The 18th International IGTE Symposium

on Numerical Field Calculation in Electrical Engineering

IGTE '18

Proceedings

Sept. 16 - 19, 2018

Hotel Novapark, Graz, Austria

Institute for Fundamentals and Theory
in Electrical Engineering - IGTE

IGTE

TU Graz
Graz University of Technology

ISBN: 978-3-85125-740-3

www.tugraz-verlag.at

TU Graz – Institut für Grundlagen und Theorie der Elektrotechnik (IGTE)
Editor: Christian Magele
Layout: Alice Reinbacher-Köstinger
Cover: Alice Reinbacher-Köstinger

www.tugraz-verlag.at

ISBN (e-book): 978-3-85125-740-3
DOI: 10.3217/978-3-85125-740-3

List of Proceedings

1 **Design concepts of low-frequency electromagnetic devices based on a data-driven approach (published in COMPEL)**
Ghorbanian, Vahid; Mohammadi, Mohammad Hossain; Lowther, David

3 **Usage of FEM for synthesis of Dead-Beat current controller for Permanent Magnet Synchronous Motor (published in COMPEL)**
Palka, Ryszard; Piotuch, Rafal

5 **Mutual Inductance-Based Angular Position Sensor for Autonomous Log Grasping**
Gietler, Harald; Stetco, Christian; Zangl, Hubert

11 **A Level Set Modeling for Moving Magnet in Finite Element Analysis**
Hayatsu, Masato; Okamoto, Yoshifumi; Nakamura, Yuta; Nakamura, Sousuke

17 **Analysis of Penalty Parameters for Interior Penalty Galerkin Methods (published in COMPEL)**
Straßer, Sebastian; Herzog, Hans-Georg

19 **Comparison of the Efficiency of E-Core Transformer to Hybrid System with Magnetic Flux Modulation**
Yatchev, Ivan; Balabozov, Iosko

23 **Exploiting the T(x) function in fast hysteresis models for transient circuit simulations (published in COMPEL)**
Wilhelm, Johann; Renhart, Werner

25 **Dynamic hysteresis modeling for soft magnetic composites based on isotropic vector play model and Cauer ladder network (published in COMPEL)**
Watanabe, Naoya; Takahashi, Yasuhito; Fujiwara, Koji

27 **Modelling the penetration of magnetic flux in thin superconducting films with shell transformations (published in COMPEL)**
Burger, Loïc; Geuzaine, Christophe; Henrotte, François; Vanderheyden, Benoît

29 **The Impact of Human Age on the Amount of Absorbed Energy from Mobile Phone (published in COMPEL)**
Jovanovic, Dejan; Stankovic, Vladimir; Cvetkovic, Nenad N.; Krstic, Dejan; Vuckovic, Dragan

31 **Peculiarities of Calculating Forced Electromagnets Shunt Windings Heating in Transient Modes**
Bajda, Yevgen; Klymenko, Borys; Pantelyat, Michael G.; Korol, Olena; Yelanskyi, Yurii

37 **Low-power electrical impedance tomography spectroscopy (published in COMPEL)**
Padilha Leitzke, Juliana; Zangl, Hubert

39 **A new approach to couple FEM calculated inductivity matrix with a non-linear magnetic circuit**
Koczka, Gergely; Preis, Kurt; Labinsky, Robert

43 **Anderson acceleration for electromagnetic nonlinear problems (published in COMPEL)**
Filippini, Mattia; Alotto, Piergiorgio; Giust, Alessandro

45 **Parallel finite-element method using domain decomposition and Parareal for transient motor starting analysis (published in COMPEL)**
Takahashi, Yasuhito; Fujiwara, Koji; Iwashita, Takeshi; Nakashima, Hiroshi

47 **Statistical Solution of Inverse Problems using a State Reduction (published in COMPEL)**
Neumayer, Markus; Suppan, Thomas; Bretterklieber, Thomas

49 **Algebraic Properties of Poynting-Theorem**
Töpfer, Hannes; Ulm, Jürgen; Delkov, Dimitri

53 **Modeling of the Reversible Heat Sources in Lithium Ion Batteries and its Impact on a Multi-Physics Model**
Koester, Niels; Essl, Christiane; Pichler, Franz; Thaler, Alexander; Fabian, Jürgen; Parz, Peter; Prosznigg, Florian

59 **Accelerating Parameter Estimation in Doyle-Fuller-Newman Model for Lithium-Ion Batteries (published in COMPEL)**
Reddy, Sohail R.; Scharrer, Matthias K.; Pichler, Franz; Watzenig, Daniel; Dulikravich, George S.

61 **Model Order Reducibility of Nonlinear Electro-Quasistatic Problems (published in COMPEL)**
Kasolis, Fotios; Clemens, Markus

63 **Multiphysics field computations for high-end smart sensor design**
Buchau, André; Anders, Jens

69 **A novel variant of the H - Φ field formulation for magnetostatic and eddy current problems (published in COMPEL)**
Smajic, Jasmin

71 **Simulating induction heating processes using harmonic balance FEM (published in COMPEL)**
Roppert, Klaus; Toth, Florian; Kaltenbacher, Manfred

73 **Magnetic coupling of mechanical modes in MRI systems (published in COMPEL)**
Ströhlein, Christopher Andreas; Landes, Hermann; Krug, Andreas; Dietz, Peter

75 **A Non-smooth Newton Method for the Solution of Magnetostatic Field Problems with Hysteresis (published in COMPEL)**
Willerich, Stephan; Herzog, Hans-Georg

77 **Behavioral Modeling of PM Motors Based on Current- and Position-Dependent Inductance Matrix Utilizing Frozen Permeability Method**
Shutta, Yusaku; Takahashi, Yasuhito; Fujiwara, Koji

83 **Comparison of Different Soil Models for the Dimensioning of the Grounding Systems**
Jesenik, Marko; Beković, Miloš; Hamler, Anton; Trlep, Mladen

89 **Design Optimization of Conductor Plate in Magnetic Sensor for Enhancing Performance on Detection of Rail Wheel**
Kuwahara, Hiroyuki; Ando, Atsushi; Maruyama, Yuya; Wakao, Shinji; Takahashi, Masahide; Yagi, Makoto; Okutani, Tamio; Okamoto, Yoshifumi

95 **Temperature-dependent hysteresis model for soft magnetic materials (published in COMPEL)**
Longhitano, Maria Roberta; Sixdenier, Fabien; Scorretti, Riccardo; Krähenbühl, Laurent; Geuzaine, Christophe

97 **Finite-element Analysis of Turbine Generator Using Homogenization Method Taking Account of Magnetic Anisotropy (published in COMPEL)**
Minehisa, Ryoko; Takahashi, Yasuhito; Fujiwara, Koji; Takahashi, Norio; Fujita, Masafumi; Tsujikawa, Kazuma; Nagakura, Ken

99 **Enhancement of convergence characteristic of Newton-Raphson method with line search for nonlinear eddy current analysis based on time-periodic FEM (published in COMPEL)**
Kakita, Shimpei; Okamoto, Yoshifumi

101 **Optimization Procedure for Approximation of Square-shaped Wire Electrode by an Ring Electrode**
Cvetkovic, Nenad N.; Barukcic, Marinko; Jovanovic, Dejan; Stojanovic, Miodrag; Hederic, Zeljko

107 **Performance of Krylov subspace method with SOR preconditioner supported by Eisenstat's technique for linear system derived from time-periodic FEM (published in COMPEL)**
Kumagai, Makoto; Kakita, Shimpei; Okamoto, Yoshifumi

109 **Worst-Case analysis of electronic circuits based on an analytic forward solver approach (published in COMPEL)**
Schenk, Mario; Muetze, Anette; Krischan, Klaus; Magele, Christian

111 **A MSFEM to simulate the eddy current problem in laminated iron cores in 3D (published in COMPEL)**
Hollaus, Karl

113 **Simulating Metallic Contamination in Permanent Magnets used in Magnetic Sensors (published in COMPEL)**
Santos Da Silva, Safire Torres; Jerance, Nikola; Rakotoarison, Harijaona Lalao

115 **Comparison of different vector Preisach models for the simulation of ferromagnetic materials (published in COMPEL)**
Nierla, Michael; Löffler, Michael; Kaltenbacher, Manfred; Rupitsch, Stefan J.

117 **Experimental technique for high frequency conductivity measurement (published in COMPEL)**
Marák, Károly; Bilicz, Sándor; Pávó, József

Index of Authors **119**

The 18th International IGTE Symposium on Numerical Field Calculation in Electrical Engineering was sponsored and supported by:

Design concepts of low-frequency electromagnetic devices based on a data-driven approach

Vahid Ghorbanian, Mohammad Hossain Mohammadi, David Lowther

Department of Electrical and Computer Engineering, McGill University, Montreal, Canada

Purpose:
This paper aims to propose a data-driven approach to determine the design guidelines for lowfrequency electromagnetic devices.

Design/methodology/approach:
Two different devices, a core-type single-phase transformer and a motor-drive system, are used to show the usefulness and generalizability of the proposed approach. Using a finite element solver, a large database of design possibilities is created by varying design parameters, i.e. the geometrical and control parameters of the systems. Design rules are then extracted by performing a statistical analysis and exploring optimal and sub-optimal designs considering various targets such as efficiency, torque ripple and power factor.

Findings:
It is demonstrated that the correlation of the design parameters influences the way the datadriven approach must be made. Also, guidelines for defining new design constraints, which can lead to a more efficient optimization routine, are introduced for both case studies.

Originality/value:
Using the proposed approach, new design guidelines, which are generally not obtainable by the classical design methods, are introduced. Also, the proposed approach can potentially deal with different parameterobjective correlations, as well as different number of connected systems. This approach is applicable regardless of the device type.

Keywords:
Electrical machine, Transformers, Finite element method, Design optimization methodology, Data-driven analysis, Design rules, Electric motor drives, Statistical analysis

Published in COMPEL - The international journal for computation and mathematics in electrical and electronic engineering, Vol. 38 No. 5, 2019, ISSN 0332-1649, page 1374 - 1385

Usage of FEM for synthesis of dead-beat current controller for permanent magnet synchronous motor

Ryszard Palka, Rafal Piotuch

Department of Power Systems and Electrical Drives, West Pomeranian University of Technology, Szczecin, Poland

Purpose:
Predictive controllers and permanent magnet synchronous motors (PMSMs) got more attention over the past decades thanks to their applicable features. This paper aims to propose and verify a method to design a predictive current controller with consideration of motor characteristics obtained from finite element analysis (FEA).

Design/methodology/approach:
Permanent magnet motor parameters and its maps can be calculated by means of FEA. The model takes into account magnetic saturation and thermal electro-magnetic properties. For each dq current vector and each position, self and mutual inductances are calculated. Based on co-energy method and fundamentals of coordinate transformation dynamic and static, dq inductances are obtained. These are used in classical and modified dead-beat current controller equations.

Findings:
To sustain good features of a controller over higher current regions, it is necessary to adapt control law of a dead-beat controller. After its modification, control quality can be superior over classical solution in high saturation regions. The transient simulations of controller and motor give accurate results.

Originality/value:
Common predictive current controllers use nominal motor parameters in their equations. The authors proposed a modified dead-beat current controller to improve the control quality. Here is no need to apply self-tuning algorithms, and implementation of the controller is not much more complicated than that of the classical controller. Designer of a control system can obtain required data from motor designer; in design process of modern machines such data are often already available. The proposed methodology increases control quality of the presented dead-beat controller.

Keywords:
Electrical machine, Optimal control

Published in COMPEL - The international journal for computation and mathematics in electrical and electronic engineering, Vol. 38 No. 5, 2019, ISSN 0332-1649, page 1386 - 1400

Mutual Inductance-Based Angular Position Sensor for Autonomous Log Grasping

Harald Gietler, Christian Stetco and Hubert Zangl

Institute of Smart Systems Technologies, Alpen-Adria Universität Klagenfurt, Universitätsstraße 65-67
A-9020 Klagenfurt am Wörthersee
E-mail: harald.gietler@aau.at

***Abstract*—In this paper we present a magnetic field based angular position sensor, designed to facilitate autonomous log grasping which can easily be mounted on different types of forest cranes in a retrofit fashion. The sensor is able to capture the absolute angle by estimating the mutual inductance between a single transmitter and two receiver coils. An optimal design procedure, based on Finite Element Method (FEM) simulations, is employed which yields a angular position resolution of 1°. However, extensive mechanical stress during log grasping can alter the sensor geometry and degrade its performance. Therefore, an robust design scheme is used to minimize those influences. In the presence of worst case conditions an angular position accuracy of 2.7° was achieved which is well inside of the requirements for autonomous log grasping.**

***Index Terms*—angle measurement, computational electromagnetics, magnetic sensors, robust design**

I. Introduction

The ever increasing number of autonomous systems employed in various industrial fields pushes the demand of robust and reliable sensors. Autonomous systems need precise information about their internal states to fulfill tasks such as picking and placing objects. Therefore, accurate and robust sensors are essential which endure harsh conditions over a long period of time. The underlying system in this work is a forestry crane which executes a pick and place task of logs. To pick a log correctly, the system needs also accurate information about the angular position of the grasper. In detail, a contact-free, non-incremental methodology with 360° coverage is desired. Unfortunately, the woodland is a rather harsh environment including e.g. water, moisture and mud. Additionally, mechanical stress needs to be considered.

Angular position sensors based on capacitive principles are readily available [1]. The underlying principle of those sensors is usually a change of geometry or permittivity. It is advantageous, that the design and implementation of capacitive sensors is comparably easy. Unfortunately, such sensors suffer from harsh environmental conditions due to their underlying physical principles, e.g. moisture affects the permittivity. Another common form of contact-free angular position sensors are based on optical principles. Here, a light beam is shone through or onto a grating and the resulting light is measured by a photo detector. The grating provides a position encoding. Optical systems can achieve very high resolution and accuracy, but require direct line of sight [2]. Therefore, they are not applicable in the considered application, due to the presence of detrimental environmental conditions.

The magnetic principle, on the other hand, is an alternative which can be very robust. Commonly, sensors such as anisotropic magnetoresistive sensors (AMR, e.g. [3]), giant magnetoresistive sensors (GMR, e.g. [4]), tunneling magnetoresistive sensors (TMR, e.g. [5]) and Hall effect sensors (e.g. [6]) are used. This paper presents an inductive sensor comprised of a single transmitting coil and two receiving coils. The mutual inductances between the transmitting coil and each receiving coil is estimated, which is the basis for the reconstruction of the rotation angle. The rotational encoding is achieved by a conductive plate covering portions of the coil architecture. On one hand, the drawback of this approach is the non-trivial design and implementation procedure, but on the other hand it is very robust against environmental effects such as water, moisture or dirt. The robustness of the magnetic field against above mentioned disturbances makes this approach especially suitable for the considered log grasping task.

II. Sensor Design

A simple measurement model for the relation between the magnetic field measured with multiple magnetic field sensors and the relative rotation θ of a magnet is given by Eq.(1)

$$\mathbf{S}(\theta, \boldsymbol{\eta}) = \mathbf{A}(\boldsymbol{\eta}) \sin(\theta - \boldsymbol{\varphi}(\boldsymbol{\eta})) + \mathbf{w} \tag{1}$$

where $\mathbf{S}(\theta, \boldsymbol{\eta})$ is the magnetic field sensor output signal vector, θ the angular position, $\boldsymbol{\varphi}(\boldsymbol{\eta})$ the phase shift and $\mathbf{A}(\boldsymbol{\eta})$ the amplitude vector. The measurement noise is modeled as multivariate additive white Gaussian noise $\mathbf{w} \sim \mathcal{N}(\mathbf{0}, \boldsymbol{\Sigma})$. Since both the amplitude and the phase shift vectors are considered as unknown parameters, at least two magnetic field sensors are required. A natural lower bound of any unbiased estimator for the unknown parameters is obtained by the inverse Fisher Information [7]

$$\sigma(\hat{\theta}) \geq I(\theta, \boldsymbol{\eta})^{-1} \tag{2}$$

where $\sigma(.)$ is the variance operator. A common goal of an optimal design procedure is to find a configuration $\boldsymbol{\eta}_{opt}$ that minimizes the lower bound, which is equivalent to a maximization of of the Fisher Information $I(\theta, \boldsymbol{\eta})$ of a

sensor configuration.

$$\boldsymbol{\eta}_{opt} = \arg\max_{\boldsymbol{\eta}\in H} I(\theta, \boldsymbol{\eta}) \tag{3}$$

where H is the design space of the problem.

Rewriting Eq.(1) into a I/Q model yields Eq.(4)

$$\mathbf{S}(\theta, \boldsymbol{\eta}) = I_A(\theta)\cos(\boldsymbol{\varphi}(\boldsymbol{\eta})) + Q_A(\theta)\sin(\boldsymbol{\varphi}(\boldsymbol{\eta})) + \mathbf{w} \tag{4}$$

The goal is now to find the optimal sensor configuration assuming uncorrelated measurements. The Fisher Information is obtained as

$$\mathbf{I}(\theta) = \frac{1}{\sigma^2}\mathbf{H}^T\mathbf{H}, \tag{5}$$

where $\mathbf{H}$ is given as the spatial derivative of $\mathbf{S}(\theta, \boldsymbol{\eta})$.

$$\mathbf{H} = \begin{bmatrix} \sin\varphi_1 & \cos\varphi_1 \\ \sin\varphi_2 & \cos\varphi_2 \end{bmatrix}$$

By computing the determinant of the Fisher Information in Eq.(5) for the two-sensor configuration we obtain the D-optimal design as

$$\max\det(\mathbf{H}^T\mathbf{H}) = 1 - \cos(2\varphi_1 - 2\varphi_2) \tag{6}$$

which yields an optimal angular displacement of $\varphi_{opt} = \pi/2$ of the two sensor elements [8]. The estimate of the absolute angle can be obtained using the in-phase and quadrature contributions by computing the arctangent

$$\hat{\theta} = \text{atan2}(Q_A, I_A) \tag{7}$$

It is important to note that the correct computation of the angle in Eq.(7) is only given if both contributions exhibit same amplitudes. In a practical situation this is not always true so that individual gain factors need to be introduced for an appropriate gain correction.

A. Log Grasper

The sensor is restricted in its design by the underlying geometry of the grasper (see Fig. 1), so that off-the-shelf inductors can not be used. To allow full rotation of 360 °, the front-end of the grasper is composed of a rotating and a fixed segment. Fig.1 depicts a 3D model

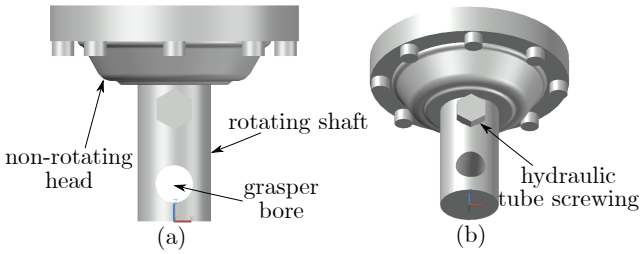

Fig. 1. Model of the rotator unit shown in profile view (a) and as a 3D model (b).

and a profile view of the rotator unit. The limitations of the design are given by tube screwings which limits the mounting of the sensor. Furthermore, the grasper is controlled by hydraulics and needs a tube connection to the non-rotating part. Also, the grasper must be mounted on the grasper bore which further limits the space on the shaft. Due to these geometrical limitations a coil design is necessary for correct angle determination.

B. Inductive Sensor

Since the optimal design is achieved by using two 90 degree phase shifted sensor elements, we model two orthogonal receiver coils ($Rx1, Rx2$) to achieve the desired phase shift in the output signal. However, the sensor design is not trivial. The mutual inductance between two coils can not directly be measured in an easy fashion. Therefore, the electromagnetic force (EMF), which can be interpreted as voltage $v(t)$, is measured and used as a basis for the estimation of the mutual inductance. The EMF $v(t,\theta)_{Rx}$ induced by a transmitter coil (Tx) in one of the two receiver coils (Rx) is given by [9]

$$v(t,\theta)_{Rx} = M(\theta)_{Rx,Tx}\frac{di_{Tx}(t)}{dt}, \tag{8}$$

where $M(\theta)_{Rx,Tx}$ is a geometry and angular position depended quantity and $i_{Tx}(t)$ is the current flowing through the active coil. The EMF can also be expressed using the magnetic flux density $\mathbf{B}_{Rx}(x,y,z,t)$ which gives

$$v(t,\theta)_{Rx} = -N_{Rx}\frac{d}{dt}\int_{\Gamma}\mathbf{B}_{Rx}(x,y,z,t)d\mathbf{A} \tag{9}$$

where N_{Rx} is the number of coil wire turns of the receiver coil, $d\mathbf{A}$ is the infinitesimal area element and Γ the cross sectional area of the passive coil represented in 3-dimensional space with $\mathbf{B}_{Rx}(x,y,z,t)$ being the corresponding magnetic flux density. For the log grasper environment the coils are restricted to be flat coils printed on a printed circuit board (PCB) on the non-rotating head of the grasper front-end. Additionally, it is thought to be mounted in a retrofit fashion. Therefore, 360° geometries are avoided. As a consequence, the active coil covers 270°, whereas the passive coils cover 180° each and are located in the cross sectional area of the active coil, see Fig. 2. The receiving coils are symmetrically placed around the center of the transmitting coil. The transmitter coil is driven with a sinusoidal excitation signal, to generate a time-varying magnetic field. To extract angular information at the receiver side, a conductive plate mounted on the rotating shaft of the grasper-front end is used. The conductive plate shields the magnetic field lines due to eddy currents in the plate which produce a counter-acting magnetic field. Thus, the net magnetic field reduces and the flux through the receiver coils decreases. This cyclic shielding gives an amplitude modulated signal at the receiver in the angular domain. The receiver coils cross sectional area is given by

$$A_{rx} = A_C - A_r, \tag{10}$$

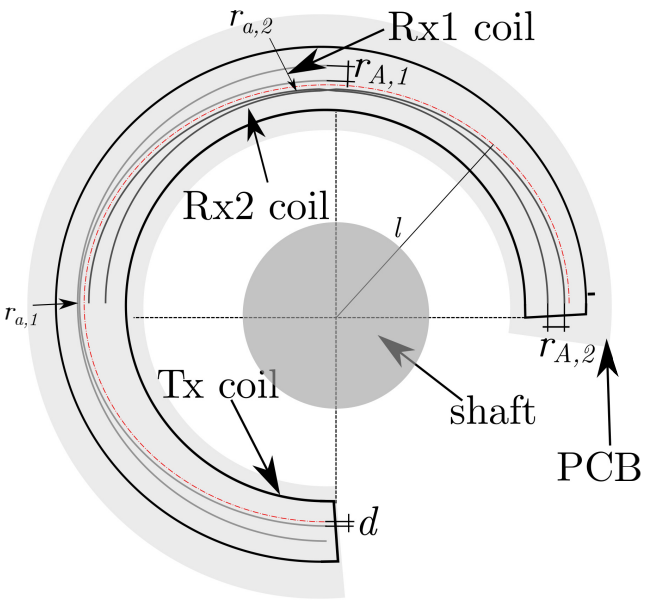

Fig. 2. Schematic view on the proposed coil design for the magnetic angular position sensor comprised by a single transmitter and two receivers.

where A_C corresponds to the area under the modulated line $\mathbf{C}(\theta)$ given by the parametrization

$$\mathbf{C}(\theta) = \begin{bmatrix} (l + r_a + d + r_A \sin(2(\theta + \frac{\pi}{4}))) \cdot \cos(\theta) \\ (l + r_a + d + r_A \sin(2(\theta + \frac{\pi}{4}))) \cdot \sin(\theta) \end{bmatrix}. \tag{11}$$

The quantities l, r_a, d and r_A correspond the distances shown in Fig. 2. The area under $\mathbf{C}(\theta)$ is given by

$$A_C = \frac{1}{2} \int_0^{\Theta} (C_x \dot{C}_y - \dot{C}_x C_y) d\theta. \tag{12}$$

A_r is the area of a circular sector with radius $l + d$ and angle $\alpha = 180°$. Choosing the parameters of the two receiver coils equally, would lead to an inequality in their cross sectional areas. In fact, the area of the inner receiver coil would be smaller. The area modulation is a result of the parameters r_a and r_A, which represent the minimum amplitude and the maximum amplitude of the sinusoidally shaped coil-wire, respectively. Choosing those parameters differently for the second receiver coil leads to equal cross sectional areas. Therefore, the parameters of the outer coil, further denoted as $Rx1$, are firstly chosen. Subsequently, the parameters of the inner coil, further denoted as $Rx2$, are determined satisfying the quadratic cost function

$$\begin{aligned} &\underset{r_{a_2}, r_{A_2}}{\text{minimize}} \quad \sum_{\theta=0}^{2\pi} (A_{Rx2} - A_{Rx1})^2 \\ &\text{subject to} \quad r_{a_2}, r_{A_2} \in \mathbf{S} \end{aligned} \tag{13}$$

For the optimization the 90° phase shift between $Rx2$ and $Rx1$ is resolved. It's worth noting that the magnetic flux density in the receiver coils is not uniformly distributed. In fact, it increases with decreasing distance to the transmitter coil-wire. To equalize the areas of the receiver coil, the modulation amplitude r_{A_2} of $Rx2$ exceeds the amplitude r_{A_1} of $Rx1$. Subsequently, a portion of A_{Rx2} is closer to the transmitter coil-wire. The flux density in this part is higher compared to the area part which is symmetrical with A_{Rx1}. Additionally, also the transmitter coil is not symmetric due to its circular shape. The arc length of the inner part of the winding is shorter than the outer part of the winding. This reduces the magnetic flux through $Rx2$. Those influences are analyzed using commercial finite element method (FEM) software and r_{A_2} is optimized in a way that

$$\begin{aligned} &\underset{r_{A_2}}{\text{minimize}} \quad \sum_{\theta=0}^{2\pi} (\Phi_{Rx2} - \Phi_{Rx1})^2 \\ &\text{subject to} \quad r_{A_2} \in \mathbf{S} \end{aligned} \tag{14}$$

is fulfilled, where Φ_{Rx2} and Φ_{Rx1} represent the magnetic flux through the cross sectional areas of $Rx2$ and $Rx1$, respectively. Furthermore, the receiver coils are twisted in order to eliminate offsets. Therefore, the magnetic flux through an uncovered receiver coil sums up to zero. A 3D model of the sensor design on the grasper front-end is shown in Fig. 3.

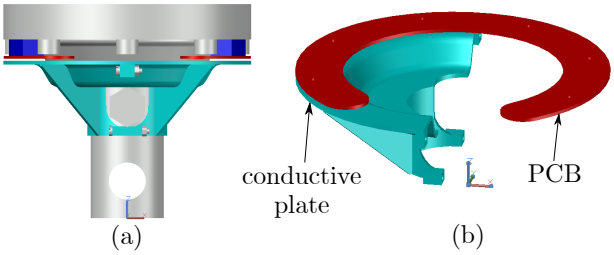

Fig. 3. 3D model of the mounted sensor on the grasper-front end (a) and proposed sensor design (b).

C. Robust Design

Due to environmental impacts the conductive plate is subject to mechanical strain which leads to deformation and tilt. Since the air gap between the conductive plate and the printed circuit board is very small a design strategy in terms of tilt robustness must be developed to ensure correct operation under harsh conditions. The conductive plate can be upward tilted in positive z-direction and also downward tilted in negative z-direction. The situation for both tilt possibilities is exemplary shown in Fig. 4. The distance between the PCB and the conductive plate is denoted by h. Due to the tilt of the conductive plate there will be a change of the distances between the receiver coils and the plate. From Fig. 4 it is obvious that the outer coil $Rx1$ is more affected by the tilt than the $Rx2$ coil since the change in distance Δh_{Rx1} varies more than the change Δh_{Rx2}. Thus we assume that the induced voltage in $Rx1$ coil is more affected at both tilt conditions. Fig. 5 shows a typical distribution of the magnetic flux density under normal conditions and at upward tilt. Since the tilt reduces the distance h between plate and coils, more eddy currents are induced in the

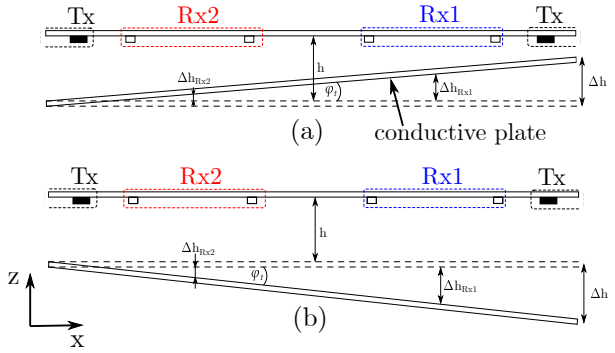

Fig. 4. Schematic side view of upward tilt (a) and downward tilt (b)

conductive material which leads to a decreasing magnetic field within the receiver coils. For downward tilt (Fig. 6)

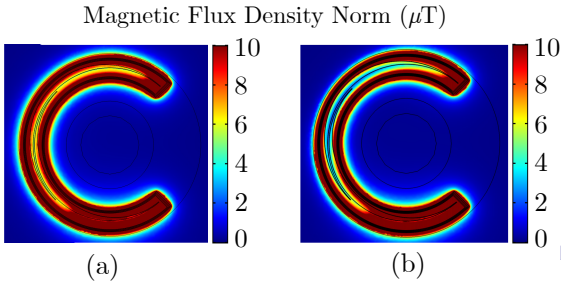

Fig. 5. Absolute value of the magnetic flux density $\mathbf{B}(x, y, z, t)$ at normal conditions (a) and upward tilt (b) using a tilt degree of $\varphi_t = 3°$.

the magnetic flux density increases since the counteracting magnetic field is lower. This is caused by the magnetic flux density which decreases with increasing distance. Consequently, for large downward tilt angles

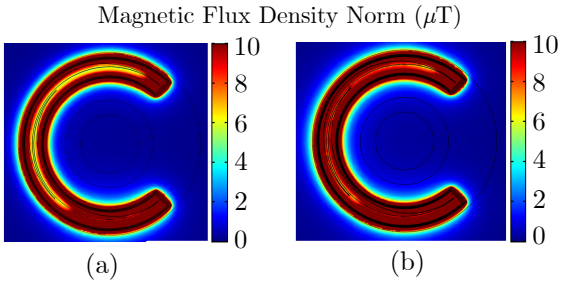

Fig. 6. Absolute value of the magnetic flux density $\mathbf{B}(x, y, z, t)$ at normal conditions (a) and downward tilt (b) using a tilt degree of $\varphi_t = -3°$.

the angular information is lost since the magnetic field in the receiver coils retains close to its maximum. Both tilt scenarios were examined using FEM simulations and a typical simulation result of the magnetic flux through both receiver coils is shown in Fig. 7 using a tilt degree of $\varphi_t = \pm 3°$.

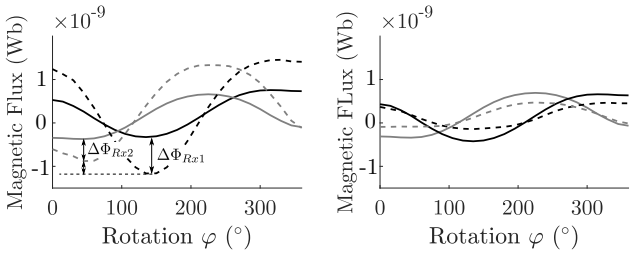

Fig. 7. The influence of the tilt on the magnetic flux through the coils is reported. It is observed that both, upward shown in the left plot and downward tilt shown in the right plot, alter the flux through both receiver coils differently. Furthermore, the flux change due to upward tilt $\varphi_t = 3°$ dominates, compared to downward tilt $\varphi_t = -3°$.

The tilt leads to a mismatch in the signal amplitudes. This is critical since the reconstruction of the angle using Eq.(7) requires equal or at least known amplitudes. Unfortunately, the tilt occurs randomly without a known underlying probability function. Hence, the goal of the robust design procedure is to change the coil geometries such that the angular position estimation is robust against stress caused tilts. Nevertheless, this geometry-adaption may degrade the performance of the nominal design but improves the estimation accuracy in presence of worst-case scenarios. Mathematically, the robust design is formulated as an optimization problem, which is minimizing the magnetic flux difference between the $Rx1$ and $Rx2$ coil. The optimization problem is given by [10]

$$\min_{r_{A_2}} \max_{\mathbf{T}} |\Phi_{Rx1} - \Phi_{Rx2}|, \tag{15}$$

where the space $\mathbf{T}$ contains all angular positions and all tilt possibilities. Firstly, the minimax optimization approach searches over the space $\mathbf{T}$ for the worst case, which is the highest absolute magnetic flux difference between $Rx1$ and $Rx2$. Subsequently, the geometry is adapted so that the magnetic flux difference is minimized.

III. Results

Simulations of the given scenario were carried out using commercial FEM software. Copper was selected as material for the conductive plate due to its high conductivity and low permeability. The rotating shaft and the static part of the rotator were modelled using iron. Experiments were conducted using a current strength of $0.01\,\mathrm{A}$ and an excitation frequency of $f = 3.5\mathrm{MHz}$ which eliminates the influence of the surrounding iron due to the low skin depth [11] of iron at high frequencies. For completeness, the used permeability of iron is $\mu_{fe} = 4000$ and its conductivity is $\sigma_{fe} = 11.2\,\frac{\mathrm{MS}}{\mathrm{m}}$. The PCB coils were modeled as quadratic copper coils with a thickness of $0.2\,\mathrm{mm}$. The plate was rotated clockwise in $1°$ increments at a distance of $h = 5\,\mathrm{mm}$ with respect to the PCB. Simulations were carried out for tilt scenarios as well as ideal conditions. The tilt scenario was further investigated using different tilt degrees in the range $\varphi_t = [-3° \ldots\ 3°]$ to investigate the tilt effect on the output

signals and the angle reconstruction. Fig. 8 summarizes the mean error between the reconstructed angle and a reference signal model. In the presence of ideal conditions the mean error is around $\Delta\theta = 1.047°$ which is shown in Fig. 8. A more accurate result could be achieved if the grid resolution of the numerical integration is increased with the drawback of a larger computational cost. Using the nominal design for the worst case tilt scenario, the mean error drastically increases up to $5.603°$. Using the robust design paradigm a performance of $2.7619°$ can be achieved which validates the robustness.

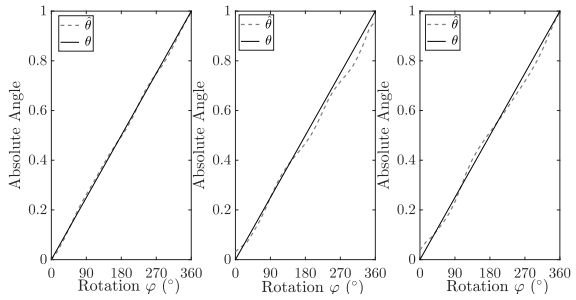

Fig. 8. Reconstructed angle using optimal design without tilt (a), using optimal design with tilt (b) and using robust design with tilt (c).

From Fig. 8 it is observed that at tilt conditions the angle estimate oscillates around the true angle of the signal model. This is due to the gain difference which can not fully be compensated using the proposed robust design scheme. The sensor accuracy, which is in the low-degree range, well satisfies the requirements for the log grasping application. Apart of the robustness against tilt, the underlying physical principles of the sensor make it additionally robust against detrimental influences such as moisture, water, mud or fog.

IV. Conclusion

We present an mutual inductance-based angular position sensor incorporating optimal and robust design paradigms. The sensor is able to reconstruct the absolute angle of a full $360°$ rotation using a geometrical design of $270°$ achieving a mean error of $1.0470°$. Simulation results showed the importance of a robust design towards worst-case scenarios which were identified by the tilt of the conductive plate due to mechanical stress. The derivation of a design paradigm yield a robust optimization problem which was applied to the sensor configuration. The adapted sensor structure yields an accuracy of $2.7619°$ in the presence of the worst case scenario, which is well inside the requirement of the proposed autonomous log grasping task. Additionally, the generic sensor design approach can easily be adapted to different forestry cranes geometries and mounted in a retrofit fashion.

Acknowledgement

The research leading to these results has received funding from the Austrian Research Promotion Agency (FFG) under the grant agreement 864807 (Auto-LOG).

References

[1] P. L. Fulmek, F. Wandling, W. Zdiarsky, G. Brasseur, and S. P. Cermak, "Capacitive sensor for relative angle measurement," *IEEE Transactions on Instrumentation and Measurement*, vol. 51, pp. 1145–1149, Dec 2002.

[2] F. Cherchi, L. Disingrini, S. Gregori, G. Torelli, V. Liberali, and M. Gottardi, "A digital self-calibration circuit for optical rotary encoder microsystems," in *IMTC 2001. Proceedings of the 18th IEEE Instrumentation and Measurement Technology Conference. Rediscovering Measurement in the Age of Informatics (Cat. No.01CH 37188)*, vol. 3, pp. 1619–1624 vol.3, May 2001.

[3] A. Arami, J. D. Rechenmann, and K. Aminian, "Reference-free automated magnetic sensor calibration for angle estimation in smart knee prostheses," *IEEE Sensors Journal*, vol. 14, pp. 1788–1796, June 2014.

[4] U. Ausserlechner, "The optimum layout for giant magnetoresistive angle sensors," *IEEE Sensors Journal*, vol. 10, pp. 1571–1582, Oct 2010.

[5] H. Yamazaki, H. Hirabayashi, N. Oyama, and M. Sakai, "Characteristics of tmr angle sensors," in *Proceedings SENSOR 2011*, pp. 361–365, 2011.

[6] S. Wu, J. Chen, and S. Wu, "A rotary encoder with an eccentrically mounted ring magnet," *IEEE Transactions on Instrumentation and Measurement*, vol. 63, pp. 1907–1915, Aug 2014.

[7] S. M. Kay, *Fundamentals of Statistical Signal Processing: Estimation Theory*. Prentice Hall, 1997.

[8] H. Zangl, L.-M. Faller, and W. Granig, "Optimal design of angular position sensors," *COMPEL - The international journal for computation and mathematics in electrical and electronic engineering*, vol. 36, no. 5, pp. 1372–1385, 2017.

[9] J. D. Jackson, *Classical electrodynamics*. New York, NY: Wiley, 3rd ed. ed., 1999.

[10] G. Heo, B. Schmuland, and D. P. Wiens, "Restricted minimax robust designs for misspecified regression models," *Canadian Journal of Statistics*, vol. 29, no. 1, pp. 117–128.

[11] H. Johnson and M. Graham, "High-speed signal propagation: Advanced black magic," 01 2003.

A Level Set Modeling for Moving Magnet in Finite Element Analysis

Masato Hayatsu, Yoshifumi Okamoto, Yuta Nakamura, and Sousuke Nakamura
*Department of Electrical and Electronic Engineering, Hosei University, Tokyo 184-8584, Japan
E-mail: masato.hayatsu.4v@stu.hosei.ac.jp, okamotoy@hosei.ac.jp

***Abstract*—When the electromagnetic field analysis of an electric device with a moving object, such as a motor or an actuator, is performed using the finite element method (FEM), a special modification to connect two finite element meshes on the interface between the moving and stationary region is frequently required. The typical methods for connecting finite element meshes at the interface are conforming connection and nonconforming connection. To make a conforming connection, it is necessary to completely set the number of nodes on both sides to the same number each other. Complex programming to connect different-unstructured-meshes with nonconformity is necessary for manipulating the stiffness matrix. In this paper, a method to realize flexible motion of a moving object using the level set function is proposed. In the proposed method, because the values of level set function in all nodes are converted to ON-OFF data of the object, it is possible to significantly increase the degree of freedom of the object. In this paper, we demonstrate the performance of the proposed method and we investigate the computational accuracy in the examination with linearly moving magnet. Furthermore, the proposed method is applied to magnetic field analysis of a magnetic levitation system, in which the N-S arrayed magnets rotate.**

***Index Terms*— Electromagnetic force, Heaviside function, level set function, moving magnet.**

I. Introduction

In recent years, there are many electromagnetic devices that use moving objects, such as electric motors and actuators. Magnetic levitation devices [1], [2] are attracting attention among electromagnetic devices that use moving objects. Because of advantages such as reduction in friction and abrasion, reduction in vibration and noise, and reduction in energy loss, magnetic levitation devices are being developed as methods for transporting people and objects. The principle of a magnetic levitation device is based on the assumption that the conductor is laid on the bottom. When aggregation of the permanent magnets inside the device rotates at a high speed, an eddy current is generated in the conductor. Consequently, a magnetic reaction field is caused by the eddy current and a levitation force is generated by the repulsion between the magnets and the magnetic reaction field. Copper is used as the conductor and a neodymium magnet is used as the permanent magnet. Moreover, by changing the arrangement of the magnets, there is a possibility to realize a strong levitation force, and it is efficient to design a high-performance magnetic levitation device by numerical analysis beforehand.

As an analytical method for the electric devices that is this study, two methods have been proposed. The first method is the method applies the moving coordinate system [3]. In [3], a DC steady state eddy current analysis considering to the rotor rotation is described. In [3], it is reported that a stable solution can be obtained even when Peclet number is sufficiently high by using a moving coordinate system. However, as the rotational speed increases, the number of iterations in the asymmetric linear solution increases, which is a disadvantage. Secondly, the finite element method (FEM) with nonconforming mesh connection [4], [5] makes it possible to connect the mesh with different distribution by imposing continuity of the magnetic vector potential $\boldsymbol{A}$ using linear combination. While the advantage of FEM with nonconforming mesh connection is to connect the finite element mesh without deformation of the element, the search for edge relationship between master and slave side is difficult.

In this paper, to overcome the aforementioned disadvantages, a modeling method supported by the level set function (MLS) [6], [7] that does not depend on the distribution of a finite element mesh in the stationary region is proposed [8]. In the MLS, the contour of the moving object is first set using the zero-isosurface of the level set function. However, it is impossible to define material constants using the level set function because the level set function value can be infinity. Therefore, the level set function must be converted to an ON-OFF format to define the material constants. As a countermeasure, the level set function value is incorporated into the Heaviside functions [9], [10]. Provided that the node is inside the moving object, the level set function value is set to a positive value, and if the node is outside the moving object, it is set to a negative value. Moreover, in the vicinity of the contour of the moving object, the interface between the air and the magnet regions can be handled continuously by the Heaviside function approximated by a fifth order function. Therefore, because the MLS depends on the location information of the zero-isosurface, it is possible to express the moving object without updating mesh data. In this paper, the performance of the MLS is first shown in the analysis model with linearly moving magnet as a basic example. Next, the MLS is applied to a magnetic levitation device for verification.

II. Modeling Object Method

A. Finite Element Method

In this paper, edge-based FEM is used as the electromagnetic field analysis method. The edge-based weighted residual G_k and nodal residual G_i in the

$\boldsymbol{A}-\phi$ formulation are given as follows:

$$G_k = \iiint_{\Omega_{\mathrm{all}}} (\nabla \times \boldsymbol{N}_k)\cdot(\nu \nabla \times \boldsymbol{A})\, dV - \iiint_{\Omega_{\mathrm{m}}} \boldsymbol{N}_k \cdot (\nu_0 \nabla \times \boldsymbol{M}_{\mathrm{m}})\, dV + \iiint_{\Omega_{\mathrm{e}}} \boldsymbol{N}_k \cdot \sigma\left(\frac{\partial \boldsymbol{A}}{\partial t} + \nabla \phi\right) dV = 0, \quad (1)$$

$$G_i = \iiint_{\Omega_{\mathrm{e}}} (\nabla N_i)\cdot \sigma\left(\frac{\partial \boldsymbol{A}}{\partial t} + \nabla \phi\right) dV = 0, \quad (2)$$

where Ω_{all} denotes the analysis region, Ω_{m} is the permanent magnet region, Ω_{e} is the eddy current region, $\boldsymbol{A}$ is the magnetic vector potential, ϕ is the electric scalar potential, $\boldsymbol{N}_k$ is the edge-based vector shape function at edge k, N_i is the nodal scalar shape function at node i, $\boldsymbol{M}_{\mathrm{m}}$ is the magnetization vector, the material constants ν and σ are the magnetic reluctivity and conductivity, respectively, and ν_0 is the magnetic reluctivity of vacuum. The notation of the boundary integral term in the equations (1) and (2) is omitted.

B. MLS

In conventional electromagnetic field analysis using the FEM, it is necessary to correct the coordinates in accordance with the moving object as shown in Figure 1. On the other hand, in the MLS, a moving object is modeled using the zero-isosurface of the level set function and by moving the zero-isosurface. Therefore, it is possible to realize the analysis without updating the mesh data. The level set function ψ is defined as follows:

$$\psi(\boldsymbol{x}) = \begin{cases} d(\boldsymbol{x}, \partial\Omega) & \boldsymbol{x} \in \Omega \\ 0 & \boldsymbol{x} \in \partial\Omega \\ -d(\boldsymbol{x}, \partial\Omega) & \boldsymbol{x} \notin \Omega \end{cases}, \quad (3)$$

where Ω is the magnet region, $\partial\Omega$ is the zero-isosurface, which shows the interface between the magnet region and air, and $d(\boldsymbol{x},\partial\Omega)$ is the shortest distance from $\partial\Omega$. Figure 2 shows a visualization of the level set function value. As shown in Figure 2, the contour of the magnet is defined by a zero-isosurface, and the function value increases as going deeper into the magnet region.

Given that the level set function value can be infinity, the level set function can not express the material constants. Then, to apply the level set function value to FEM, the level set function is transformed into a function that returns a value from 0 to 1. Thus, the smoothed Heaviside function (SHF) [9], which continuously changes 0 (air) to 1 (magnet), enables the FEM to easily realize a moving object without special treatment. The SHF $H(\psi)$ approximated by a fifth order function can be formulated as follows:

$$H(\psi) = \begin{cases} 0 & (\psi < -h) \\ \frac{1}{2} + \frac{15}{16}\left(\frac{\psi}{h}\right) - \frac{5}{8}\left(\frac{\psi}{h}\right)^3 + \frac{3}{16}\left(\frac{\psi}{h}\right)^5 & (-h \le \psi \le h) \\ 1 & (h < \psi) \end{cases}, \quad (4)$$

where h is the transition width for continuously handling material constants.

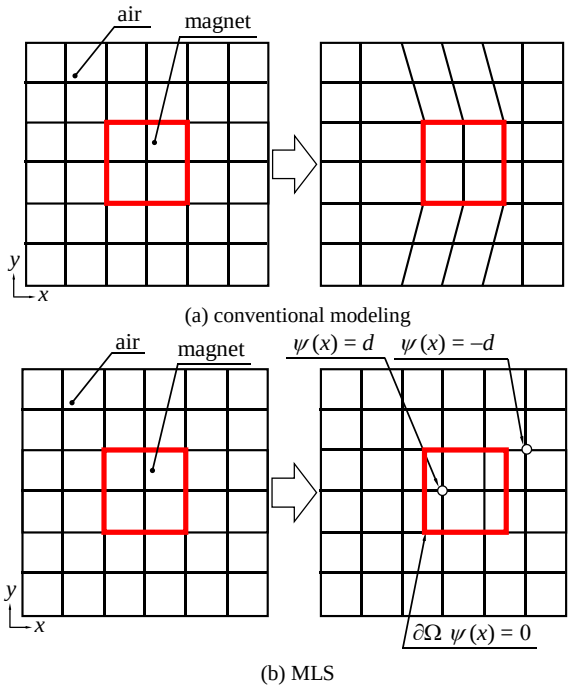

Figure 1: Modeling using the conventional method and MSL.

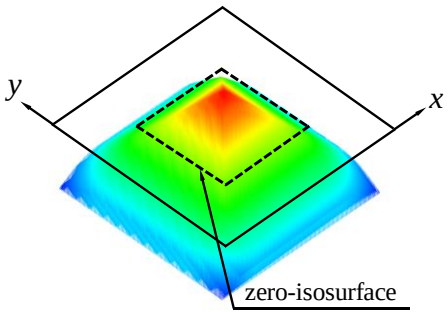

Figure 2: Distribution of the level set function.

Figure 3 shows the relationship between the level set function $\psi(x)$ and the Heaviside function $H(\psi)$ in the x-direction. In this case, the zero-isosurface of $\psi(x)$ is set to an arbitrary point ($x = \beta$, $x = -\beta$). Therefore, when the region of a moving object is confined to $-\beta \le x \le \beta$ and $\psi(x)$ is calculated, the sign of the gradient in $\psi(x)$ is reversed when $x = 0$ as the boundary. Furthermore, $\psi(x)$ satisfies the following condition on the property of the equidistant function.

$$|\nabla \psi| = 1. \quad (5)$$

Similarly, the distribution of $H(\psi)$ for evaluating material constants also changes when $x = \beta$ and $x = -\beta$. When the value of $H(\psi)$ is 0, the material is defined by air. When the value of $H(\psi)$ is 1, the material is defined by the moving object. Furthermore, within the width of the transition, the material continuity is imposed by a fifth order function.

The moving object is defined as a permanent magnet to consider not only linear motion but also the rotation of the swarm of magnets in magnetic levitation device. When a permanent magnet is modeled using a level set function, the magnetization vector $\boldsymbol{M}(\psi)$ is approximated using $H(\psi)$ as follows:

$$\boldsymbol{M}(\psi) = H(\psi)\boldsymbol{M}_0, \quad (6)$$

where $\boldsymbol{M}_0$ is magnetization vector in permanent magnet.

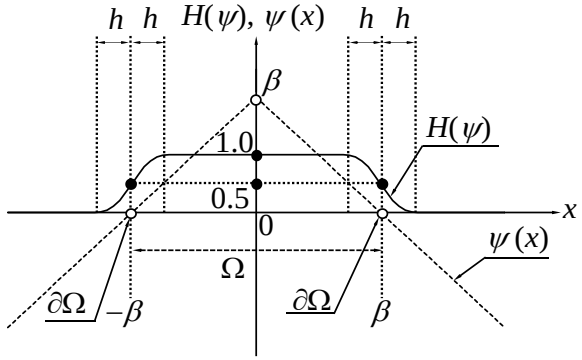

Figure 3: Relationship between the level set function and the SHF.

III. Analysis Model

A. Basic Verification Model

The performance of the MLS is verified by the simple model. Figure 4 shows the basic verification model. In this model, the permanent magnet is linearly moved along the *x*-direction in the upper part of the conductor. Therefore, an electromotive force is induced in the conductor, and an eddy current is generated. The eddy current loss and electromagnetic force are analyzed. The eddy current loss generated on the conductor is calculated as follows:

$$P_{Je} = \int_{\Omega_e} \frac{\boldsymbol{J}_e^{\,2}}{\sigma} dV, \tag{7}$$

where $\boldsymbol{J}_e$ is eddy current density. Moreover, the electromagnetic force is analyzed using the nodal force method [11]. The nodal force $\boldsymbol{f}_i$ at node i is given as:

$$\boldsymbol{f}_i = -\int_{\Gamma_f} \boldsymbol{T} \nabla N_i dV, \tag{8}$$

where $\boldsymbol{T}$ is stress tensor, Γ_f is one layer of the air region surrounding the conductor. Moreover, the total force generated on the conductor can be obtained by summation of all nodal forces. The total force $\boldsymbol{F}$ is described as:

$$\boldsymbol{F} = \sum_i \boldsymbol{f}_i. \tag{9}$$

In this verification, the copper is considered as the conductor, and the neodymium magnet is considered as the permanent magnet. The intensity of magnetization is 1.25 T in *z*-direction. This magnet is moved by 2.5 mm during each time-step. The velocity is 5.0 m/s.

The hexahedral 1st order edge-based element is adopted for discretization in FEM. The number of elements is 383,070, the number of nodes is 363,776, and degree of freedom is 1,165,712. To solve the simultaneous linear equations obtained by FEM, the ICCG method [12], [13] is applied. When relative residual of ICCG is less than 10^{-6}, the iterative process of ICCG is terminated. For the discretization in the time direction, the GEAR backward difference [14], [15] is adopted. Then, the width of the time-step Δt is set to 1.0 ms and the number of time-step is set to 24.

In the MLS, zero-isosurface is moved in the *x*-direction by 2.5 mm at each time-step at the same velocity (v = 5.0 m/s) as that of the magnet. Furthermore, MLS is compared with the conventional method by adopting two lengths (h = 0.5 and 1.5 mm) for the transition width. Moreover, MLS is evaluated under the condition that the width of the time-step Δt is changed into 0.5 ms when the transition width h is 0.5 mm.

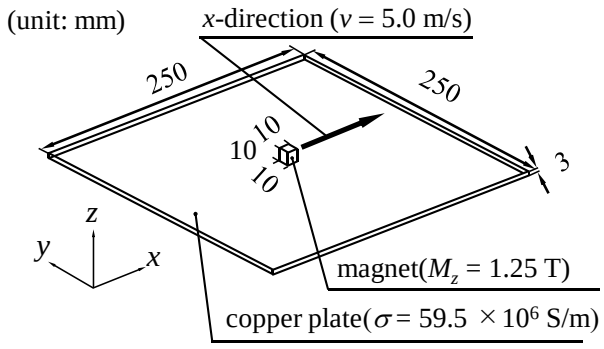

(a) bird's-eye view

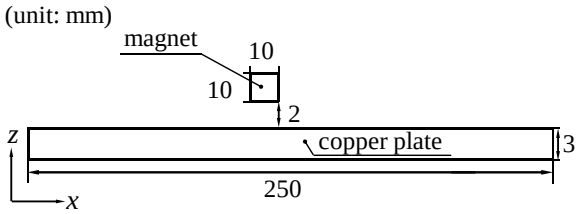

(b) *x*–*z* plane

Figure 4: Analysis model (basic verification model).

B. Magnetic Levitation Device

In this section, the specification of a magnetic levitation system that applies the N-S array is defined. Figure 5 shows the analysis model for a magnetic levitation device. A copper plate is used as the conductor (σ=59.5×10^6 S/m) and a neodymium magnet is used as the permanent magnet (the intensity of magnetization is 1.25 T in the *z*-direction), similar to the previous section. Furthermore, the magnetic levitation device is set to float 2 mm, and eight neodymium magnets are arranged on the circumference in the device. As shown in Figure 5 (a), the magnet array has N poles and S poles arranged alternately. The time-step width Δt is set to 1.0 ms and the rotating pitch is set to 7.5 degrees such that the magnet array is rotated at 1,600 rpm. Additionally, the number of total time step is set to 36.

In this model, the number of elements is 118,560, the number of nodes is 122,034, and the degree of freedom is 364,588. Figure 6 shows the mesh for magnetic levitation device used in the conventional method. The mesh is uniformly generated based on the rotation pitch. However, because the shape of the magnet is cubical in shape, it is necessary to match the shape of the magnet by performing coordinate transformations. Consequently, as shown in Figure 6, the shape of the mesh in the conventional method is distorted in the magnet region and its surroundings. Furthermore, when the rotation of the magnet is considered, it is necessary to perform the next step after restoring the shape of the mesh. Therefore, additional time and effort are necessary to repeat the modifications and restore the mesh data.

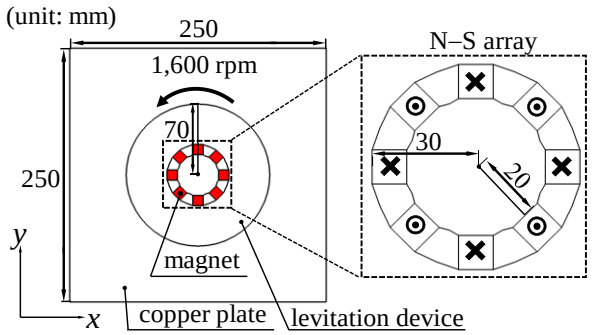

(a) x–y plane

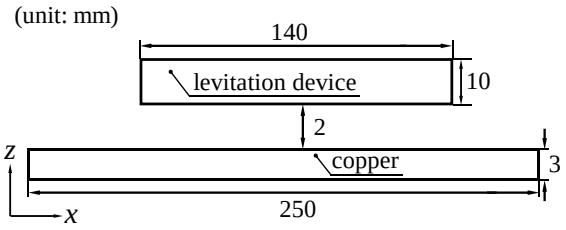

(b) x–z plane

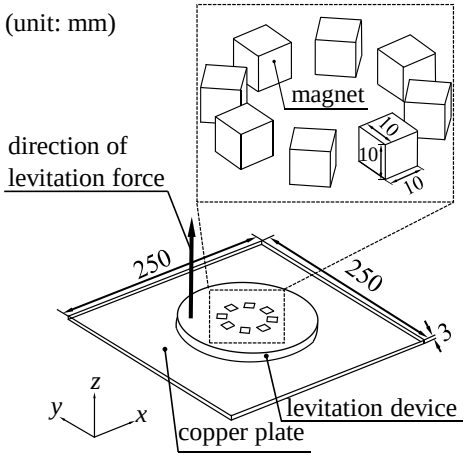

(c) bird's-eye view

Figure 5: Analysis model (magnetic levitation device).

Figure 7 shows the mesh for the magnetic levitation device for MLS. The red frame shown in Figure 7 shows the zero-isosurface in the level set function, and the eight frames are defined by individual level set functions. Comparing Figure 7 with Figure 6, the mesh of the MLS shown in Figure 7 does not need to update mesh data, and it is possible to maintain the shape of the mesh.

In this case, the region that considers the level set functions are described. In the calculating the level set function, provided that all of nodes are calculated, the calculation cost increases.

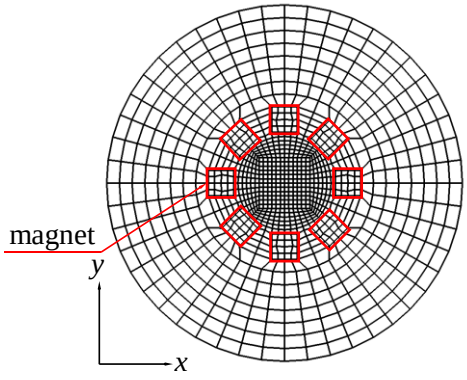

Figure 6: Conventional method mesh (magnetic levitation device).

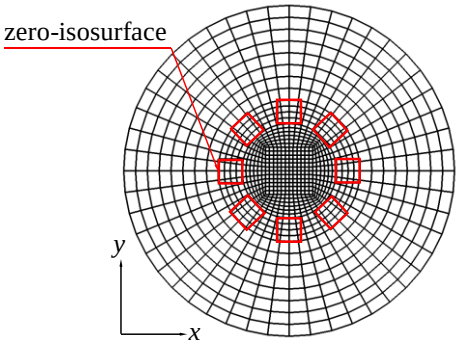

Figure 7: MLS mesh (magnetic levitation device).

Therefore, in this analysis model, the region in which the level set function is considered is set only to the region of magnetic levitation device. In this analysis, the value of the transition width h of the Heaviside function is 0.5 mm.

IV. Analysis Results

A. Basic Verification Model

Figure 8 shows the distribution of eddy currents in the copper plate at the 10th time-step using the conventional method and MLS (h = 0.5 mm). As a result of visualizing the eddy current density, it can be confirmed that the distribution is quite similar in both cases. Figure 9 shows the result of eddy current loss. When the conventional method was considered as criterion, the maximum relative error rate of MLS was less than 5.0 % for all the transition width h.

Figure 10 shows the results for electromagnetic force. When the transition width h is 0.5 mm, the maximum relative error rate is less than 5.0 % could be obtained. The same trend was observed for the eddy current loss.

It can be seen that the accuracy of both the eddy current loss and the electromagnetic force was improved when the value of the transition width h decreases. The reason is that SHF returns 0 or 1, or the value close to 0 or 1 in a narrow section because the gradient of the fifth order function in Figure 3 is sharp when the transition width h decreases.

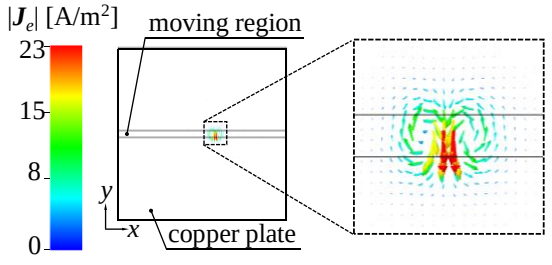

(a) conforming

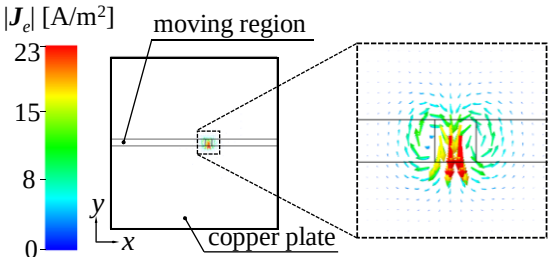

(b) MLS (h = 0.5 mm)

Figure 8: Distribution of eddy current loss (basic verification model).

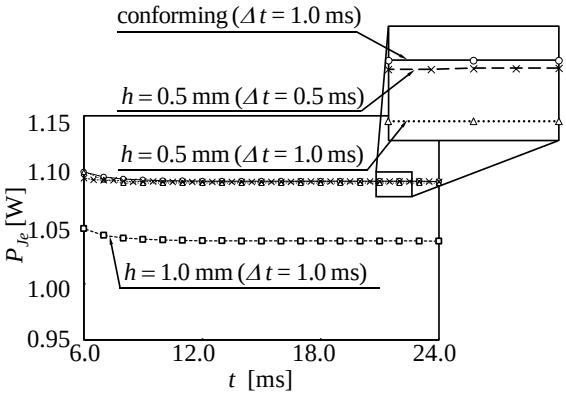

Figure 9: Eddy current loss (basic verification model).

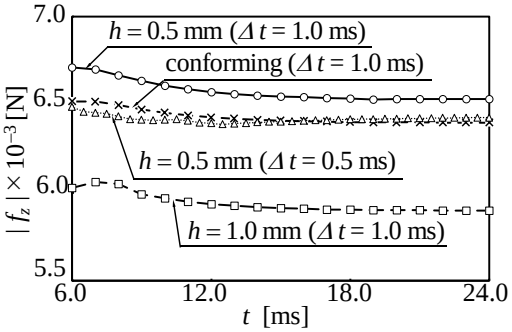

Figure 10: Electromagnetic force (basic verification model).

Furthermore, it was possible to obtain a more accurate result by fixing the value of the transition width h and changing the time-step width. Therefore, it can be seen that MLS can model the movement in accordance with the width of the time-step without updating the mesh information.

Table I shows the average number of iterations in the ICCG method and the result of the elapsed time. Given that similar results were obtained using both methods, it can be seen that the calculation of the level set function in the MLS has limited influence on the overall calculation time. In this model, because the shape of model is simple, all moving regions were divided into parts of a grid. Therefore, it was possible to move only the material constant without updating the mesh data in the conventional method; thus, there was no error in calculation time using either method.

From the above results, it can be seen that MLS is effective for application to simple movements of objects.

TABLE I COMPUTATIONAL EFFORT OF BASIC VERIFICATION MODEL

	average number of itrations. (per time step)	elapsed time[s]
conventional (conforming)	300.4	797
MLS (h = 0.5 mm)	307.7	789
MLS (h = 1.0 mm)	308.7	805

CPU: Intel Core i7 7700K 4.20 GHz & 32.0 GB RAM

B. Magnetic Levitation Device

Figure 11 shows the distribution of eddy current in the copper plate at the 10th time-step using the conventional method and MLS (h = 0.5 mm). Thus, by visualizing the eddy current density, it can be confirmed that the distribution is quite similar in both cases, similar to the previous section. However, in the conventional method, given that the mesh shape is transformed in the vicinity of the magnet, it is assumed that the discretization error is included.

Figure 12 shows the result of the eddy current loss. When the conventional method was considered as criterion, the maximum relative error rate of MLS was 1.1 %.

Figure 13 shows the result of electromagnetic force. The maximum relative error rate of MLS was 2.7 % when the value of levitation force in the conventional method was considered as criterion. As described in the previous paragraph, given that the mesh data was updated by the coordinate transformation in the conventional method, it is assumed that the discretization error is included. Moreover, as shown in Figure 13, it can be seen that the levitation force converges with a fixed value.

Table II shows the average number of iterations in the ICCG method and the elapsed time. In this model, because the number of magnets in this model was set to eight, the level set function was calculated eight times. Therefore, it can be seen that the calculation cost of the coordinate correction in the conventional method is slightly larger than that of the calculation cost for eight calculations of the level set function in MLS.

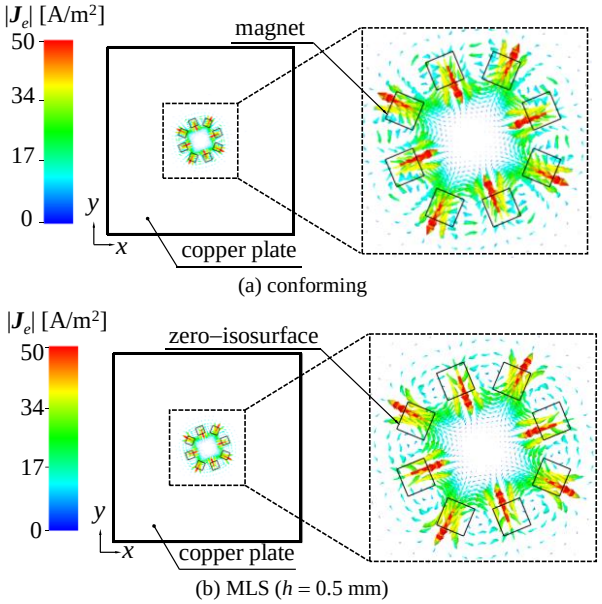

Figure 11: Distribution of eddy current (Magnetic levitation device).

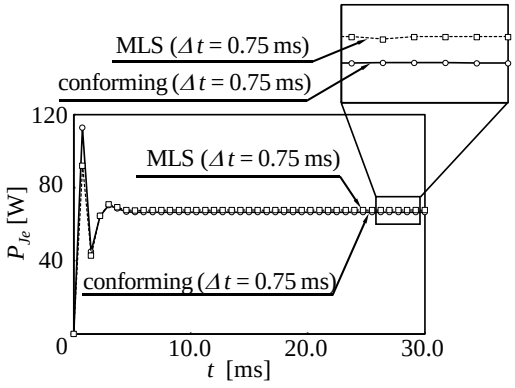

Figure 12: Eddy current loss (magnetic levitation device).

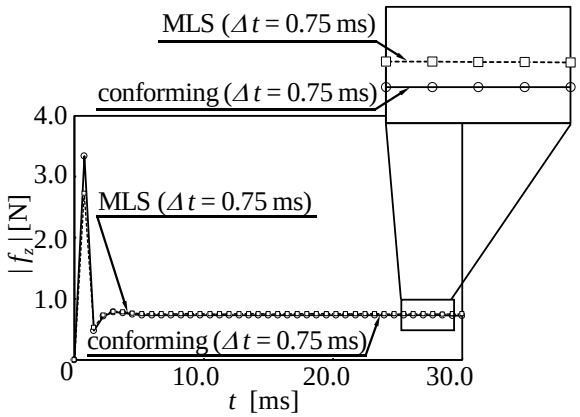

Figure 13: Levitation force (magnetic levitation device).

TABLE II COMPUTATIONAL EFFORT OF MAGNETIC LEVITATION DEVICE

	average number of itrations. (per time step)	elapsed time [s]
conforming (Δt = 0.75 ms)	72.5	224
MLS (Δt = 0.75 ms)	73.3	211

From the above results, it can be seen that MLS can be effectively applied to magnetic levitation device, as shown in the previous section. Moreover, it is expected that this method will mitigate the process of generating a mesh for a complicated model and coordinate transformation associated with the movement of the object.

V. CONCLUSION

In this paper, the method to realize flexible motion of a moving object using the level set function (MLS) was proposed. The performance of the MLS was shown in the analysis models of linearly moving magnet and magnetic levitation device. In these models, the maximum relative error of levitation force derived from MLS was less than 5.0 % in comparison to conventional finite element method. Therefore, it can be seen that MLS can accurately express the moving object without updating mesh data. Moreover, it is expected that the MLS will mitigate the process of generating a mesh for a complicated model.

REFERENCES

[1] Y. Hibino, N. Goto, K. Sugahara, "Development of an eddy current magnetic levitation system with revolving permanent magnets," *The Papers of Joint Technical Meeting on Static Apparatus and Rotating Machinery*, SA-18-22, RM-18-22, pp. 35-37 (2018) (in Japanese).

[2] M. Ebrahimian, M. Khodabakhsh, and G. Golamraz, "An analytical 3-D model for calculating eddy-current damping force for a magnetic levitation system with permanent magnet," *IEEE Trans. Magn.*, vol. 48, no. 9, pp. 2472-2478, Sep. 2012.

[3] K. Muramatsu, Y. Yokoyama, and N. Takahashi, "3D magnetic field analysis using nonconforming mesh with edge elements," *IEEE Trans. Magn.*, vol. 38, no. 2, pp. 433-436, Mar. 2002.

[4] Y. Okamoto, R. Himeno, K. Ushida, A. Ahagon, and K. Fujiwara, "A dielectric heating analysis method with accurate rotational motion of stirrer fan using nonconforming mesh connection," *IEEE Trans. Magn.*, vol. 44, no. 6, pp. 806-809, Jun. 2008.

[5] C. Golovanov, J. L. Coulomb, Y. Marechal, and G. Meunier, "3D mesh connection techniques applied to movement simulation," *IEEE Trans. Magn.*, vol. 34, no. 5, pp. 3359-3362, Sep. 1993.

[6] J. A. Sethian, and A. Wiegmann, "Structural boundary design via level set and immersed interface methods," *J. Comput. Phys.*, vol. 163, no. 2, pp.489-528, Nov. 1999.

[7] Y. Okamoto, H. Masuda, Y. Kanda, R. Hoshino, and S. Wakao, "Convergence acceleration of topology optimization based on level set function using method of moving asymptotes in 3-D nonlinear magnetic field system," *IEEE Trans. Magn.*, vol. 53, no. 6, pp. 806-809, Jun. 2017.

[8] Y.-S. Kim, S.-H. Lee, and H. S. Choi, "Application of the level set method to finite element modeling of moving objects in electromagnetic field," *IEEE Trans. Magn.*, vol. 45, no. 3, pp. 1144-1147, Mar. 2009.

[9] M.-Y. Wang, X. Wang, and D. Guo, "A level set method for structural topology optimization," *Comput. Methods. Appl. Mech. Engrg.*, vol. 192, pp. 227-246, Sep, 2002.

[10] A. Kawamoto, T. Matsumori, S. Yamasaki, T. Nomura, T. Kondoh, and S. Nishiwaki, "Heaviside projection based topology optimization by a PDE-filtered scalar function," *Structural and Multidisciplinary Optimization*, vol. 44, no. 1, pp. 19-24, Jul. 2011.

[11] A. Kameari, "Local force calculation in 3D FEM with edge elements," *International Journal of Applied Electromagnetics in Materials*, vol. 3, pp. 231-240 (1993).

[12] J. Meijerink, and H.A. van der Vorst, "An iterative solution method for linear systems of which the coefficient matrix is a symmetric *M*-matrix," *Mathematics of Computation*, vol. 31, pp. 148-162 (1977).

[13] K. Fujiwara, T. Nakata, and T. Iwashita, "Acceleration of convergence characteristic of the ICCG Method," *IEEE Trans. Magn.*, vol. 29, no. 2, pp. 1958-1961, Mar. 1993.

[14] G. A. Gear, *Numerical Initial Value Problems in Ordinary Differential Equations*. Prentice-Hall, Inc. Englewood Cliffs, New Jersey (1971).

[15] Y. Okamoto, K. Fujiwara, and Y. Ishihara, "Effectiveness of higher order time integration in time domain finite element method," *IEEE Trans. Magn.*, vol. 46, no. 8, pp. 3321-3324, Mar. 2010.

Analysis of penalty parameters for interior penalty Galerkin methods

Sebastian Straßer, Hans-Georg Herzog

Institute of Energy Conversion Technology, Technical University of Munich (TUM), Munich, Germany

Purpose:
The purpose of this paper is to analyse the influence of penalty parameters for an interior penalty Galerkin method, namely, the symmetric interior penalty Galerkin method.

Design/methodology/approach:
First of all, the solution of a simple model problem is computed and compared to the exact solution, which is a periodic function. Afterwards, a two-dimensional magnetostatic field problem described by the magnetic vector potential A is considered. In particular, penalty parameters depending on the polynomial degree, the properties of the elements and the material are considered. The analysis is performed by varying the polynomial degree and the mesh sizes on a structured and an unstructured mesh. Additionally, the penalty parameter is varied in a specific range.

Findings:
Choosing the penalty parameter correctly plays an important role as the stability and the convergence of the numerical scheme can be affected. For a structured mesh, a limiting value for the penalty parameter can be calculated beforehand, whereas for an unstructured mesh, the choice of the penalty parameter can be cumbersome.

Originality/value:
This paper shows that there exist different penalty parameters which can be taken into account to solve the considered problems. One can choose a global penalty parameter to obtain a stable solution, which is a sharp estimation. There has always to be the consideration to guarantee the coercivity of the bilinear form while minimising the number of iterations.

Keywords:
Boundary value problems, Finite element method, Numerical analysis

Published in COMPEL - The international journal for computation and mathematics in electrical and electronic engineering, Vol. 38 No. 5, 2019, ISSN 0332-1649, page 1401 - 1412

Comparison of the Efficiency of E-Core Transformer to Hybrid System with Magnetic Flux Modulation

Ivan Yatchev, Iosko Balabozov
Department of Electrical Apparatus, Technical University of Sofia, Bulgaria,
E-mail: yatchev@tu-sofia.bg, i.balabozov@tu-sofia.bg

***Abstract*—Efficiency of two electromagnetic systems is compared – E-core transformer and hybrid electromagnetic system with magnetic modulation. The latter is created by adding permanent magnet to the construction of the E-core transformer. Coupled electromagnetic field – electric circuit analysis is carried out using COMSOL software. The results show higher efficiency of the hybrid system.**

***Index Terms*—FEM modelling, Hybrid electromagnetic system, Magnetic flux modulation.**

I. Introduction

Permanent magnets in nowadays have improved characteristics, and the constant progress of production technologies leads to a reduction in their price. In addition, demand for energy-efficient devices leads to the development of fundamentally new concepts of electromagnetic devices with built-in permanent magnets. Such devices are hybrid electromagnetic systems with magnetic flux modulation (HEMSMM).

The idea of embedding permanent magnets in electromagnetic devices is not new [1]-[3], but due to the lack of materials with appropriate characteristics, many of them have not been practically realized. By the type of the magnetic system, the studied constructions in nowadays can be grouped as systems with open type magnetic core and systems with closed core. Systems from closed type core are presented in patents [10]-[12], where different configurations of pulsed power fed control coils are used in such a way to obtain redistribution of magnetic flux from permanent magnet. Moreover, the magnetic flux created by the coils is added to the flux created by the permanent magnet. In [4]-[7], open-type constructions are considered, whereby the magnetic flux from the permanent magnet is separated from the flux created by the control coils by using air gaps. Different methods for controlling of magnetic flux from a permanent magnet are presented in [8]. A construction which consist several permanent magnets and two coils is described in [9], where the magnetic field generated by control coil is perpendicular to the field from magnets. Is same construction the basic principle is the saturation of the magnetic system. Such a construction is energy linear generator that is shown in [13]. The study of such constructions and the search for new ones is aimed at improving their efficiency and achieving a coefficient of performance (COP) greater than 1. Some theoretical aspects and examples for COP are given in [14]. There is also a conceptual diagram of permanent magnet motor where asymmetrical regaining is used to achieve better coefficient of performance.

The main purpose of this work is to make a comparison of energy efficiency of two similar constructions of electromagnetic systems. They are similar to E-core transformer but differ in the number and position of the coils. One of the constructions also has permanent magnets (PM), that are incorporated in the magnetic core. PM generate constant magnetic fluxes which are redirected when the coils are fed. Comparison is based on computer simulation using FEM.

II. Studied Construction

A previous research by the authors is published in [15], where a HEMSMM with one PM and two output coils is modelled and studied. The main part of construction studied in the present paper is shown in Figure 1. There are two variants of the modelled construction, one with PM and one without. To use the same mesh of finite elements in the computer models and to minimize the error, the PM regions are not removed but replaced with air in variant without magnets.

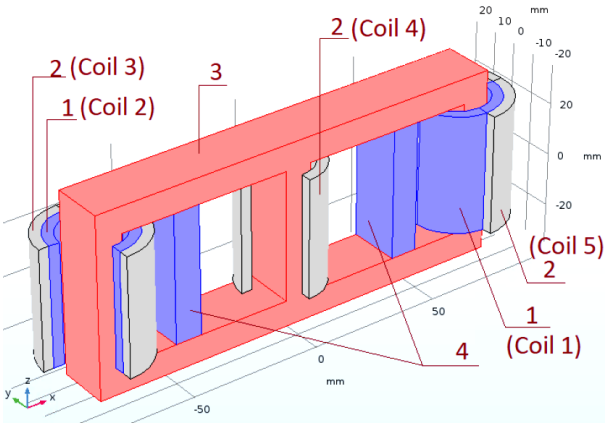

A) Variant 1 - with permanent magnets (HEMSMM)

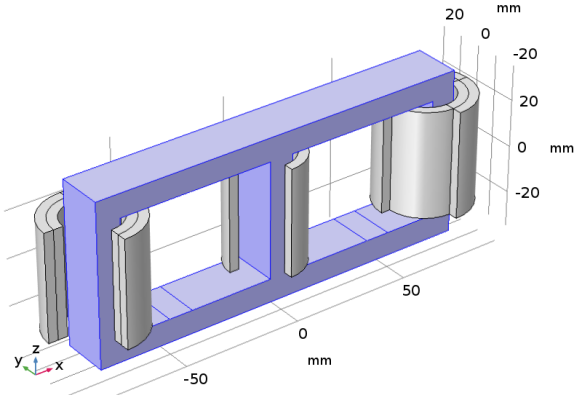

B)Variant 2 – without permanent magnets (E-core transformer)

Figure 1: Main construction of modelled HEMSMM

The main construction parts are:

1. Input (control) coils - Coil 1 and Coil 2;
2. Output (signal) coils - Coil 3, Coil 4 and Coil 5;
3. Ferromagnetic core;
4. Permanent magnets.

III. FEM Modelling of the Systems without and with PM

Coupled electromagnetic filed– electric circuit problem is solved in COMSOL software [16] and result are analysed. In Figure 2 modelled electric circuit together with generated power pulses from V1 and V2 is shown.

The parameters of input and output coils are defined in magnetic field interface and are linked to the electric circuit. Two pulsed power sources are used for power feeding of input coils L1 and L2. Different power modes can be achieved by changing the parameters of electric pulses. The output coils L3, L4 and L5 are loaded over resistors R3, R4 and R5.

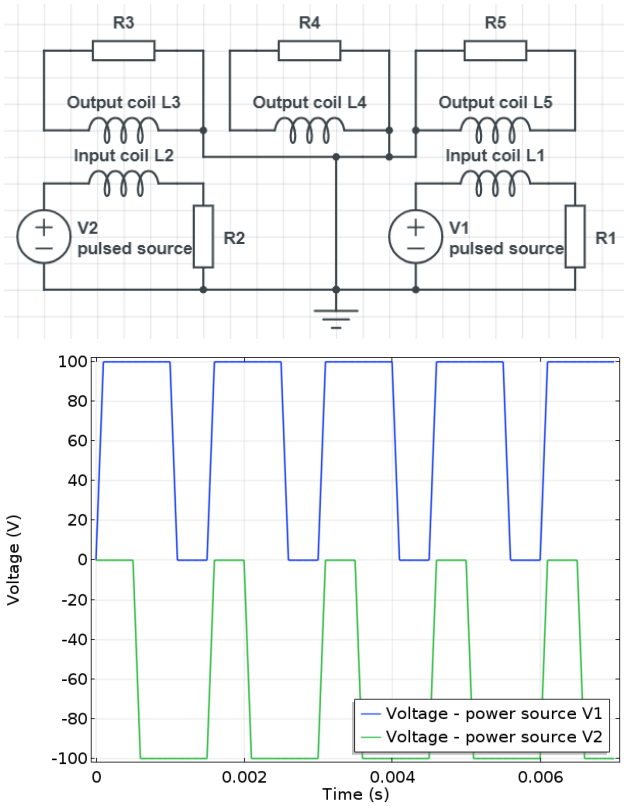

Figure 2: Modelled electric circuit and voltage pulses from power sources V1 and V2

For solving of the models with PM two steps are needed. First stationary task with respect to the electromagnetic field is solved. In this step the electric circuit does not participate. Results for the electromagnetic field due to permanent magnets have been obtained. During the second step, a time-dependent task is solved, where as an initial condition the results for the electromagnetic field obtained in the calculation of step 1 is taken in account. The coils are connected to the electric circuit shown in Figure 2 and modeled in the same model.

According to COMSOL user's guide [16], magnetostatics equation is achieved from Ampere's law for static cases:

$$\nabla \times \mathbf{H} = \mathbf{J} \tag{1}$$

Using the definitions of magnetic vector potential, $\mathbf{B} = \nabla \times \mathbf{A}$ and the constitutive relationship, $\mathbf{B} = \mu_0 (\mathbf{H} + \mathbf{M})$, Ampere's law for static case can be written as:

$$\nabla \times (\mu_0^{-1} \nabla \times \mathbf{A} - \mathbf{M}) = 0 \tag{2}$$

For time dependent step the equation is transformed to:

$$\sigma \frac{\partial \mathbf{A}}{\partial t} + \nabla \times (\mu_0^{-1} \nabla \times \mathbf{A} - \mathbf{M}) = N.I/S \tag{3}$$

The circuit equation are:

$$Coil\ 1:\ V_1 = R_1.I_1 + \partial\Psi_1/\partial t \tag{4}$$

$$Coil\ 2:\ V_2 = R_2.I_2 + \partial\Psi_2/\partial t \tag{5}$$

$$Coil\ 3:\ -\partial\Psi_3/\partial t = R_3.I_3 \tag{6}$$

$$Coil\ 4:\ -\partial\Psi_4/\partial t = R_4.I_4 \tag{7}$$

$$Coil\ 5:\ -\partial\Psi_5/\partial t = R_5.I_5 \tag{8}$$

The *B-H* curve of the used ferromagnetic material for the magnetic core is shown in Figure 3.

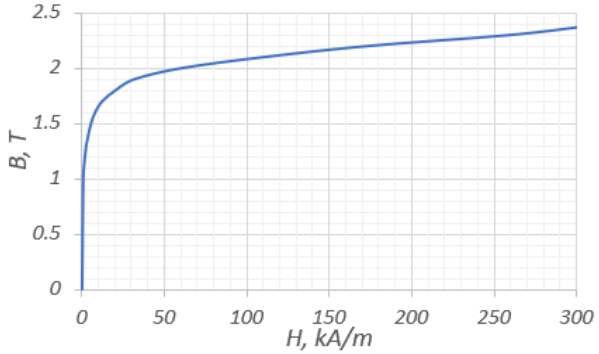

Figure 3: B-H curve of used ferromagnetic material in the modelling

In Figure 4 and Figure 5, magnetic flux density for model without (E-core transformer) and with PM (HEMSMM) is presented. By power feeding the input coils, the magnetic flux changes its path which produce signal to the output coil.

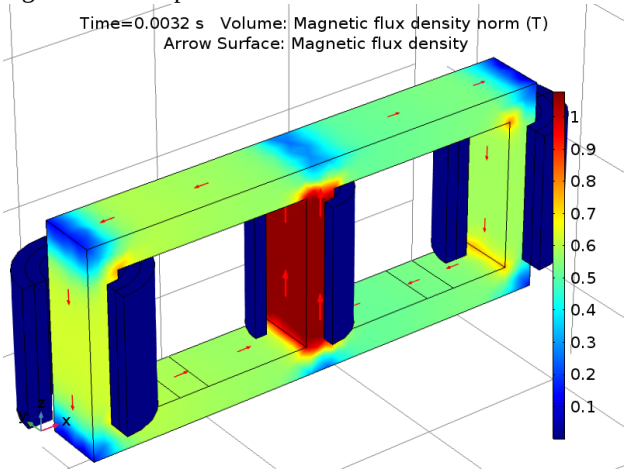

Figure 4: Magnetic flux density of construction without PM

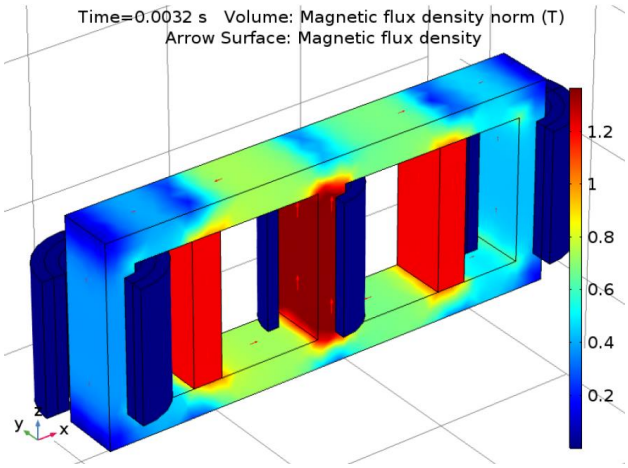

Figure 5: Magnetic flux density of construction with PM.

IV. Results from Simulations

In Figure 6 and 7 electric parameters of input coils for the two variants (with and without PM) are shown.

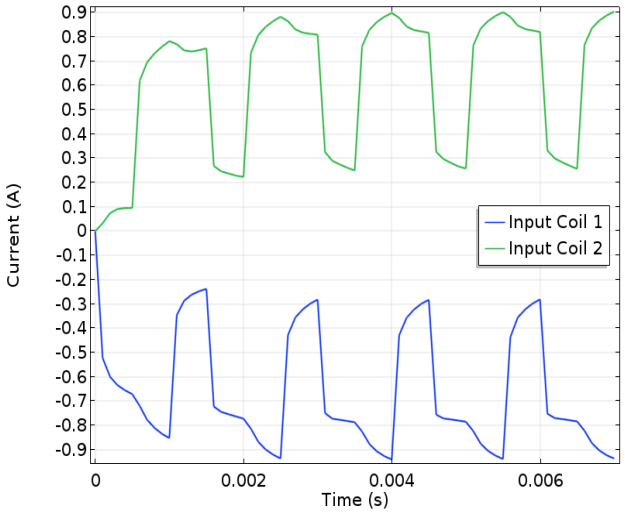

A) Current through input coils with PM

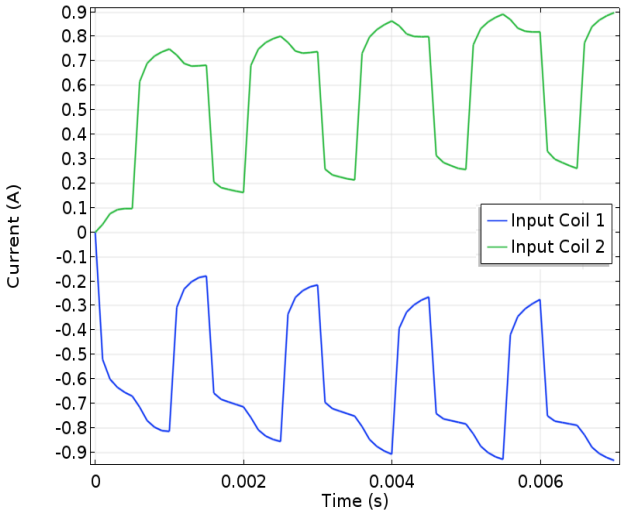

B) Current through input coils without PM

Figure 6: Current through input coils.

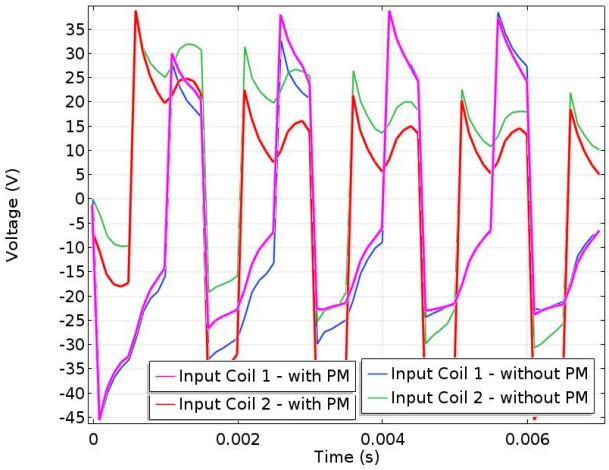

Figure 7: Voltage of input coils for variants with and without PM.

The output coils current for construction with and without permanent magnets is shown in Figure 8.

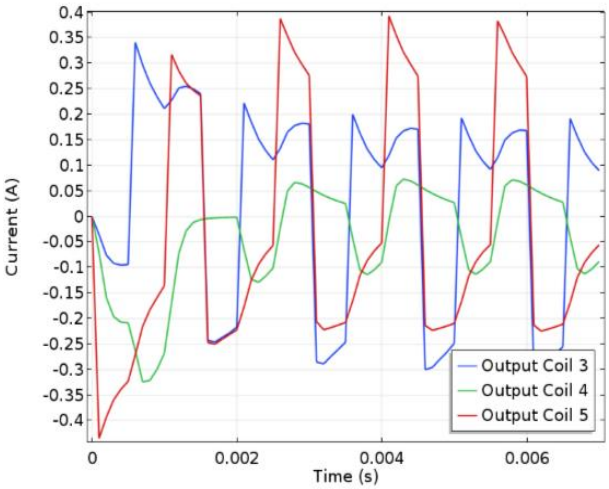

A) Current through output coils with PM

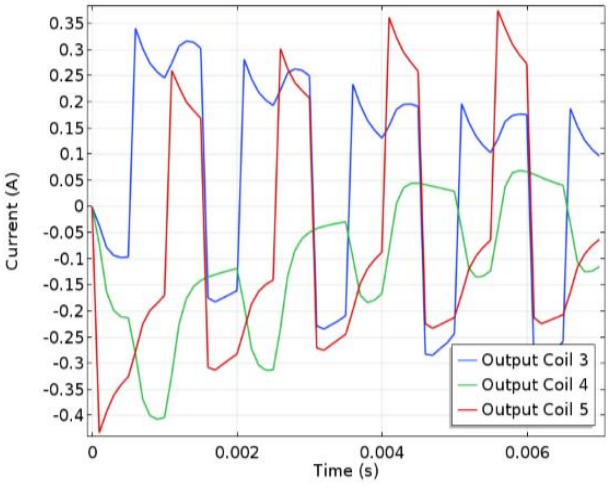

B) Current through output coils without PM

Figure 8: Current through output coils.

The instantaneous value of the electrical power achieved in each of the output coils for construction with permanent magnets is shown in Figure 9.

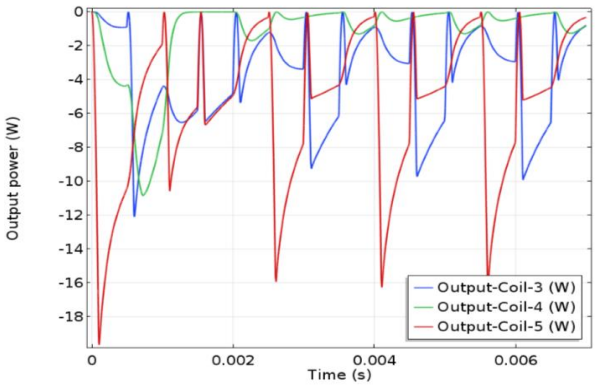

Figure 9: Power of output coils for construction with PM.

In Figure 10, comparison of average input to the output power for both studied variants is presented. It is clear that the transient process in the construction with PM is more than two times shorter compared to the construction without PM.

A) Average power for variant with PM

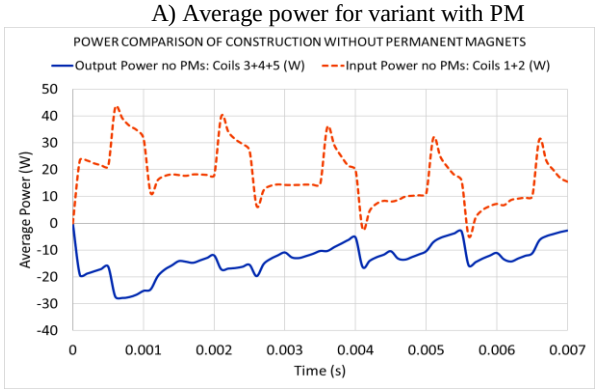

B) Average power for variant without PM

Figure 10: Comparison of average input-output power

Table I shows the change in efficiency when permanent magnets are added to the construction. The average power values are calculated after the transition process ends and are for the same time period for both models (with and without PM).

TABLE I

COMPARISON OF THE EFFICIENCY OF MODELLED CONSTRUCTIONS

	Average Input Power	Average Output power	Efficiency
Variant without PMs	11.884 [W]	10.017 [W]	84.29 %
Variant with PMs	10.752 [W]	9.980 [W]	92.82 %
Difference between studied variants			8.53 %

V. CONCLUSION

The developed computer simulations and the results obtained allow determining the positive influence of the flux created by a permanent magnet on the efficiency of the electromagnetic system. The transient process is two times shorter in the construction with PM, which is an advantage when using it in applications that require frequent switching on and off. To verify the simulation results, experimental prototypes of similar devices will be developed.

VI. ACKNOWLEDGMENT

The present work is supported by the National Science Fund of Bulgarian Ministry of Education and Science, Project No. DN 17/13.

REFERENCES

[1] Toffolo, D.S, Flux switching transformer, U.S. Patent 3087108 A, 1963. [https://tinyurl.com/ycr637bh] – 01.10.2018

[2] Subieta-Garron, "Transformer in combination with a permanent magnet". U.S. Patent 3368141, 1968.

[3] Bramanti, D., Magnetic Amplifier, U.S. Patent 4675615 A, 1987. [https://www.lens.org/lens/patent/US_4675615_A] - 01.10.2018

[4] Asaoka, K., Static magnet dynamo for generating electromotive force based on changing flux density of an open magnetic path U.S. Patent 5926083 A, 1999.

[5] Ivanov, V., Motionless Generator. [https://tinyurl.com/y7pbpv6z] - 01.10.2018

[6] Willis, R. Electrical Generator. U.S. Patent App. WO 2009/065219 A1, 2009. [http://rexresearch.com/willis/willis.htm] -01.10.2018 [https://tinyurl.com/ybv389vu] - 01.10.2018

[7] Flynn, C.J., Talsoe, N.B., & Childress, J.J. Parallel Path Magnetic Technology for High Efficiency Power Generators and Motor Drives. Space Tech.& Applic.: 3rd Symp.New Frontiers & Future Concepts. AIP Conf. Proceedings, 813, 2006, pp. 1205−1212.

[8] Flynn, C.J., Methods for controlling the path of magnetic flux from a permanent magnet and devices incorporating the same. US Patent No: US 6,246,561 B1, 2001

[9] Gunderson, G., Solid State Electric Generator, US Patent 2006/0163971 A1. [https://tinyurl.com/y7b44n9y] - 01.10.2018

[10] Ueno, T., Higuchi, T., Novel composite of magnetostrictive material and piezoelectric actuator for coil-free magnetic force control, Sensors and Actuators A 129 (2006), 251–255, doi:10.1016/j.sna.2005.09.061

[11] Patrick, Stephen, et al., Motionless electromagnetic generator, European Patent EP 1446862 B1, 2013. [https://www.lens.org/lens/patent/EP_1446862_B1] - 01.10.2018

[12] Patrick, Stephen, et al., Motionless electromagnetic generator, US 6362718 B1, 2002. [https://tinyurl.com/yacopbfz] - 01.10.2018

[13] Kunel, H., Procedures and Devices for Energy Production, Patent DE3024814, 1982, [https://tinyurl.com/yc64vbah] - 01.10.2018

[14] Walters, M., et al., Introducing the Practice of Asymmetrical Regauging to Increase the Coefficient of Performance of Electromechanical Systems, Center for Power Electronics Systems, Department of Electrical and Computer Engineering, North Carolina A & T State University Greensboro, NC 27411 USA [https://tinyurl.com/y8jg934x] – 01.10.2018

[15] Yatchev, I., Balabozov, I., Hinov, K., Minchev, M., Gueorgiev, V., "Electromagnetic Field Analysis of a Hybrid Electromagnetic System with Magnetic Flux Modulation with One Permanent Magnet and Two Collecting Coils", XXth International Symposium on Electrical Apparatus and Technologies (SIELA2018), 3-6 June 2018, Bourgas, Bulgaria, DOI:10.1109/SIELA.2018.8447108, ISBN:978-1-5386-3420-2

[16] COMSOL Multiphysics 5.3 User's Guide.

Exploiting the T(x) function in fast hysteresis models for transient circuit simulations

Johann Wilhelm, Werner Renhart

Institute for Fundamentals and Theory in Electrical Engineering, Graz University of Technology, Graz, Austria

Purpose:
The purpose of this paper is to investigate an alternative to established hysteresis models.

Design/methodology/approach:
Different mathematical representations of the magnetic hysteresis are compared and some differences are briefly discussed. After this, the application of the T(x) function is presented and an inductor model is developed. Implementation details of the used transient circuit simulator code are further discussed. From real measurement results, parameters for the model are extracted. The results of the final simulation are finally discussed and compared to measurements.

Findings:
The T(x) function possesses a fast mathematical formulation with very good accuracy. It is shown that this formulation is very well suited for an implementation in transient circuit simulator codes. Simulation results using the developed model are in very good agreement with measurements. Research limitations/implications For the purpose of this paper, only soft magnetic materials were considered. However, literature suggests, that the T(x) function can be extended to hard magnetic materials. Investigations on this topic are considered as future work.

Originality/value:
While the mathematical background of the T(x) function is very well presented in the referenced papers, the application in a model of a real device is not very well discussed yet. The presented paper is directly applicable to typical problems in the field of power electronics.

Keywords:
Magnetic hysteresis, Transient analysis, Transient simulation

Published in COMPEL - The international journal for computation and mathematics in electrical and electronic engineering, Vol. 38 No. 5, 2019, ISSN 0332-1649, page 1427 - 1440

Dynamic hysteresis modeling for soft magnetic composites based on isotropic vector play model and Cauer ladder network

Naoya Watanabe, Yasuhito Takahashi, Koji Fujiwara

Department of Electrical Engineering, Doshisha University, Kyotanabe, Japan

Purpose:
This paper aims to propose an effective modeling method of dynamic hysteresis properties for soft magnetic composite (SMC) core using an equivalent circuit representation. Because the eddy currents flowing inside iron powder particles should be considered, it is well known that an accurate magnetic field analysis of the SMC core in a wide range of excitation frequency is not easy. To overcome this difficulty, a dynamic hysteresis modeling based on the standard Cauer circuit is investigated.

Design/methodology/approach:
In the proposed method, the first inductance represents the static magnetic property of the SMC, and the latter part represents the dynamic effect because of the eddy currents. The values of the circuit elements were determined by an optimization method based on symmetric loops measured at several frequencies. To verify the validity of the proposed modeling method, finite-element analyses of a ring core inductor and an alternating current reactor were performed.

Findings:
By comparing the simulated and measured magnetic properties, the necessity to consider magnetic hysteresis in the equivalent circuit model is clarified. Furthermore, the frequency-dependent inductances of practical reactors can be obtained from the finite-element analysis combined with the proposed method.

Originality/value:
This paper demonstrates the significance of determining the circuit parameters in the equivalent circuit for dynamic hysteresis modeling based on the measured magnetic properties. The effectiveness of the proposed method is verified by comparing frequency-dependent inductances of two kinds of reactors between the simulation and measurement.

Keywords:
Magnetic hysteresis, Soft magnetic materials, Finite-element method, Equivalent circuit model, Cauer circuit

Published in COMPEL - The international journal for computation and mathematics in electrical and electronic engineering, Vol. 38 No. 5, 2019, ISSN 0332-1649, page 1413 - 1426

Modelling the penetration of magnetic flux in thin superconducting films with shell transformations

Loic Burger, Christophe Geuzaine, Francois Henrotte, Benoit Vanderheyden

Department of Electrical Engineering and Computer Science, Universite de Liege Faculte des Sciences Appliquees, Liege, Belgium

Purpose:
Finite element (FE) models are considered for the penetration of magnetic flux in type-II superconductor films. A shell transformation allows boundary conditions to be applied at infinity with no truncation approximation. This paper aims to determine the accuracy and efficiency of shell transformation techniques in such non-linear eddy current problems.

Design/methodology/approach:
A three-dimensional H - Φ formulation is considered, where the reaction field is calculated in the presence of a uniform applied field. The shell transformation is used in the far-field region, and the uniform applied field is introduced through surface terms, so as to avoid infinite energy terms. The resulting field distributions are compared against known solutions for different geometries (thin disks and thin strips in the critical state, square thin films). The influence of the shape, size and mesh quality of the far-field regions are discussed.

Findings:
The formulation is shown to provide accurate results for a number of film geometries and shell transformation shapes. The size of the far-field region has to be chosen in such a way to properly capture the asymptotic decay of the fields, and a practical procedure to determine this size is provided.

Originality/value:
The importance of the size of the far-field region in a shell transformation and its proximity to the conducting domains are both highlighted. This paper also provides a numerical way to apply a constant magnetic field in a given region, while the source, on which only the far-field behaviour of the applied field depends, is excluded from the model.

Keywords:
Eddy currents, Finite element method, Computational electromagnetics, Superconducting materials

Published in COMPEL - The international journal for computation and mathematics in electrical and electronic engineering, Vol. 38 No. 5, 2019, ISSN 0332-1649, page 1441 - 1452

The impact of human age on the amount of absorbed energy from mobile phone

[1]Dejan B. Jovanovic, [2]Vladimir Stankovic, [1]Nenad N. Cvetkovic, [2]Dejan Krstic, [1]Dragan Vuckovic

[1]Faculty of Electronic Engineering, University of Nis, Nis, Serbia
[2]Faculty of Occupational Safety, University of Nis, Nis, Serbia

Purpose:
The purpose of this paper is to determine the impact of human age on the distribution of electric field and absorbed energy that originates from a mobile phone

Design/methodology/approach:
This research was performed for frequencies of 900, 1800 and 2100MHz, which are used in a mobile communication system. To obtain the most accurate results, 3D realistic model of the childs head has been created whereby the dimensions of this model correspond to the dimensions of a seven-year-old child. Distribution of the electric field and specific absorption rate (SAR) through the childs head was obtained by numerical analysis based on the finite integration technique.

Findings:
The results discover that amount of absorbed energy is greater in the surface layers of the childs head model when the electromagnetic (EM) characteristics of tissues are adjusted for the child. This deviation corresponds to different EM characteristics of biological tissues and organs of an adult person compared to a child.

Originality/value:
The proposed procedure offers the model for accurate estimation and quality analysis of SAR and EM field distribution inside child head tissue.

Keywords:
Communication technologies, Electromagnetic fields, Optimal design, Electromagnetic compatability

Published in COMPEL - The international journal for computation and mathematics in electrical and electronic engineering, Vol. 38 No. 5, 2019, ISSN 0332-1649, page 1465 - 1478

Peculiarities of Calculating Forced Electromagnets Shunt Windings Heating in Transient Modes

[1]Yevgen Bajda, [1]Borys Klymenko, [1]Michael Pantelyat, [1]Olena Korol, [2]Yurii Yelanskyi
[1]Department for Electrical Apparatus, National Technical University "Kharkiv Polytechnic Institute",
Kyrpychova Str. 2, UA-61002 Kharkiv, Ukraine
[2]Yuzhnoe State Design Office, Krivorozhskaya Str. 3, UA-49008 Dnipro, Ukraine

Abstract—**An analytical expression is obtained that makes it possible to calculate the volumetric density of sources of transient heating of shunt windings, in which as they are heated up, the volumetric density of sources integrally decreases, but at the same time, at points with higher temperature, the source density is higher than at points with lower temperature. Using the example of temperature calculations of miniature gas distributors, it is shown that at forced heating of the electromagnets in shunt windings significant temperature drops, reaching 35% of the maximum temperature, as well as a slight effect on the heating of surrounding objects, in particular, steel of the magnetic core, are observed.**

***Index Terms*—Finite Element Method, forced heating, shunt windings.**

I. INTRODUCTION

In the International Electrotechnical Vocabulary (IEV) [1], as well as in the well-known explanatory dictionaries [2], the term "shunt winding" directly refers to electric machines, although the use of this term can naturally be extended to other objects, in which there are windings connected in parallel to the load or power source. In the same IEV, the term "shunt release" is defined as "a release energized by a source of voltage: IEV 441-16-41". Structurally, shunt release is a device containing an electromagnet, the winding of which is connected through a switching element in parallel with a voltage source. It should be borne in mind that "release" is "a device, mechanically connected to a mechanical switching device, which releases the holding means and permits the opening or the closing of the switching device: IEV 441-15-17".

Shunt windings are also used in undervoltage releases of circuit breakers, in various relays [3], contactors, electromagnetic clutches and brakes, blocking electromagnets and in the designs of a number of other electrical apparatus. One example of the use of shunt windings of DC electromagnets are high-speed electromagnetic valves for gas distribution devices. Such valves are used, in particular, in modern rocket and space technology as jet micromotors for the executive bodies of the rocket stabilization systems [4], as well as for controlling movement of spacecrafts in space (orientation, stabilization, orbit correction, maneuver, etc.) [5].

At the design stage of objects with DC electromagnets, it is necessary to perform calculations of the thermal state of shunt windings, the accuracy of which can affect the size and mass of the object as a whole. Despite the wide prevalence of shunt windings of DC electromagnets, there are no publications on calculation of transients of their forced heating, as far as the authors know.

The computational capabilities of modern computers make it possible to perform mathematical modelling of static and dynamic thermal processes in various objects by numerical solution of corresponding equations of mathematical physics [6]. Here, despite high performance of modern computers, solution of 3D problems causes significant difficulties both in terms of describing geometry of the object, and in terms of time spent on calculations. At the same time, absolute majority of shunt windings of a wide variety of apparatus with high degree of adequacy can be considered as axisymmetrical 2D objects in a cylindrical coordinate system, which significantly speeds up computational procedures when calculating static and dynamic heating processes of such windings.

The peculiarity of the process of forced heating of shunt windings is the presence of significant temperature differences at various points in the cross section of the winding, and hence significant differences in values of volumetric densities of heat sources. Here, this should take into account the fact that in the process of heating of the winding its resistance increases, therefore, the volumetric density of sources integrally decreases, but at the same time, at points with higher temperature at each moment in time, the density of sources is greater than at points with lower temperature.

The goal of this paper is to clarify the mathematical model and the algorithm for calculating forced heating of shunt windings.

II. DESCRIPTION OF THE TECHNIQUE PROPOSED

Carrying out thermal calculations using computer codes that use the Finite Element Method requires careful preparatory work related to description of geometry of the electromagnet on the r - z plane passing through its axis of symmetry, dividing the cross section of the electromagnet with shunt winding and objects adjacent to the electromagnet involved in heat exchange process (in aggregate, the calculation regions) into subdomains that can be considered homogeneous from the point of view of physical properties, determination of boundaries of these subdomains and differential equations describing processes in these subdomains, as well as specifying initial and boundary conditions.

Thermal calculation or determination of temperature fields ϑ in an object containing a shunt winding is performed by numerically solving a system of transient heat transfer equations within computational region. This

system consists of n (corresponding to the number of subdomains) Fourier differential heat transfer equations (for subdomains with internal heat sources) and Laplace (for subdomains without internal sources). This system is the following [7], [8]:

$$c_{\mathrm{w}} \cdot \gamma_{\mathrm{w}} \cdot \frac{\partial \vartheta}{\partial t} + \mathrm{div}(-\lambda_{\mathrm{w}} \cdot \mathrm{grad}\vartheta) = q\,, \tag{1}$$

$$c_k \cdot \gamma_k \cdot \frac{\partial \vartheta}{\partial t} + \mathrm{div}(-\lambda_k \cdot \mathrm{grad}\vartheta) = 0\,,\ k = 1, 2, \ldots, n-1, \tag{2}$$

where (1) refers to the subdomain that corresponds to the cross section of the winding, and totality of equations (2) refers to other subdomains. In (1), (2): c_{k} is the specific heat of the material at arbitrary point of the k-th subdomain, γ_k is the material density of the k-th subdomain, λ_k is the specific thermal conductivity of the material at arbitrary point of the k-th subdomain, c_{w} is the specific equivalent heat capacity of the winding considered as a uniform body, γ_{w} is the equivalent density of the winding, λ_{w} is the equivalent thermal conductivity of the winding, q is the volumetric density of heat sources at arbitrary point of the subdomain that corresponds to the cross section of the winding.

To perform thermal calculation of the electromagnet in transient mode, it is necessary to set initial and boundary conditions [7], [8]. For the beginning of transient ($t = 0$), initial conditions should be formulated. We assume that before start of the heating process, the electromagnet was continuously in ambient air environment with initial temperature ϑ_{i}, therefore all parts of the electromagnet had the same temperature, that is, for all points we have the following initial conditions [7], [8]:

$$\vartheta(0) = \vartheta_{\mathrm{i}}. \tag{3}$$

Boundary conditions should be specified on the surface of calculation area. It is considered that the most correct are conditions of the third kind (the Robin conditions) [7], [8]:

$$-\lambda \cdot \mathrm{grad}_{\mathrm{n}}\vartheta = K \cdot (\vartheta - \vartheta_{\mathrm{a}})\,, \tag{4}$$

where λ is the thermal conductivity of the material of the body located near the boundary with environment, $\mathrm{grad}_{\mathrm{n}}\vartheta$ is the normal component of the temperature gradient near surface of the body, ϑ is the temperature on surface of the body, ϑ_{a} is the ambient air temperature, K is the heat transfer coefficient from surface of the body.

Some multiphysics codes provide the option to calculate the heat transfer coefficient at natural convection by solving the Navier-Stokes and thermal radiation equations, based on Stefan-Boltzmann law [8].

One of these subdomains, namely the subdomain that corresponds to cross section of the winding, differs from others in at least two ways: firstly, this subdomain is not homogeneous, because the winding consists of not one material like other subdomains (steel, insulation material, air, etc.), but of several materials with significantly different properties, at least of copper and insulation, and secondly, this subdomain is active – it contains internal heat sources with volumetric density q, which is non-uniformly distributed over cross section of the subdomain, and depends on temperature ϑ at particular point of the cross section. When performing thermal calculations, winding is usually considered as a kind of homogeneous body with some equivalent characteristics: the equivalent specific heat capacity c_{w}, the equivalent density γ_{w}, and the equivalent thermal conductivity λ_{w}.

In this paper, the authors proceed from assumption that the winding consists of only two components — copper and insulation, and volume fraction of copper is equal to the fill factor k_{w}, therefore, to calculate the equivalent density γ_{w} and the equivalent specific heat capacity c_{w}, we can recommend the following formulas:

$$\gamma_{\mathrm{w}} = \gamma_{\mathrm{cu}} \cdot k_{\mathrm{w}} + \gamma_{\mathrm{i}} \cdot (1 - k_{\mathrm{w}})\,, \tag{5}$$

$$c_{\mathrm{w}} = (c_{\mathrm{cu}} \cdot k_{\mathrm{w}} \cdot \gamma_{\mathrm{cu}} + c_{\mathrm{i}} \cdot (1 - k_{\mathrm{w}}) \cdot \gamma_{\mathrm{i}}) / \gamma_{\mathrm{w}}\,, \tag{6}$$

where γ_{cu}, γ_{i} are, respectively, the density of copper and internal insulation, c_{cu}, c_{i} are, respectively, the specific heat capacity of copper and internal insulation.

Methods for calculating the equivalent thermal conductivity λ_{w} of windings were considered in the works of a number of authors in the 30 s - 60 s of the last century [7] , [8], [9]. In those papers, empirical formulas obtained by processing experimental data for impregnated windings were presented. Among them there is the formula that we used in our calculations:

$$\lambda_{\mathrm{w}} = k \cdot \lambda_{\mathrm{i}} \cdot (d / \Delta)^{p}\,, \tag{7}$$

where k, p are, respectively, the empirical coefficient and the exponent (recommended values: $k = 1.225$; $p = 0.5$), λ_{i} is the thermal conductivity of internal insulation, d is the diameter of the winding wire, Δ is the thickness of the wire insulation.

In well-known classical studies on heat transfer in bodies with internal sources [7], [8], [9], two options for determining the volumetric density q of the heat sources are usually considered: either as some average constant values:

$$q = \mathrm{const} \tag{8}$$

or as linear dependencies:

$$q = q_0 \cdot (1 + \alpha_0 \cdot \vartheta), \tag{9}$$

where q_0 is the density of heat sources at temperature 0 °C, α_0 is the temperature coefficient of resistance of material of the winding wire, referred to temperature 0 °C, ϑ is the temperature at arbitrary point of the body.

At calculating such windings, the following factors should be taken into account: 1 – when the winding is heated, its resistance increases, and therefore, at constant supply voltage U, the power P and the average value of the volumetric density of heat sources decrease, but 2 – at specific time at point of the cross section of the winding with higher temperature, the resistance of the turn will be greater than at point with lower temperature, therefore, the volumetric density of heat sources at point with higher temperature will be greater than at point with lower temperature, too.

We take into account these two factors and the assumption of a uniform distribution of winding copper, and hence the current i over the surface S of the cross section of the winding or winding space of height a and width b, the area of which is equal to the product $a \times b$ (Fig. 1), that in each elementary area of size drdz copper occupies a part equal to the fill factor k_{w}, and the rest of the region is insulation.

Volumetric density of heating power source at arbitrary point with coordinates (r, z) on the winding section plane is equal to ratio of the elementary power dP allocated in the volume element dV = l · dr · dz, where l is the length of the current tube at this point, to value of this volume:

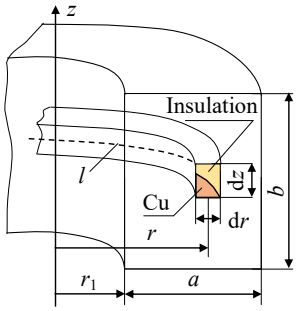

Figure 1: To determination of volumetric density of the heat sources in the winding.

$$q = \frac{\mathrm{d}P}{\mathrm{d}V}. \tag{10}$$

Volume dV is determined by the expression

$$\mathrm{d}V = l \cdot \mathrm{d}r \cdot \mathrm{d}z, \tag{11}$$

and the power dP can be determined using the current element di and the conductivity dG of elementary current tube:

$$\mathrm{d}P = \frac{(\mathrm{d}i)^2}{\mathrm{d}G}. \tag{12}$$

Expression for definition of dG can be represented as:

$$\mathrm{d}G = \frac{k_\mathrm{w} \cdot \mathrm{d}r \cdot \mathrm{d}z}{\rho_0 \cdot (1+\alpha_0 \cdot \vartheta) \cdot l}, \tag{13}$$

where ρ_0 is the specific resistance of winding material at temperature 0 °C.

Calculated equivalent current density J in the cross section of the winding:

$$J = \frac{i \cdot N}{S} = \frac{U \cdot N}{R \cdot S}, \tag{14}$$

where i is the current in the winding at arbitrary time, R is the resistance of the winding at corresponding time, N is the number of turns of the winding, U is the voltage at the terminals of the winding.

Using (14), we can determine the current element

$$\mathrm{d}i = J \cdot \mathrm{d}r \cdot \mathrm{d}z = \frac{U \cdot N}{R \cdot S} \cdot \mathrm{d}r \cdot \mathrm{d}z, \tag{15}$$

and the elementary power:

$$\mathrm{d}P = \frac{(\mathrm{d}i)^2}{\mathrm{d}G} = \frac{U^2 \cdot N^2 \cdot \rho_0 \cdot (1+\alpha_0 \cdot \vartheta) \cdot l \cdot \mathrm{d}r \cdot \mathrm{d}z}{R^2 \cdot S^2 \cdot k_\mathrm{w}}, \tag{16}$$

Substituting (16) into (11), we obtain:

$$q = \frac{\mathrm{d}P}{\mathrm{d}V} = \frac{U^2 \cdot N^2 \cdot \rho_0 \cdot (1+\alpha_0 \cdot \vartheta) \cdot l \cdot \mathrm{d}r \cdot \mathrm{d}z}{R^2 \cdot S^2 \cdot k_\mathrm{w} \cdot l \cdot \mathrm{d}r \cdot \mathrm{d}z} =$$

$$= \frac{U^2 \cdot N^2 \cdot \rho_0 \cdot (1+\alpha_0 \cdot \vartheta)}{R^2 \cdot S^2 \cdot k_\mathrm{w}}. \tag{17}$$

As a result of simple transformations, we obtain the final expression for determining volumetric density of heat sources at arbitrary point of the winding section at arbitrary point in time:

$$q = \frac{U^2}{R_\mathrm{i} \cdot V} \cdot \frac{(1+\alpha_0 \cdot \vartheta) \cdot (1+\alpha_0 \cdot \vartheta_\mathrm{i})}{(1+\alpha_0 \cdot \vartheta_\mathrm{av})^2}, \tag{18}$$

where R_i is the winding resistance at the initial temperature; ϑ_av is the average temperature of the winding; V is the winding volume:

$$V = a \cdot b \cdot \pi \cdot (2 \cdot r_1 + a), \tag{19}$$

where r_1 is the inner diameter of winding space (Fig. 1).

For windings with known dimensions and winding data, (18) can be written as:

$$q = \frac{U^2}{R_0 \cdot V} \cdot \frac{(1+\alpha_0 \cdot \vartheta)}{(1+\alpha_0 \cdot \vartheta_\mathrm{av})^2}, \tag{20}$$

where R_i is the winding resistance at temperature 0 °C.

Formula (20) can be used in the calculations of both non-stationary and stationary temperature fields.

III. Numerical Results Obtained

As an example, we present results of thermal calculations of one of designed gas distribution devices. Calculations are carried out by numerical solution of the heat transfer equations (1) and (2) with initial condition (3) and boundary conditions (4). Heat transfer coefficients took into account natural convection (solving the Navier-Stokes equations) and thermal radiation (Stefan-Boltzmann law). The calculations took into account features of heating shunt windings discussed above.

Initial data:

- area of the winding space of the winding – $S = 72.6 \cdot 10^{-6}$ m^2 (72.6 mm^2)
- winding volume – $V = 4650 \cdot 10^{-9}$ m^3 (4650 mm^3)
- number of turns of the winding – $N = 1155$
- winding wire diameter – $d = 0.2 \cdot 10^{-3}$ m
- winding fill factor – $k_\mathrm{w} = 0.5$
- ambient air temperature, initial winding temperature – $\vartheta_\mathrm{a} = 35$ °C
- winding resistance at temperature 35°C – $R_{35} = 42.87$ Ω
- ambient air pressure – $p_\mathrm{a} = 0.1$ MPa
- winding supply voltage – $U = 33.5$ V
- temperature coefficient of resistance wire (copper) at 0 °C – $\alpha_0 = 0.00423$ K^{-1}

Sketch of the gas distribution device and its geometric model are shown in Fig. 2.

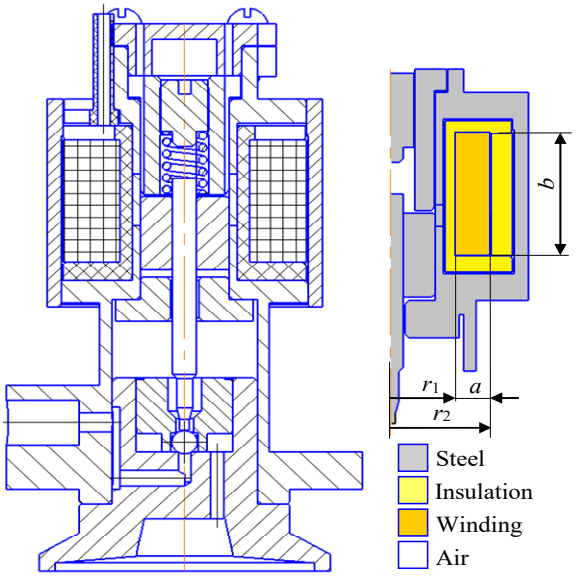

Figure 2: The sketch of the gas distribution device and its geometric model.

Mode of operation of the gas distribution device is short-term, the operating time is 70 s. In accordance with technical requirements, the average winding temperature at maximum allowable voltage of power supply (33.5 V) should not exceed 150 °C.

Figure 3 shows the calculated curve of the transient of average winding temperature (solid line). As it can be seen, average temperature of the winding during 70 s of heating increases from 35 °C to 112 °C and does not reach maximum permissible value. On the same graph, solid lines show curves demonstrating how the resistance R of the winding and the power P dissipated in it change in time.

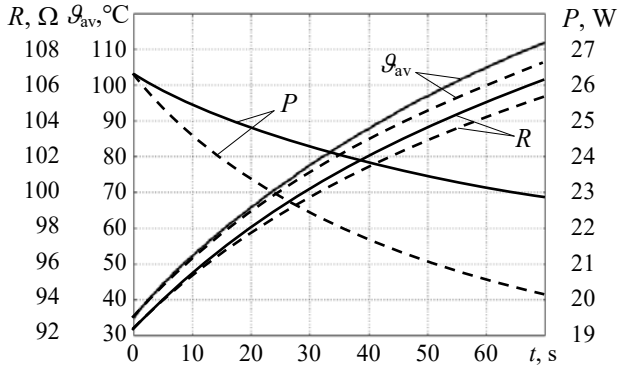

Figure 3: Transients of the average temperature of the winding, the resistance of the winding and the power dissipated in it.

A characteristic feature of this calculation is that heating is calculated not for a separate winding, but for the entire electromagnet and adjacent objects, taking into account heat exchange between the winding, magnetic core and adjacent objects.

At forced heating of shunt windings, significant temperature drops are observed both inside and outside the winding, as evidenced by the picture of the temperature field of the electromagnet 70 s after the beginning of the transient, shown in Fig. 4.

It must be emphasized that the picture of temperature field presented in Fig. 4, refers to the entire electromagnet, and from this picture it is difficult to separate the temperature distribution directly in the winding and estimate the temperature rise in it. Such estimation can be done by graphs presented in Fig. 5 (solid lines) showing temperature distribution along the winding perimeter, as well as radial temperature distribution in the cross section of the winding with maximum temperature.

From these graphs it can be seen that in this winding, despite its miniature (winding thickness is only 4.4 mm, and width is 16.5 mm), the temperature rise in it 70 s after the start of forced heating is 29.6 °C with average temperature of 112 °C, the maximum temperature of 120.6 °C and the lowest temperature of 91 °C at the corner point.

Such a significant temperature rise is characteristic specifically for forced heating process of the winding, in which the objects surrounding the winding, first of all the magnetic core, due to the significant heat capacity, do not have time to heat up.

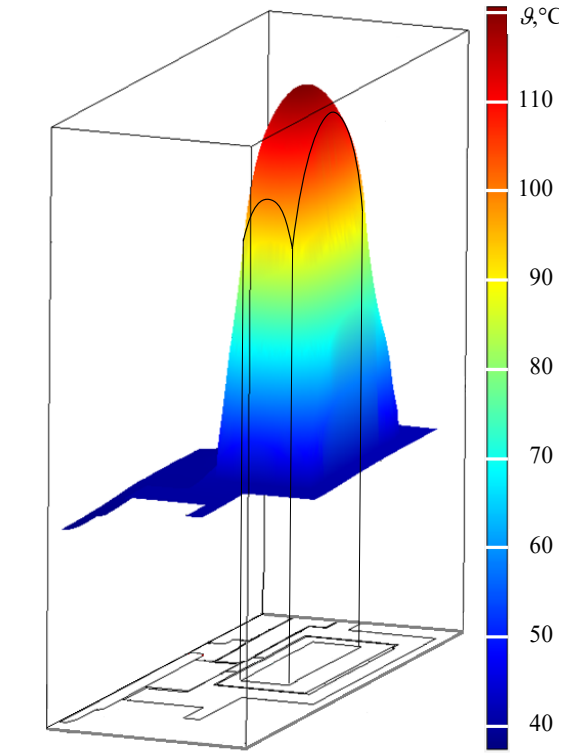

Figure 4: The spatial image of the picture of temperature field of the electromagnet 70 s after the beginning of the transient.

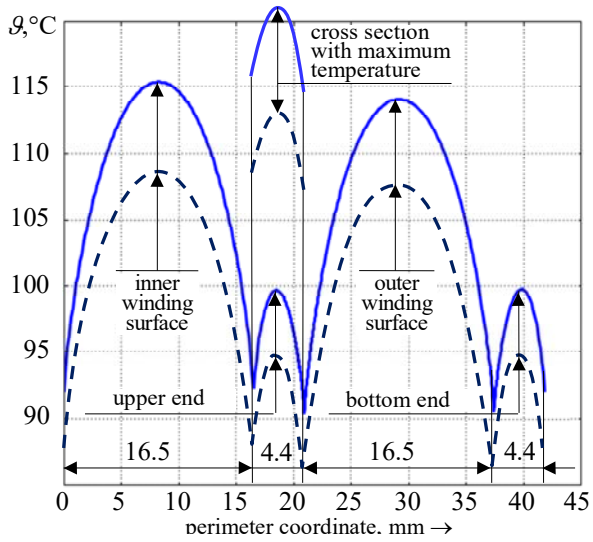

Figure 5: Temperature distribution around the perimeter of the electromagnet winding and in the cross section with the maximum temperature 70 s after the beginning of the transient.

As can be seen from the picture of temperature field of the electromagnet shown in Fig. 4, 70 s after the beginning of the transient, the temperature of the magnetic core increased by no more than 5 °C and, thus, does not perform the function of a radiator, which helps to cool the winding and equalize the temperature at various points of its cross section.

The initial value of volumetric density of heat sources at all points in the cross section of the winding is constant: $q_i = U^2 / (R_i \cdot V) = 5.63 \cdot 10^6$ W/m^3. 70 s after the beginning of transient, the volumetric density of heat sources is distributed irregularly over the cross section of

the winding. The graphic picture of this distribution for the considered example is shown in Fig. 6.

Attention is drawn to the fact that degree of this irregularity is not very significant. For example, if the maximum temperature value (122 °C) in the cross section of the winding (Fig. 5) exceeds the lowest temperature value (91 °C) by 34%, then the maximum value of volumetric density of heat sources ($5.00 \cdot 10^6$ W/m^3) exceeds the smallest value ($4.75 \cdot 10^6$ W/m^3) by only 5.2%.

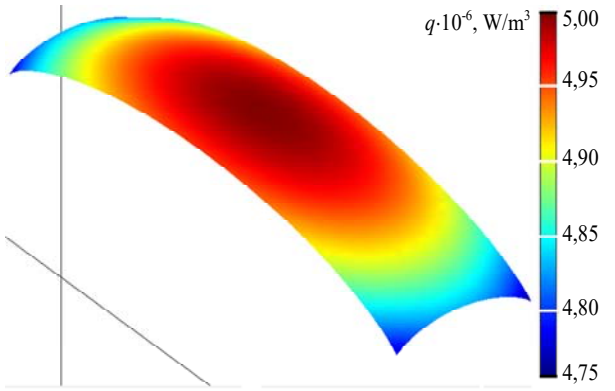

Figure 6: Volumetric density of heat sources distribution 70 s after the beginning of the transition process.

Above calculations took into account specifics of heating of shunt windings — integral decrease in the volumetric density of sources as the winding is heated up and irregular distribution of the source density over the cross section of the winding at any given time, namely, at points with higher temperature the source density is greater than at points with lower temperature.

It is of interest to compare obtained results with results of calculations, provided that at each particular moment in time the density of heat sources is assumed to be the same at all points of the cross section. In this case, the density of heat sources should be calculated by the formula:

$$q = \frac{U^2}{R \cdot V} = \frac{U^2 \cdot (1 + \alpha_0 \cdot \vartheta_1)}{R_i \cdot (1 + \alpha_0 \cdot \vartheta_{av}) \cdot V} = \frac{U^2}{R_0 \cdot (1 + \alpha_0 \cdot \vartheta_{av}) \cdot V} \quad (21)$$

In this case, at calculating heating of the electromagnet with shunt winding, the volumetric density of heat sources, decreasing in time from initial value ($5.00 \cdot 10^6$ W/m^3), at each moment in time is distributed irregularly over the winding cross section and 70 s after the beginning of the transient drops to $4.33 \cdot 10^6$ W/m^3 which is 11% less than the average q value ($4.88 \cdot 10^6$ W/m^3) in the first version.

Results of calculation of transients of the change in the average temperature, resistance of the winding and the power released by it are shown in Fig. 3 by dotted lines. In this case, the average temperature 70 s after the beginning of the transient is equal to 105.6 °C at the maximum temperature of 113.3 °C and the lowest temperature of 82 °C, which is 7% - 8% less than values obtained in calculations using (20) in determination q values.

The results of calculation of temperature on the perimeter of the winding (Fig. 5, dashed lines) turn out to be about as small, although the value of the temperature difference between the most and least heated points remains almost unchanged.

Figure 7 shows the calculated temperature distribution curves in sections with maximum temperatures 70 s after the beginning of the transition process, obtained using (20) to determine q (dotted line), and using (21) to determine q (dashed line).

In the considered examples, 70 s after the beginning of the transient, a significant part of the heat dissipated in the winding is given to the insulation frame and the compound filling the space between the outer part of the winding and the yoke of the electromagnet, where the temperature rises from 35 °C to 70 °C - 100 °C. Therefore, forced heating process in these examples cannot be considered as adiabatic. Calculations show that during adiabatic heating, winding temperature 70 s after the beginning of transient reaches 162 °C, which is much higher than calculated average temperature (112 °C).

Figure 7 shows one more curve – the result of calculating temperature distribution in the cross section with the maximum temperature in stationary mode (thin line). This calculation was carried out at reduced voltage of the power source of 10.15 V. This voltage was chosen so that the maximum temperature value in stationary mode was equal to the maximum temperature under conditions of forced heating 70 s after the beginning of the transient (120.6 °C) when the power supply voltage is 33.5 V. As you can see, under conditions of forced heating, the temperature of the magnetic core increased by only 5 °C - 6° C, while under conditions of stationary heating, the temperature of the magnetic core increased significantly – to 106 °C - 107 °C , and the temperature rise in the winding did not exceed 5 °C - 6 °C.

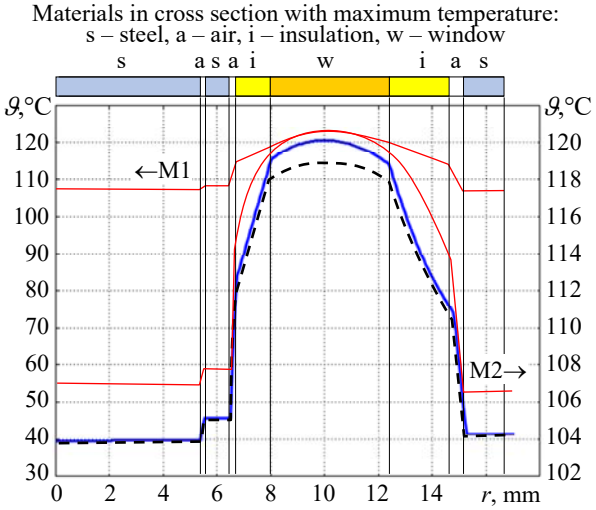

Figure 7: Comparison of temperature distribution curves in cross section with maximum temperature in conditions of forced and stationary heating.

It should be borne in mind that thermal calculations are not an end in themselves – they allow to form initial data for electromagnetic calculations and for determining traction forces and response times, which in many cases is the main result of the calculation of electromagnet. As a result, the errors made during thermal calculations lead to errors in subsequent electromagnetic, force and dynamic calculations.

For example, lowering of the result of calculating the average temperature leads to overestimation of the result of calculation of the traction force of electromagnet, and as a result, the designed electromagnet may turn out to be inoperable. Calculating the temperature fields of the windings, including at their forced heating, by numerical solution of differential heat transfer equations using the Finite Element Method taking into account the approaches considered in this paper, improves accuracy of calculating thermal and, as a result, electromagnetic, force and dynamic characteristics of electromagnets, and increases quality of their design.

IV. CONCLUSIONS

1. An analytical expression is obtained that allows to calculate the volumetric density of sources of transient heating of shunt windings, in which as they are heated, the volumetric density decreases integrally, but at the same time, at points with higher temperatures, the source density is greater than at points with less temperature.

2. Calculations carried out show that at the forced heating of electromagnets, in shunt windings significant temperature rises, reaching 35% of the maximum temperature, as well as a weak effect on the heating of objects surrounding the winding, in particular, steel of the magnetic core, are observed.

REFERENCES

[1] Electropedia: The World's Online Electrotechnical Vocabulary. http://www.electropedia.org.
[2] Collins Dictionary. https://www.collinsdictionary.com/.
[3] N. Sterl, *Power Relays*. *EH-Schrack Components AG*. Vienna: Tyco Electronics Austria GmbH, 1997.
[4] V.P. Olejnik, Yu.A. Yelanskyi and L.G. Kaluger, "Mathematical modelling of a gas distributor of the carrier rocket gas-jet control system," *Space Technology. Missile Weapons*. Issue 1 (113), pp. 59-66, 2017 (in Russian).
[5] N.M. Beliaev, N.P. Belik and E.I. Uvarov, *Jet Control Systems for Spacecrafts*. Moscow: Mechanical Engineering, 1979, 232 p. (in Russian).
[6] P.P. Silvester and R.L. Ferrari, *Finite Elements for Electrical Engineers*. 3rd ed. Oxford: Oxford University Press, 1996, 494 p.
[7] H.S. Carslaw and J.C. Jaeger, *Conduction of Heat in Solids,* 2nd ed. Oxford: Oxford University Press, 1959, 510 p.
[8] A.V. Lykov, *Heat Transfer Theory*. Moscow: Higher School, 1967, 600 p. (in Russian)
[9] A.M. Zalesskyi and G.A. Kukekov, *Thermal Calculations of Electrical Apparatus*. Leningrad: Energy, 1967, 378 p. (in Russian).

Low-power electrical impedance tomography spectroscopy

Juliana Padilha Leitzke, Hubert Zangl

Alpen-Adria University Klagenfurt, Klagenfurt, Austria

Purpose:
This paper aims to present an approach based on electrical impedance tomography spectroscopy (EITS) for the determination of water and ice fraction in low-power applications such as autarkic wireless sensors, which require a low computational complexity reconstruction approach and a low number of electrodes. This paper also investigates how the electrode design can affect the reconstruction results in tomography.

Design/methodology/approach:
EITS is performed by using a non-iterative method called optimal first order approximation. In addition to that, a planar electrode geometry is used instead of the traditional circular electrode geometry. Such a structure allows the system to identify materials placed on the region above the sensor, which do not need to be confined in a pipe. For the optimization, the mean squared error (MSE) between the reference images and the obtained reconstructed images was calculated.

Findings:
The authors demonstrate that even with a low number of four electrodes and a low complexity reconstruction algorithm, a reasonable reconstruction of water and ice fractions is possible. Furthermore, it is shown that an optimal distribution of the sensor electrodes can help to reduce the MSE without any costs in terms of computational complexity or power consumption.

Originality/value:
This paper shows through simulations that the reconstruction of ice and water mixtures is possible and that the electrode design is a topic of great importance, as they can significantly affect the reconstruction results.

Keywords:
EITS, Multi-frequency EIT

Published in COMPEL - The international journal for computation and mathematics in electrical and electronic engineering, Vol. 38 No. 5, 2019, ISSN 0332-1649, page 1480 - 1492

A new approach to couple FEM calculated inductivity matrix with a non-linear magnetic circuit

*Gergely Koczka, †Kurt Preis and *Robert Labinsky
*Transformers Weiz, Siemens Inc, Austria, Elingasse 3, 8160 Weiz, Austria
†Institute of Fundamentals and Theory in Electrical Engineering, Graz University of Technology, 8010 Graz, Austria

***Abstract*—Modeling variable shunt reactors (VSR) to analyze switching transients is necessary to avoid the appearance of high inrush current. In this paper an efficient FEM2D-magnetic network hybrid model will be introduced to reduce the simulation time and increase the accuracy of the transient inrush currents.**

***Index Terms*— FEM, Inrush current, Numerical analysis, Shunt reactor**

I. INTRODUCTION

Modeling the non-linear behavior of a variable shunt reactor (VSR) with the finite element method can be time consuming. There are already simplified models for switching impulse simulation [1], but the accuracy of these models can be increased with a bit more accurate approch.

To use a 2D axisymmetric finite element method (FEM2D) for modeling the core and winding of the shunt reactor, the calculated impedance has even a better accuracy to the measurements as it is prescribed by the standard (maximal allowed deviation is 2.5%) (IEEE C57.21-2008 7.2.1). The common technique to couple field calculation method with magnetic and electric circuit models [2] is using a strong coupling between the field equation system and the electric circuit equations. These methods can lead to a robust method, if the windings have to be modeled accurate and the non-linearity must be taken into account within the FEM analysis.

In this paper a mathematic approximation will be introduced, which can be used to reduce the number of equations and to create a very small magnetic circuit model coupled with the impedance matrix of the FEM2D model, having the same steady state accuracy as the FEM2D model.

II. IMPEDANCE MATRIX

A. FEM calculated matrix

The conductors of the windings are designed so, that the eddy currents in the copper have no influence in the impedance. Therefore, the impedance matrix can be determined by the flux linkages of the magneto-static field.

Using the A formulation in the finite element analysis the flux linkage can be determined as follows [3]:

$$\int_{\Omega} \nabla\times\mathbf{N}_k \cdot \nu\nabla\times\mathbf{A}_j d\Omega = \int_{\Omega} \nabla\times\mathbf{N}_k \cdot \mathbf{t}_{0,j} d\Omega \qquad (1)$$

$$L_{FEM,i,j} = -\int_{\Omega} \mathbf{t}_{0,i} \cdot \nabla\times\mathbf{A}_j d\Omega \qquad (2)$$

where $\mathbf{N}_k$ is the k-th basis function in the discretized FEM problem, $\mathbf{A}_j$ is the j-th magnetic vectorpotential, $\mathbf{t}_{0,i}$ and $\mathbf{t}_{0,j}$ are the impressed electric vectorpotential for 1A of the i-th and j-th electrical branch and $L_{FEM,i,j}$ is the j-th element of the i-th row in the inductance matrix. $\nabla\times\mathbf{t}_{0,i}$ and $\nabla\times\mathbf{t}_{0,j}$ are also called the turn densities of the i-th and j-th electrical branches.

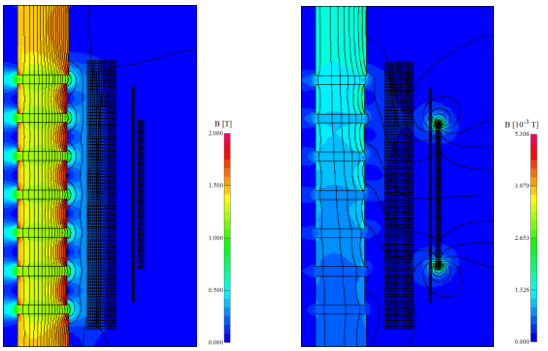

Figure 1: FEM2D calculated field in the iron core and in the winding block (1 phase). Left: field due to maximal current; Right: field due to distribution currents

B. Magnetic circuit

To write the equations of the magnetic circuit the magnetic scalar potential (Φ) will be used in the nodes of the circuit and impressed electric vectorpotential (t_0), where a magnetic branch is connected to a coil, or an eddy-current region (see Figure 2, 3). Eddy current regions are modelled with a short-circuited winding with only one electrical turn.

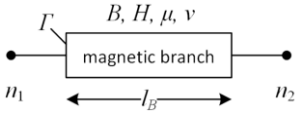

Figure 2: Magnetic branch to consider material properties.

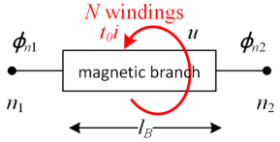

Figure 3: Magnetic branch coupled with voltage excitation.

The magnetic field intensity inside the magnetic branches can be written as follows:

$$H = t_0 \cdot i - \nabla\Phi\,, \tag{3}$$

with

$$\nabla\Phi = \frac{\Phi_{n_1} - \Phi_{n_2}}{l_B}\,, \tag{4}$$

and

$$t_0 = \frac{1}{l_B} N \tag{5}$$

where Φ_{n_1} and Φ_{n_2} are values of the magnetic scalar potential in the n_1-th and n_2-th node, i is the current in the corresponding electric branch, l_B is the length, Γ is the area of the magnetic branch and N is the number of turns in the corresponding winding. With this formulation the equation

$$\oint H d\ell = I \tag{6}$$

is satisfied automatically, where I denotes the overall current flowing through a closed circle in the magnetic circuit's path.

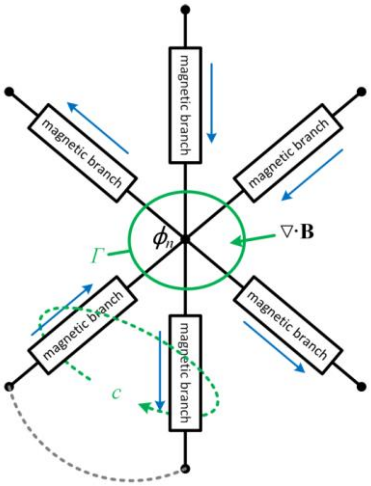

Figure 4: meaning of divergence **B** around a node in the magnetic circuit.

To determine the flux in the magnetic branches the following equation must be solved:

$$\nabla\cdot\mathbf{B} = 0 \Leftrightarrow \iint_{\Gamma} \mathbf{B} d\Gamma = 0 \Leftrightarrow \sum_{\Gamma_i \subset \Gamma} B_i \cdot \Gamma_i = 0\,, \tag{6}$$

where B_i is the flux density in the i-th magnetic branch and Γ_i is the area of the i-th magnetic branch (see Figure 4).

The voltage of the coils can be determined as follows [3]:

$$\int_{\Omega} t_0 \cdot \frac{\partial}{\partial t} \mathbf{B} d\Omega = 0 \Leftrightarrow \sum_{i=1}^{n_B} t_{0,i} \cdot \frac{\mathrm{d}}{\mathrm{d}t} B_i \cdot l_{B,i} \cdot \Gamma_i = u\,, \tag{7}$$

where n_B is the number of magnetic branches in the circuit model.
With these notations – and by applying the material relationship between B and H – the differential equation system results in

$$\begin{bmatrix} \mathbf{R} & 0 \\ 0 & \mathbf{S}_\rho \end{bmatrix} \begin{bmatrix} \mathbf{i} \\ \mathbf{x} \end{bmatrix} + \frac{\mathrm{d}}{\mathrm{d}t} \begin{bmatrix} \mathbf{V}_\mu & \mathbf{g}_\mu \\ \mathbf{g}_\mu^T & \mathbf{C}_\mu \end{bmatrix} \begin{bmatrix} \mathbf{i} \\ \mathbf{x} \end{bmatrix} = \begin{bmatrix} \mathbf{u} \\ 0 \end{bmatrix} \tag{8}$$

where $\mathbf{R}$ contains the winding resistances, $\mathbf{S}_\rho$ the resistances of the eddy-current branches, **i** the winding currents and **x** the eddy-currents and the magnetic scalar potentials in the magnetic circuit nodes. The sub-matrixes in equation (8) can be determined as follows:

$$\mathbf{V}_\mu = t_0^T \cdot \mu \cdot t_0 \cdot l_B \cdot \Gamma\,, \tag{9}$$

$$\mathbf{g}_\mu = -t_0^T \cdot \mu \cdot l_B \cdot \Gamma \cdot \nabla\,, \tag{10}$$

$$\mathbf{C}_\mu = \nabla^T \cdot \mu \cdot l_B \cdot \Gamma \cdot \nabla\,. \tag{11}$$

Impedance matrix of the magnetic circuit can be determined from (8) with the Schur-complement method:

$$L_{MN} = \mathbf{V}_\mu - \mathbf{g}_\mu \mathbf{C}_\mu^{-1} \mathbf{g}_\mu^T \tag{12}$$

III. Coupling the results

Let us define a very simplified magnetic circuit model for the geometry of an air-gapped-core shunt reactor (see.: Figure 5).

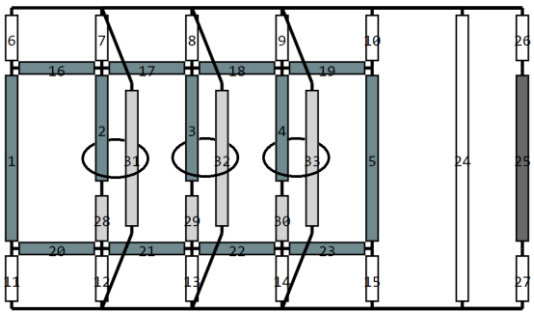

Figure 5: Magnetic circuit model of a 3-phase reactor. Loops around magnetic branches are representing the winding blocks. Each block can have multiple electrical branches.

In our example, we have a 3/2 core type variable shunt reactor (3 main and 2 return limbs). The magnetic circuit model represents the core, the air volumes near the winding block, the air volume inside the tank and the tank (see Table I.).

TABLE I
MAGNETIC BRANCH DESCRIPTIONS

Branch number(s) in Figure 5	Description
2, 3, 4	Effective iron volumes of the main limbs
28, 29, 30	Effective air volumes of the air gaps in the main limbs
31, 32, 33	Air volume outside the main limbs, but inside the winding blocks
1, 5	Return Limb
16 – 23	Iron parts of the yoke
24	Air volume outside the winding blocks but inside the tank
6 – 15, 26, 27	Air volumes between yoke and tank
25	Tank wall

An eddy-current electric branch will be added around the branch representing the tank wall.

To keep the magnetic circuit as simple as possible, it will be generated without the magnetic air-branches between the windings. This means that the t_0 for the main- and regulation windings corresponding to the same limb have the difference only by the number of their electrical turns. This leads to a singular equation system, due to each part of a winding around the same limb is coupled to the same branches in the magnetic circuit. In case of a gapped core reactor the t_0 can be coupled to linear magnetic (air) branches, e.g. in fig. 5 the winding block of the first phase is coupled to the magnetic branches 28 and 31, the second phase to 29 and 32 and the third phase to 30 and 33. In that case the sub-matrix $\mathbf{V}_\mu$ is block diagonal (in this example in Figure 5 one block per phase) depending only from linear material (see (9)) and it is also singular (its rank is only 3).

The steady state impedance matrix of the magnetic circuit can be determined by fixing the non-linear permeability to a linearized steady state permeability (μ_{steady}) and applying the equation (12):

$$L_{MN,steady} = \mathbf{V}_{\mu_{steady}} - \mathbf{g}_{\mu_{steady}} \mathbf{C}^{-1}_{\mu_{steady}} \mathbf{g}^T_{\mu_{steady}} . \qquad (13)$$

to achive the accuracy of FEM calculated impedance matrix, the matrix $L_{MN,steady}$ – which is the impedance matrix for the whole 3-phase system – can be manipulated in that way:

$$\tilde{L}_{MN,steady} = \begin{bmatrix} L_{FEM} & L_{MN,1,2} & L_{MN,1,3} \\ L_{MN,2,1} & L_{FEM} & L_{MN,2,3} \\ L_{MN,3,1} & L_{MN,3,2} & L_{FEM} \end{bmatrix}, \qquad (14)$$

where $L_{MN,i,j}$ -s are the mutual inductances between the i-th and j-th phase of the $L_{MN,steady}$.

The calculation of a modified $\mathbf{V}_\mu$ matrix in the equation (12), can be done as follows:

$$\tilde{\mathbf{V}}_\mu = \tilde{L}_{MN,steady} + \mathbf{g}_{\mu_{steady}} \mathbf{C}^{-1}_{\mu_{steady}} \mathbf{g}^T_{\mu_{steady}} . \qquad (15)$$

The ordinary differential equation (8) corresponding to the magnetic circuit model can be modified as:

$$\begin{bmatrix} \mathbf{R} & 0 \\ 0 & \mathbf{S}_\rho \end{bmatrix} \begin{bmatrix} \mathbf{i} \\ \mathbf{x} \end{bmatrix} + \frac{\mathrm{d}}{\mathrm{d}t} \begin{bmatrix} \tilde{\mathbf{V}}_\mu & \mathbf{g}_\mu \\ \mathbf{g}^T_\mu & \mathbf{C}_\mu \end{bmatrix} \begin{bmatrix} \mathbf{i} \\ \mathbf{x} \end{bmatrix} = \begin{bmatrix} \mathbf{u} \\ 0 \end{bmatrix}. \qquad (16)$$

The reason, why this mathematical coupling works, is because of a good choice of t_0 -s, so the matrix $\mathbf{V}_\mu$ will be linear. In case of air-gapped iron core shunt reactors, the t_0 -s can be coupled to air-magnetic branches in the core (air-gap branches, as in the presented example). In the case of the Figure 5 example, these branches are the 28-th and 31-th for phase 1, the 29-th and the 32-th for phase 2 and the 30-th and 33-th for phase 3. The definition of $\tilde{\mathbf{V}}_\mu$ concludes, that the steady state solution of the modified system is the same as the FEM steady state. For time stepping methods considering the nonlinearity of the magnetic network with this approach is also no problem, because the matrix $\tilde{\mathbf{V}}_\mu$ must be assembled only once, due to it is independent of any nonlinear magnetic branches.

IV. NUMERICAL RESULTS

In our example the nonlinear B-H curve is simplified. It is linearized until the saturation point (2.03 T) [4] with μ_r=40000 (see Figure 6). This curve is applied in the magnetic branches 2, 3 and 4 (see Figure 5).

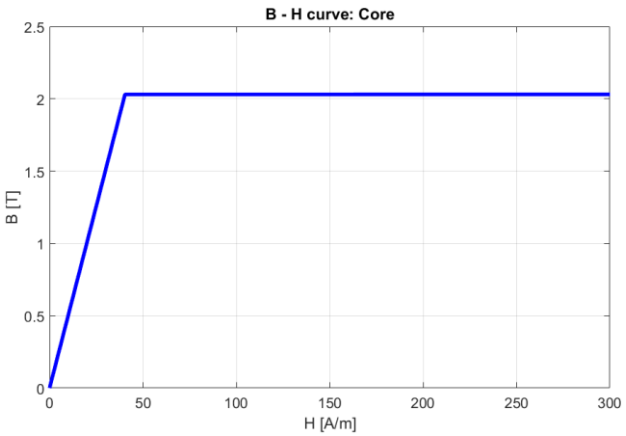

Figure 6: B-H curve for the magnetic branches according to the iron parts of the core

In yoke and return limb another B-H curve was used, due the flux has to go in hard direction of the anisotropic sheets. The saturation level of this material is estimated at

1.85T, and the relative permeability below this point is μ_r=10000 (see Figure 7).

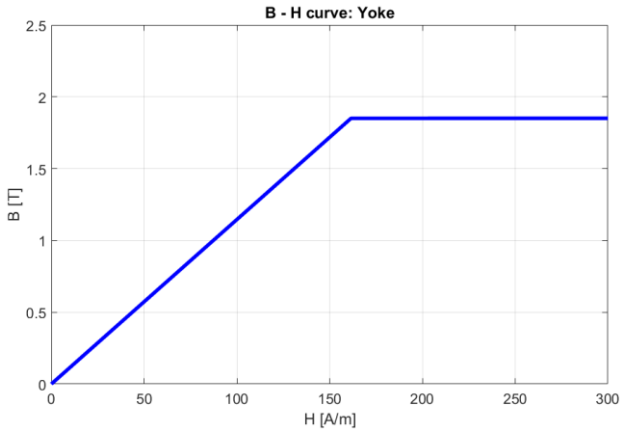

Figure 7: B-H curve for the magnetic branches according to yoke and return limb

The inrush current can be determined fast and accurate with this simplified model, due in that case there are only 105 unknowns to be determined in each timestep: 14 nodes in the magnetic circuit model (see Figure 5), 90 electric branches according to the winding parts (30 in each phase) and 1 eddy-current branch around the magnetic branch represents the tank wall. The inrush current in the first second calculated by this method is shown in Figure 8.

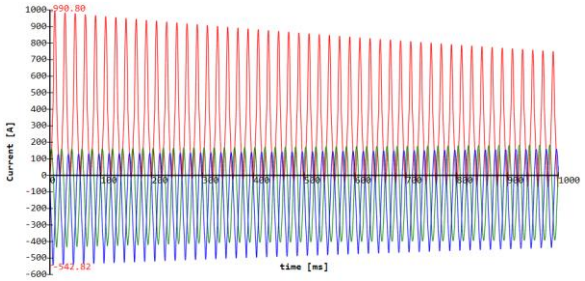

Figure 8: Inrush current in the main windings of a 3-phase reactor. Red: phase 1, Green: phase 2, Blue: phase 3

The inrush current calculation is not very sensitive to the B-H curve, due to the most parts of the iron is saturated at the beginning. In a second simulation the core B-H curve was replaced by a more realistic one (see Figure 9).

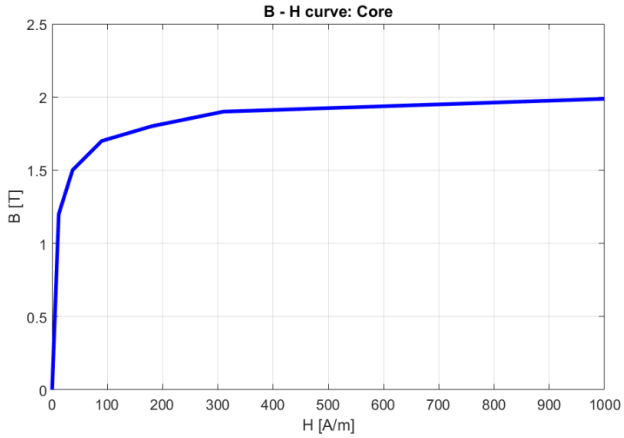

Figure 6: B-H curve for the magnetic branches according to the iron parts of the core

The difference between the two simulations is neglectable as shown in Table II.

TABLE II
COMPARISON OF THE PEAK CURRENTS USING DIFFERENT B-H CURVES FOR THE CORE MATERIAL IN THE MAGNETIC CIRCUIT SIMULATION

Phase description	Peak current with the linearized B-H curve	Peak current with the more accurate B-H curve
Phase 1	990,80 A	990,99 A
Phase 2	-435,29 A	-434,36 A
Phase 3	-542,82 A	-542,01 A

Also the shape of the inrush currents are in principle the same as it is shown in Figure 9 and 10.

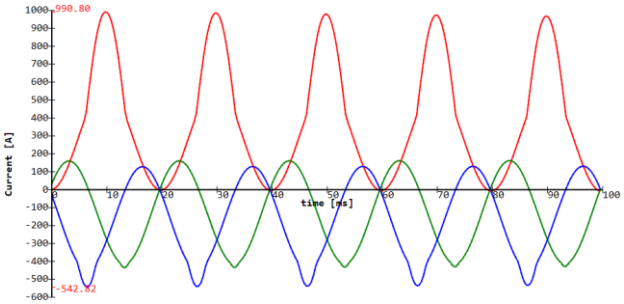

Figure 9: Inrush current in the main windings of a 3-phase reactor using the linearized B-H curve. Red: phase 1, Green: phase 2, Blue: phase 3

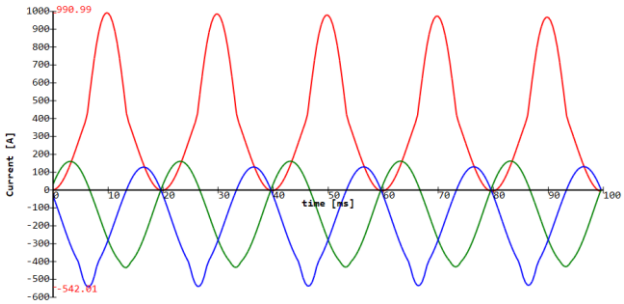

Figure 10: Inrush current in the main windings using the realistic B-H curve. Red: phase 1, Green: phase 2, Blue: phase 3

V. CONCLUSION

An efficient, stable and accurate approach was presented to determine the inrush current of gapped-core shunt reactors. An additional advantage of this method is that the differential equation must be determined only once, and it can be used for all tap positions for VSR-s.

REFERENCES

[1] A. Župan, B. Filipović-Grčić, and I. Uglešić, "Modelling of variable shunt reactor in transmission power system for simulation of switching transients," *2017 40th International Convention on Information and Communication Technology, Electronics and Microelectronics (MIPRO)*, Opatija, 2017, pp. 598-602.

[2] S. Kanerva, S. Seman, and A. Arkkio, "Inductance Model for Coupling Finite Element Analysis With Circuit Simulation," *IEEE Trans. Magn.*, vol. London, vol. 41, No. 5, pp. 1620-1623, May 2005.

[3] O. Biro, K. Preis, G. Buchgraber and I. Ticar, "Voltage-driven coils in finite-element formulations using a current vector and a magnetic scalar potential," *in IEEE Transactions on Magnetics*, vol. 40, no. 2, pp. 1286-1289, March 2004.

[4] Toshiro Tomida, Shigeo Uenoya and Naoyuki Sano, "Fine-Grained Doubly Oriented Silicon Steel Sheets and Mechanism of Cube Texture Development", *in JIM Materials Transactions*, vol. 44, No. 6 (2003) pp. 1106 to 1115

Anderson acceleration for electromagnetic nonlinear problems

[1]Mattia Filippini, [1]Piergiorgio Alotto, [2]Alessandro Giust

[1]Dipartimento di Ingegneria Industriale, Universit di Padova, Padova, Italy
[2]Doctoral Program Computational Mathematics, Johannes Kepler University, Linz, Austria

Purpose:
The purpose of this paper is to implement the Anderson acceleration for different formulations of eletromagnetic nonlinear problems and analyze the method efficiency and strategies to obtain a fast convergence.

Design/methodology/approach:
The paper is structured as follows: the general class of fixed point nonlinear problems is shown at first, highlighting the requirements for convergence. The acceleration method is then shown with the associated pseudo-code. Finally, the algorithm is tested on different formulations (finite element, finite element/boundary element) and material properties (nonlinear iron, hysteresis models for laminates). The results in terms of convergence and iterations required are compared to the non-accelerated case.

Findings:
The Anderson acceleration provides accelerations up to 75 per cent in the test cases that have been analyzed. For the hysteresis test case, a restart technique is proven to be helpful in analogy to the restarted GMRES technique.

Originality/value:
The acceleration that has been suggested in this paper is rarely adopted for the electromagnetic case (it is normally adopted in the electronic simulation case). The procedure is general and works with different magneto-quasi static formulations as shown in the paper. The obtained accelerations allow to reduce the number of iterations required up to 75 per cent in the benchmark cases. The method is also a good candidate in the hysteresis case, where normally the fixed point schemes are preferred to the Newton ones.

Keywords:
Numerical analysis

Published in COMPEL - The international journal for computation and mathematics in electrical and electronic engineering, Vol. 38 No. 5, 2019, ISSN 0332-1649, page 1493 - 1506

Parallel finite-element method using domain decomposition and Parareal for transient motor starting analysis

[1]Yasuhito Takahashi, Koji Fujiwara, [2]Takeshi Iwashita, [3]Hiroshi Nakashima

[1]Department of Electrical Engineering, Doshisha University, Kyotanabe, Japan
[2]Information Initiative Center, Hokkaido University, Sapporo, Japan
[3]Academic Center for Computing andMedia Studies, Kyoto University, Kyoto, Japan

Purpose:
This paper aims to propose a parallel-in-space-time finite-element method (FEM) for transient motor starting analyses. Although the domain decomposition method (DDM) is suitable for solving largescale problems and the parallel-in-time (PinT) integration method such as Parareal and time domain parallel FEM (TDPFEM) is effective for problems with a large number of time steps, their parallel performances get saturated as the number of processes increases. To overcome the difficulty, the hybrid approach in which both the DDM and PinT integration methods are used is investigated in a highly parallel computing environment.

Design/methodology/approach:
First, the parallel performances of the DDM, Parareal and TDPFEM were compared because the scalability of these methods in highly parallel computation has not been deeply discussed. Then, the combination of the DDM and Parareal was investigated as a parallel-in-space-time FEM. The effectiveness of the developed method was demonstrated in transient starting analyses of induction motors.

Findings:
The combination of Parareal with the DDM can improve the parallel performance in the case where the parallel performance of the DDM, TDPFEM or Parareal is saturated in highly parallel computation. In the case where the number of unknowns is large and the number of available processes is limited, the use of DDMis the most effective from the standpoint of computational cost.

Originality/value:
This paper newly develops the parallel-in-space-time FEM and demonstrates its effectiveness in nonlinear magnetoquasistatic field analyses of electric machines. This finding is significantly important because a new direction of parallel computing techniques and great potential for its further development are clarified.

Keywords:
Electrical machine, Transient analysis, Finite element method, Domain decomposition method, Parallel computing, Parareal

Published in COMPEL - The international journal for computation and mathematics in electrical and electronic engineering, Vol. 38 No. 5, 2019, ISSN 0332-1649, page 1507 - 1520

Statistical solution of inverse problems using a state reduction

Markus Neumayer, Thomas Suppan, Thomas Bretterklieber

Institute of Electrical Measurement and Measurement Signal Processing,Graz University of Technology, Graz, Austria

Purpose:
The application of statistical inversion theory provides a powerful approach for solving estimation problems including the ability for uncertainty quantification (UQ) by means of Markov chain Monte Carlo (MCMC) methods and Monte Carlo integration. This paper aims to analyze the application of a state reduction technique within different MCMC techniques to improve the computational efficiency and the tuning process of these algorithms.

Design/methodology/approach:
A reduced state representation is constructed from a general prior distribution. For sampling the Metropolis Hastings (MH) Algorithm and the Gibbs sampler are used. Efficient proposal generation techniques and techniques for conditional sampling are proposed and evaluated for an exemplary inverse problem.

Findings:
For the MH-algorithm, high acceptance rates can be obtained with a simple proposal kernel. For the Gibbs sampler, an efficient technique for conditional sampling was found. The state reduction scheme stabilizes the ill-posed inverse problem, allowing a solution without a dedicated prior distribution. The state reduction is suitable to represent general material distributions.

Originality/value:
The paper presents a method to improve the solution process of inverse problems within the Bayesian framework. The stabilization of the inverse problem due to the state reduction improves the solution. The approach simplifies the tuning of MCMC methods.

Keywords:
Inverse problems, Bayesian statistics, State reduction, Statistical solution

Published in COMPEL - The international journal for computation and mathematics in electrical and electronic engineering, Vol. 38 No. 5, 2019, ISSN 0332-1649, page 1521 - 1532

Algebraic Properties of Poynting-Theorem

Hannes Töpfer*, Jürgen Ulm† and Dimitri Delkov†
*TU Ilmenau Department of Advanced Electromagnetics, Helmholzplatz 2, 98693 Ilmenau, Germany
†Heilbronn University of Applied Sciences Campus Künzelsau, Daimlerstraße 35, 74653 Künzelsau
E-mail: dimitri.delkov@hs-heilbronn.de

***Abstract*—The aim of this paper is to show the algebraic properties of the Poynting-Theorem from algebraic topology viewpoint in order to show the behavior of the energy flow in electromagnetic fields on manifolds in different dimensions.**

***Index Terms*—electromagnetic energy, Poynting-Theorem.**

I. INTRODUCTION

To optimize the efficiency of electromagnetic devices it is useful to know the electromagnetic energy flow inside and outside of the considered system. The electromagnetic energy can be determined by calculating the Poynting vector. However, the calculation of the Poynting vector can be very complicated when the considered system has a complex geometry. In this case, the field quantities will be calculated with the finite-element-method. Due to discontinuities on the surfaces where different media cut each other, the Poynting vector is also discontinuous; this property will be analyzed in this paper more accurately. In this paper, we want to show how energy flow in electromagnetic fields can be described from geometrical topology viewpoint. At first, we introduce simplicial surfaces and simplicial complexes in $\mathbb{R}^n$ to describe the room and the electromagnetic energy flow. In order the algebraic structure and behavior will considered and analyzed.

II. ENERGY FLOW IN ELECTROMAGNETIC FIELDS

In the past, there was a discussion of the unique solution of the Poynting vector. Because when we add, a divergence free vector field to the Poynting-Theorem the solution of the power flux will be not change

$$\nabla(\boldsymbol{E}\times\boldsymbol{H}) = \nabla(\boldsymbol{E}\times\boldsymbol{H} + \nabla\times\boldsymbol{v}). \tag{1}$$

Where $\boldsymbol{H}$ is the magnetic field strength, $\boldsymbol{E}$ the electric field strength and $\boldsymbol{v}$ an arbitrary vector field. This problem occurs in many publications and many solutions were proposed. We can read one solution of this problem in [1]. The Poynting-Theorem is also a law of energy conservation (without dissipation)

$$\frac{\partial u}{\partial t} = -\nabla\boldsymbol{S}. \tag{2}$$

Where $\boldsymbol{S}$ is the Poynting vector and u the electromagnetic energy. This law can be considered as analogy to the conservation of charges. We will consider at first the Poynting-Theorem in the integral form

$$\oiint_S \boldsymbol{E}\times\boldsymbol{H}\,d\boldsymbol{S} = \iiint_V \boldsymbol{H}\frac{\partial\boldsymbol{B}}{\partial t}dV + \iiint_V \boldsymbol{E}\frac{\partial\boldsymbol{D}}{\partial t} + \iiint_V \boldsymbol{E}\boldsymbol{J}\,dV. \tag{3}$$

The left side of the equation (3) means; the energy flowing through the boundary surfaces of the volume is equal to the negative of the total energy per unit volume. This includes the time rate of change of electromagnetic energy plus time rate of change of electric energy plus the energy losses.

To obtain the entire energy located in a system, we have to solve the integral over a closed surface. Before we solve the integral, we have to look of the properties of the surface.

III. TOPOLOGY

There is, actually, different definition of a surface, depending upon which type of properties one is interested. There are three main types of surfaces:

- Topological surfaces
- Simplical surfaces and
- Smooth Surfaces

Every surface of one of the three types can be converted into either of the other types. This does not hold in higher dimensions!

A. Topological Surfaces

Definition: A subset $Q \subset \mathbb{R}^n$ is called a topological surface, or just surface, if each point $p \in Q$ has an open neighborhood that is homeomorhic to the open unit dist int D^2.

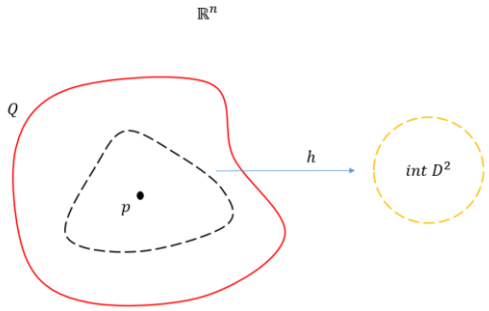

Figure 1: Topological Surface

B. Simplical Surfaces

Definition: Let $\sigma = < a_0, \dots, a_k >$ be a k-simplex in $\mathbb{R}^n$. A face of σ is a simplex spanned by a non-empty subset of $\{a_0, \dots, a_i\}$; if this subset is proper the face is called a proper face. A face of σ that is a k-simplex is called a k-face.

C. Smooth Surfaces

Definition: A subset $M \subset \mathbb{R}^n$ is a smooth surface if it is a topological surface and if for each point $p \in M$ there is a coordinate patch $\varphi: U \to M \subset \mathbb{R}^3$ such that $p \in \varphi(U)$.

D. Orientation on Surfaces

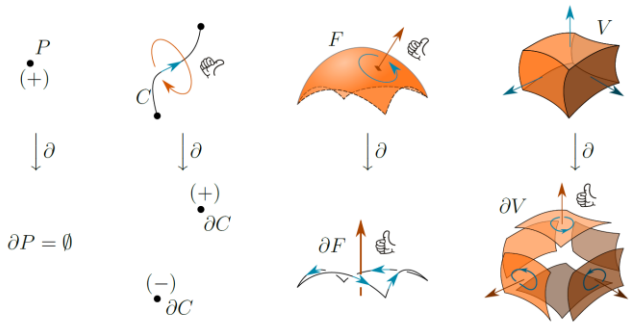

Figure 2: Orientation of surfaces

In the above figure we can see, 0-, 1-, 2-, and 3-dimensional manifolds with inner (blue) and outer (orange) orientation.

In the bottom figure, we can see boundaries of the manifolds with induced orientation. Null-dimensional manifolds (points) have a sign as orientation and have no edge. The three-dimensional manifold has only an inner but not an outer orientation. Inner and outer orientation form a coordinate system.

IV. Poincarè-Lemma

We consider a closed curve. Then it is easy to find a surface whose edge is exactly this curve. In addition, it is easy to see that there are several (infinitely many) surfaces that have the same edge curve. For a curve C and a surface$F$, we can say

1. The curved is closed: $\partial C = 0$.
2. The edge of a surface is a curve: $\partial F = C$.
3.

It becomes more difficult when the surface is connected several times, that is; it have holes. Then the surface has several borders and is ambiguous.

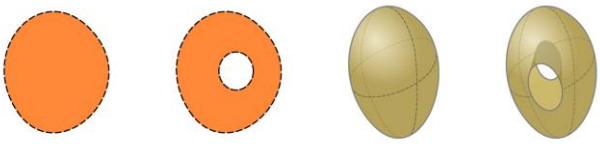

Figure 3: Surfaces and volumes

So we can conclude. A differential form is closed when

$$d\omega = 0.$$

It is called exactly if it is a differential form (also called potential form), so that

$$\omega = dn.$$

Due to the complex property, $dd = 0$ every exact differential form is closed. However, the reverse applies only under a (topological) condition: The area must be simply connected (precise: star-shaped, but this is the same in the cases relevant to electrodynamics).

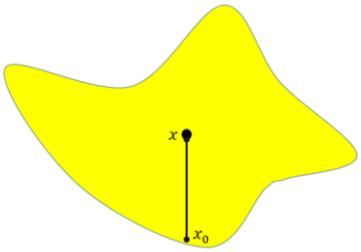

Figure 4: star-shaped region

A subset $M \subseteq \mathbb{R}^n$ is said to be *star-shaped* with respect to the point $x_0 \in M$ if the line segment

$$[x_0\ x] = \{x_0 + t(x - x_0): t \in [0,1]\}$$

is connected in M for all $x \in M$.

If an area has holes, we cannot find a potential form to determine the differential form. For any star-shaped regions, we can say that there exist always potentials

- potentials are uniquely determined except for constants
- vector potentials are uniquely determined except for one gradient field.

V. De Rham –Cohomology

For example, consider a two-dimensional manifold (a surface) with non-trivial topology, meaning the surface has a hole. The hole leads to a nontrivial cohomology:

"hole" $\to Kern(curl) \neq Image(grad) \to \boldsymbol{v} \neq grad\varphi.$

Consequently, a vector field $\boldsymbol{v}$ cannot be expressed as a gradient of a scalar potential. We can calculate the quotient spaces

$$H^1(X, \mathbb{R}) := \frac{Kern\left(curl: V(X) \to V(X)\right)}{Image\left(div: F(X) \to V(X)\right)}$$

$$H^2(X, \mathbb{R}) := \frac{Kern\left(div: V(X) \to F(X)\right)}{Image\left(rot: F(X) \to V(X)\right)}.$$

It is remarkable that the quotient space $H^1(X, \mathbb{R})$ is usually finite-dimensional, although both $Kern\,(curl)$ and $Image\,(grad)$ are infinite-dimensional.
For $H^1(X, \mathbb{R}) = 0$ whenever $X \subseteq R^2$ is star-shaped.
The dimension of $H^1(X, \mathbb{R})$ is the number of „holes" of X.

In principle, de Rham cohomology is not needed to reach this conclusion; we can also obtain this from the Poincarè-Lemma. Their relevance (for numerical field computation) lies in the fact that topological properties can be calculated numerically exactly and with little effort. This is done by simplicial approximation of the area that means triangulation in polygon (1D), triangles (2D) and

tetrahedrons (3D), as it is anyway for the FEM is necessary.

We can illustrate the de Rham complex in the following figure.

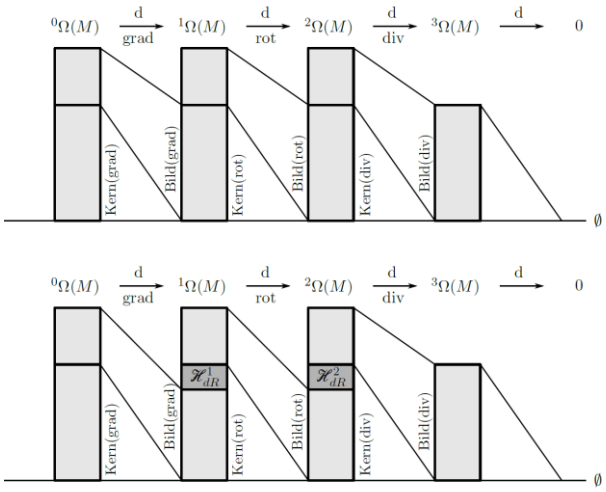

Figure 5: The de Rham complex [6]

In figure (5) we can see the de Rham complex in three-dimensional space with kern and image of the differential operators. Above: de Rham complex for simply connected areas. Bottom: For multiple connected areas, nontrivial de Rham cohomologies arise.

In the electromagnetic field theory, there are several cases where nontrivial topology arises. For instance, we consider the following figure.

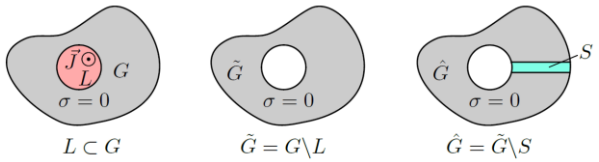

Figure 6: Different topologies [6]

Left: G is a simply connected, but not rotation-free area. Middle: G is a rotation-free, but not simply connected area. Right: Through a cut the area G is simply connected.

For a vortex field, therefore, a scalar function would be necessary, monotonically increasing on a closed path so that every field line of the vortex field is closed. But this is not possible. One possible solution is a cut S: The (rotation-free) area $\tilde{G}$ was cut, now the two conditions are satisfied

1. $curl\ \boldsymbol{H} = 0 \rightarrow d^1H = 0$
2. The area $\hat{G}$ is simple connected.

And we can expressed the magnetic field strength as usual

$$\boldsymbol{H} = -grad\ \psi. \tag{4}$$

VI. Computation of Poynting Vector

To calculate the energy in electromagnetic field, we have to consider the topology (and geometry), the Poincarè-Lemma and the cohomology. There are two different ways to solve the Poynting-Theorem. The classical way is to solve the Poynting vector directly with the field quantities

$$\boldsymbol{E} = -grad\ \varphi - \partial_t \boldsymbol{A} \tag{5}$$

$$\boldsymbol{H} = \frac{1}{\mu} curl\ \boldsymbol{A}. \tag{6}$$

The two field strengths are discrete 1-forms

$$\boldsymbol{S} \coloneqq \boldsymbol{E} \times \boldsymbol{H} = * (\mathfrak{E}^1 \wedge \mathcal{H}^1). \tag{7}$$

Where * is the Hodge-Star operator and $\mathfrak{E}^1$, $\mathcal{H}^1$ one forms. Thus, the Poynting vector must be a 2-form. This calculation method have one disadvantage. Since the magnetic field strength $\boldsymbol{H}$ is a weak solution, it does not satisfy the tangential continuity of a 1-form. Continuity can not be guaranteed and the power flow is not exactly preserved. Since $\boldsymbol{E}$ and $\boldsymbol{H}$ can not be approximated conformity at the same time, the Poynting vector $\boldsymbol{S}$ as their cross product is not compliant. This is a big disadvantage, because the energy transfer can only calculated on boundaries.

The second method based on *Whitney-Elements*. Here we use node, edge, face and volume elements as approach functions and apply the finite-element-method.

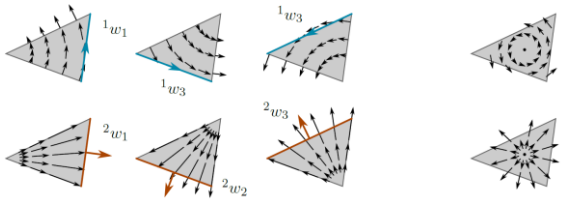

Figure 7: Whitney-Elements

Edge elements form a vortex field, facet elements form a source field. Degree of freedom is the circulation along one edge or the flow through one. Whitney k forms have three deifying properties

- they are polynomials of at least the first degree
- the magnitude and the orientation on the common sides surface of two adjacent tetrahedral of the discrete $k-forms$ are the same
- they are uniquely determined by a k-dimensional integral on a k-simplex.

When the suitable Whitney elements are chosen, their continuity conditions are identical to those of the approximated field quantities. Field strengths are tangentially continuous and normally discontinuously, a property that is approximated appropriately with edge elements. At flux densities, the normal component is continuous and the tangent component is discontinuous, which is reflected correctly by facet elements.

These properties are very suitable to calculate the Poynting vector and the electromagnetic energy inside of a system.

With the field quantities we calculate at first the energy (electric and magnetic energy).

$$u_e^3 = \frac{1}{2}\mathfrak{E}^1 \wedge D^2 \tag{8}$$

$$u_m^3 = \frac{1}{2}\mathcal{H} \wedge \mathcal{B} \tag{9}$$

Subsequently the Poynting vector can be determined.

VII. Conclusion

When we want to calculate the electromagnetic energy or the Poynting-Theorem (Poynting vector), we cannot do that by using the standard methods. We have to consider the cohomology, also the topology and geometry of the given system to calculate the field quantities. Furthermore, there is one open question about Poynting vector. We still do not know whether the Poynting vector exist in non-trivial topologies or not. This problem we will investigate in further works.

To simulate the electromagnetic energy flow it is suitable to use the Whitney elements to calculate the field quantities in order to calculate the Poynting vector. This require further works and programming to show it on a real system.

References

[1] A. Bossavit "A note on the Poynting vector and of the Maxwell tensor" EMF 2016 Symposium, Int J Number Model. 2018; 31:e2214.

[2] A. Bossavit, "Computational Electromagnetism, Variational Formulations, Complementarity, Edge Elements", 1997, Academic Press.

[3] D. Bloch, "A first Course in geometric Topology and Differential Geometry", 1956, Birkhäuser.

[4] K. Jänich, "Topologie", 2004, Springer-Lehrbuch.

[5] K. Jänich, "Vektoranalysis", 2004, Springer-Lehrbuch.

[6] C. Kißling, "Implementierung des Poynting-Theorems in die Finite-Elemente-Methode", 2018, Master-Thesis, TU Ilmenau

Modeling of the Reversible Heat Source in Lithium-Ion Batteries and its Impact on a Multi-Physics Model

N. Köster*, C. Essl*, F. Pichler*, A. Thaler*, J. Fabian†, P. Parz† and F. Prosznigg†

*VIRTUAL VEHICLE Research Center,
†Samsung SDI Battery Systems
E-mail: niels.koester@v2c2.at

***Abstract*—The reversible heat source in a lithium-ion battery is modeled and implemented in a multi-physics model, which aims to simulate the thermal, electrical and chemical behavior of the battery cell. The numerical solution is compared to real measurements of this cell to show the impact of the reversible heat source on the thermal behavior.**

***Index Terms*—battery modeling, finite element method, multi-physics, thermal behavior.**

I. Introduction

Battery-electrical vehicles become more competitive and their driving range becomes larger. This is achieved with an increase in volume and energy density of the battery cells and battery modules. This has the side effect that the batteries can generate more heat. Therefore, the thermal management is an increasingly important factor in battery design. Additionally, heat sources, which traditionally are ignored because their impact is to small, have to be considered as well.

For the thermal design of the battery the heat must be accurately modeled. There are two main heat sources, which are the focus in this paper:

- The irreversible/Joule's heat source $\mathrm{q_J}$, which is the heat generated by the Joule's losses and the losses due to over-potential
- The reversible/reaction heat source $\mathrm{q_R}$, which is the heat generated or consumed by the lithium reactions in active materials.

The Joule's heat source $\mathrm{q_J}$ is well understood. But the reversible heat source $\mathrm{q_R}$ is often not modeled at all, because its calculation is not trivial. For example *Pals et al.* [1] states the problem of not having enough OCV measurements to calculate $\mathrm{q_R}$ and therefore set it zero.

The reversible heat source $\mathrm{q_R} = IT\frac{\partial U_{ocv}}{\partial T}$ is connected to the reaction entropy $\Delta S = nF\frac{\partial U_{ocv}}{\partial T}$. This connection is generally used to calculate $b(z) = \frac{\partial U_{ocv}}{\partial T}$, see *Giel et al.* [6], because the direct calculation of the derivative $\frac{\partial U_{ocv}}{\partial T}$ is in many cases not possible.

If $b(z)$ is calculated, this is often done for coin cells [6] or half cells [8] [9]. *Reynier et al.* [9] determined the entropy of lithiation of Li_xCoO_2 for $0.5 < x \leq 1$ and *Williford et al.* [8] calculated the entropy of lithiation of graphite. This is than superimposed to get the $\mathrm{q_R}$, see *Jeon et al.* [3].

This paper introduces a simpler method to calculate $b(z)$ which is based directly on the energy balance (3) by *Bernardi et al.* [2].

In Section II the point and 3d multi-physics model are introduced and discussed.

In Section III the measurements and method to determine $b(z) = \frac{\partial U_{ocv}}{\partial T}$ are discussed. The method, which we call the **energy based method**, is applied to a prismatic commercial battery cell used in automotive applications.

In Section IV the resulting $b(z)$ is used in a multi-physics simulations and compared with a measured temperature on the surface of the commercial battery cell. The simulations in Section IV suggest that the **energy based method** gives a good approximation of the reversible heat source $\mathrm{q_R}$. Additionally, the **energy based method** can be applied to prismatic battery cells directly and not only to half or coin cells. For example to the commercial battery cell examined in this paper has the outer dimensions $150mm \times 95mm \times 25mm$.

This research is part of the flagship project "eMPROVE" which is funded in Austria by the "Climate and Energy Fund" and the Austrian Federal Ministry for Transport, Innovation and Technology (bmvit).

II. Multi-Physics Battery Models

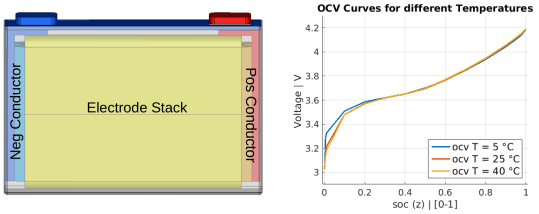

(a) Generic Cell Geometry (b) U_{ocv} for different temperatures

Fig. 1: *1a: Model of one battery cell with different parts: electrode stack, aluminum positive conductor and copper negative conductor. This is just a schematic drawing, not a real cell. 1b: Measured U_{ocv}-curve for temperature $5°C$, $25°C$ and $40°C$ from a commercial battery cell.*

A. Point Model

The multi-physics model discussed in this paper has three distinct sets of equations which describe the battery cell.

The State of Charge z: The **state of charge** (soc) is defined as 1.0 when the cell is fully charged and 0 if the cell is fully discharged. It is modeled by the Coulomb counting method:

$$\frac{dz}{dt}(t) = \frac{1}{Q_p} I(t), \tag{1}$$

where Q_P is the cell capacity in As and I is the current in A [5, Section 2.2]. The equation (1) states that z dependent on $|I|/Q_p$. Therefore, in battery modeling the current is often given in C, where $1C$ is the current needed to discharge the cell in 1h. The commercial battery cell used in this paper has a capacity $Q_p = 37Ah$, where $1C$ is the current $37A$ and $0.5C$ is $18.5A$.

The Cell Voltage U: The **voltage** U is modeled as

$$U(t) = U_{ocv}(t) + f_U(t) \tag{2}$$

which generally is split into a **open circuit voltage** U_{ocv} (OCV) and an **overpotential** f_U [5, Section 2.1 - 2.8]. The open circuit voltage depends on the state of charge z, the temperature T:

$$U_{ocv}(t) = U_{ocv}(z(t), T(t)).$$

There are different methods to model f_U for now it is assumed that the open circuit voltage is given, then the overpotential is $f_U = U - U_{ocv}$.

The Temperature T of the cell: The **temperature** in K is calculated with the energy balance [2], which in its simplified form is

$$c_p \frac{dT}{dt}(t) + h_s \left(T(t) - T_s\right) = \mathrm{q_J}(t) + \mathrm{q_R}(t), \tag{3}$$

where c_p is the heat capacity, h_s is the heat transfer coefficient, T_s is the external Temperature. The **reversible heat source** is

$$\mathrm{q_R}(t) := I(t) T(t) \frac{\partial U_{ocv}}{\partial T}(t) \tag{4}$$

and the **Joule's heat source** is

$$\mathrm{q_J}(t) := I(t) \left(U(t) - U_{ocv}\right). \tag{5}$$

The main focus of this work is the **reversible heat source**, its measurements and calculation, since it is the heat generated by the lithium reaction with the cathode and anode it can also be called the **reaction heat source**. To calculate the reversible heat source with (4) is often not practical, since the calculation of the entropy $b(z)$ is not easy, see Example 1, where the entropy is defined as

$$b(z) := \frac{\partial U_{ocv}}{\partial T}(t).$$

The **Joule's heat source** in general is composed of the Joule heating and the dissipated power of the overpotential. For the point model the Joule's heat source is only dependent on the overpotential f_U, i.e $\mathrm{q_J}(t) = I f_U \geq 0$. Because it is always positive independent of the current, it is often called the irreversible heat source.

Example 1. In a commercial battery cell measured at the VIRTUAL VEHICLE Research Center we recorded that differences of $10^{-4}V$ in the measurement of the open circuit voltage already resulted in huge differences ($> 200\%$) of $\frac{\partial U_{ocv}}{\partial T}$ since many OCV-curves of commercial cells show little variation over a large temperature range. See Figure 1b for an example U_{ocv}-curve for the prismatic commercial battery cell with the dimensions $150mm \times 95mm \times 25mm$.

As Example 1 shows a direct calculation of $\mathrm{q_R}$ with the open circuit voltage U_{ocv} is often not practical.

B. 3d Model

The domain of the battery is $\Omega \in \mathbb{R}^3$, where every $x \in \Omega$ is a point in a battery with possible different material parameters. The domain Ω is bounded and has a polygonal boundary. In the 3d multi-physics model there are three distinct domains which together make up the whole battery

$$\Omega = \overline{\Omega_J} \cup \overline{\Omega_T} \cup \overline{\Omega_A},$$

each of this domains has different physical equations and consist of different materials. The domains are:

1) Electrode Stack ($\Omega_J \subset \mathbb{R}^3$)
   - chemical-electrical equation,
   - thermal equation,
   - one non-isotropic homogenized material.
2) Conductors ($\Omega_T \subset \mathbb{R}^3$)
   - electrical equation,
   - thermal equation,
   - different material (Copper, Aluminum, ...).
3) Non-conductive Materials ($\Omega_A \subset \mathbb{R}^3$)
   - thermal equation,
   - different material (Air, Plastic, ...).

For an example of the different domains see Figure 1a, where the electrode stack is shown in yellow, the conductors are red and blue and the non-conductive materials are transparent.

The **electrical model** and the **electrical-chemical model** are described in *Pichler et al* [4]. The electrical model is simplified by the implicit super-position strategy [4, Equation (22) - (25)]. The electrical-chemical model in the electrode stack is strongly coupled with the electrical model, see [4, Equation (30) - (34)]. The **thermal model** in this paper has different heat sources than *Pichler et al* [4] and is

$$\begin{aligned} c_p^H(x) \frac{\partial}{\partial t} T(t,x) - \nabla \left(\lambda^H(x) \cdot \nabla T(t,x)\right) & \\ = q(t,x) & \quad \text{for } x \in \Omega \\ \gamma_1^{\mathrm{int}} T(t,x) = h_s \left(T(t,x) - T_s\right) & \quad \text{for } x \in \Gamma_{cool} \\ \gamma_1^{\mathrm{int}} T(t,x) = 0 & \quad \text{for } x \in \Gamma \setminus \overline{\Gamma_{cool}} \\ T(0,x) = T_0(x) & \quad \text{for } x \in \overline{\Omega}, \end{aligned} \tag{6}$$

with the heat capacity $c_p^H(x)$ and the heat conductivity $\lambda^H(x)$ depending on the material at the point x. The boundary $\Gamma := \partial\Omega$ of the battery cell is split into a part that is actively cooled Γ_{cool} and the rest which is assumed to be isolated. The co-normal derivative $\gamma_1^{\mathrm{int}} T(t,x)$ of the T is defined as

$$\gamma_1^{\mathrm{int}} T(t,x) := \lim_{\Omega \ni \tilde{x} \to x \in \Gamma} \left(\lambda^H(\tilde{x}) \cdot \nabla T(t,\tilde{x})\right) \cdot \boldsymbol{n}(x),$$

where $\boldsymbol{n}$ is the outer normal vector of Ω.

The heat source q is split into the **irreversible heat source** $\mathrm{q_J}$, the **reversible heat source** $\mathrm{q_R}$ and the Joule's heat source on q_j, as discussed below. The **reversible heat source** is:

$$\mathrm{q_R} := A\, i(t,x)\, T(t,x)\, b(z(t,x)), \quad \text{for } x \in \Omega_J$$

where i is the current density at point $x \in \Omega_J$ in $\frac{A}{m^2}$, z is state of charge at point $x \in \Omega_j$, A is the cathode/anode area per volume in $\frac{m^2}{m^3}$ and b is the approximation of $\frac{dU_{ocv}}{dT}$ in $\frac{V}{K}$. The **irreversible heat source** is:

$$\mathrm{q_J}(t,x) := A\, i(t,x)\, (U(t,x) - U_{ocv}(z,T))\,,$$

for $x \in \Omega_J$, where $U(t,x) = \varphi_+(t,x) - \varphi_-(t,x)$ in V is the voltage between cathode and anode and U_{ocv} is the open circuit voltage in V. The **cathode potential** $\varphi_+(t,x)$ and the **anode potential** $\varphi_-(t,x)$ are the solution of the electrical-chemical model [4, Equation (30) - (34)].

In the homogenized 3d model the heat source q consists of the two contributions already discussed in (4) and (5) and one further Joule's heating term that emerges from the current flowing through the aluminum foil and copper foil in the electrode stack

$$\begin{aligned} q_j^1(t,x) := \quad & (\sigma_+ \nabla\varphi_+(t,x)) \cdot \nabla\varphi_+(t,x) \\ + \quad & (\sigma_- \nabla\varphi_-(t,x)) \cdot \nabla\varphi_-(t,x) \end{aligned} \tag{7}$$

for $x \in \Omega_J$, where σ_+ is the electric conductivity of the cathode foil material (aluminum) and σ_- is the electric conductivity of the anode foil material (copper). In the point model (7) is already part of (5). In the conductors there also is a Joule's heat source:

$$q_j^2(t,x) := \quad (\sigma(x) \nabla\phi(t,x)) \cdot \nabla\phi(t,x) \quad \text{for } x \in \Omega_T,$$

where σ is the electric conductivity of the conductor and ϕ is the electrical potential in the conductor. Therefore, the heat source q is

$$q(t,x) = \begin{cases} q_j^1(t,x) + \mathrm{q_J}(t,x) + \mathrm{q_R}(t,x) & \text{for } x \in \Omega_J, \\ q_j^2(t,x) & \text{for } x \in \Omega_T, \\ 0 & \text{for } x \in \Omega_A. \end{cases}$$

The electrical-chemical, thermal and electrical models in $\Omega = \overline{\Omega_J} \cup \overline{\Omega_T} \cup \overline{\Omega_A}$ are discretized using a finite element method [7]. The resulting linear equations are solved using BiCGStab(l) with polynomial order 2 or the CG method depending on the equation. For the finite element discretization the open source software Elmer is used, see *www.csc.fi/web/elmer*.

III. Fitting Heat Source from Measurements

In this section a non-destructive approach based on the energy balance (3) is introduced and applied to a prismatic commercial battery cell. In contrast to the method which relies on the reaction entropy $\Delta S = nF \frac{\partial U_{ocv}}{\partial T}$ [6]. The method introduced in this section is called the energy based method, which does not need any knowledge about the anode and cathode material.

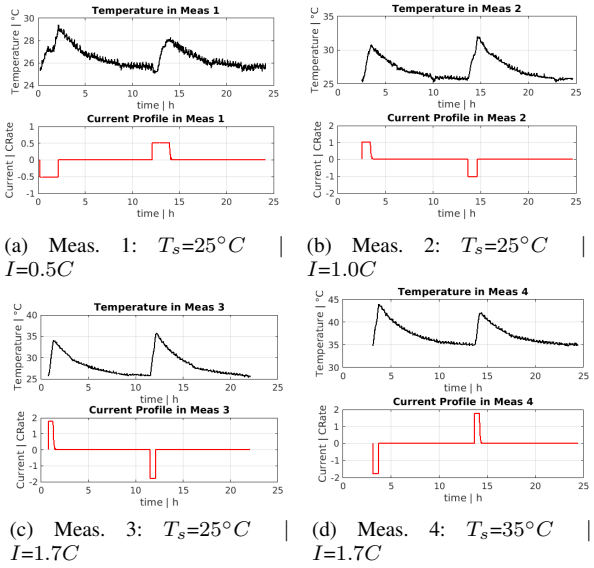

(a) Meas. 1: T_s=25°C | I=0.5C (b) Meas. 2: T_s=25°C | I=1.0C

(c) Meas. 3: T_s=25°C | I=1.7C (d) Meas. 4: T_s=35°C | I=1.7C

Fig. 2: *Temperature measurement for charge/discharge cycle, with different currents (0.5C, 1C and 1.7C) and different external temperatures (25°C and 35°C).*

In Section IV it is shown that this approach already produces a lot more accurate multi-physics 3d simulations.

The idea is to calculate the heat source with the energy equation (3) by

$$q(t) = \mathrm{q_J}(t) + \mathrm{q_R} = c_p^H \frac{dT^m(t)}{dt} + h_s\,(T^m(t) - T_s) \tag{8}$$

from a measured temperature $T^m(t)$. From this the heat source q is calculated and separated into $\mathrm{q_R}$ and $\mathrm{q_J}$. In the following subsection the measurement for the calculation of q, an approach to split q and a fitting process for $b(z)$ and $R(z)$ are discussed. Additionally, the model assumptions are inspected.

A. Measurement for the calculation of q

TABLE I: Overview of Meas. 1, 2, 3 and 4

Name Units	T_s °C	I C	T_{max}^{-I} °C	T_{max}^{+I} °C	a_1 V/A	a_2 V
Meas. 1	25	0.5	28.8	27.7	$0.11e-4$	-0.016
Meas. 2	25	1.0	31.5	30.3	$0.029e-4$	-0.016
Meas. 3	25	1.7	34.7	33.1	$0.011e-4$	-0.022
Meas. 4	35	1.7	44.1	42.2	$0.013e-4$	-0.028

The commercial battery cell is placed into a climate chamber (Memmert IPP 500) and the external temperature T_s is kept constant. The cell is cooled to the external temperature T_s. Then four different current profiles are applied: The cell is fully charged and discharged were the temperature at the beginning of each charge/discharge step is cooled to T_s.

0.) Temperate the cell to the external temperature T_s,
1.) Fully discharge/charge the cell with constant current I,
2.) Relaxation of the cell ($I = 0$) until $T(t) = T_s$,
3.) Fully charge/discharge the cell with constant current $-I$,

4.) Relaxation of the cell ($I = 0$) until $T(t) = T_s$.

These measurement are done for different constant currents I and different external temperatures T_s, four of these measurements are shown in Figure 2a - 2d and an overview of the different currents, external temperatures and some results are given in Table I.

If $I > 0$ the cell is charged, if $I < 0$ the cell is discharged and if $I = 0$ the cell relaxes.

To calculate the heat source q in the equation (8) the heat capacity c_p^H, the heat transfer coefficient h_s and the derivative $\frac{dT^m}{dt}$ have to be known.

The measurements Meas. 1, 2, 3 and 4 are used to calculate $b(z)$. Additionally, the measurements Meas. 3 and 4 are used to validate the linearity of $\mathrm{q_R}$ in T.

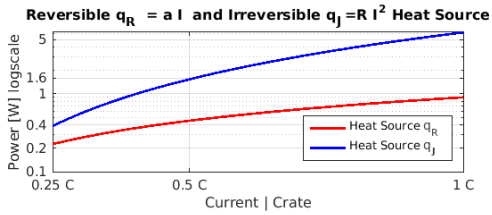

Fig. 3: *Fitted Heat Sources* $\mathrm{q_J} = aI$ *and* $\mathrm{q_R} = RI^2$*, where* R *and* a *are constant in* z *and* T*. The Fitting only uses the maximal Temperatures.*

Example 2 (Fit Constants). The first approximation we consider is $\mathrm{q_J} \approx a_1 I^2$ and $\mathrm{q_R} \approx a_2 I$, i.e $\mathrm{q_J}$ is quadratic and $\mathrm{q_R}$ is linear in the current. The temperature dependency is ignored for now. We can calculate a_1 and a_2 directly from T_{max}^{-I} and T_{max}^{+I}. The results from this calculation are given in Table I.

We see that for a discharge the lithium reaction is exothermic and heat is generated by $\mathrm{q_R}$. Furthermore, for a charge the reversible is endothermic and heat is used up. This is seen later again.

In Figure 3 the average Joule's heat source $\mathrm{q_J}(I) = a_1 I^2$ and the average reversible heat source $\mathrm{q_R}(I) = a_2 I$ are plotted. From this figure it can be concluded that the reversible heat source makes a big difference if the current is small ($|I| < 0.5C$). For this commercial battery cell $\mathrm{q_R}$ does not make a big difference for large current ($|I| > 1$).

If the cell is fully charged and discharged the difference $\Delta T = T_{max}^{-I} - T_{max}^{+I}$ stays the same if T_s does. This is the case for different I since $\mathrm{q_R}$ is linear in I.

B. Fitting of $\mathrm{q_R}$ and $\mathrm{q_J}$

1) Smooth Temperature T: The measured temperature T^m is smoothed by interpolating with a polynomial of order 5, which works very well for Meas. 1, 2, 3 and 4. For Meas 1 this is shown in Figure 4 for the charge and discharge cycle.

2) Calculate the Total Heat Source q: The heat source $q = \mathrm{q_J} + \mathrm{q_R}$ is calculated by equation (8) from $\frac{dT^m}{dt}$ and T^m. In Figure 4c the heat source for the discharge $q(-I)$ is shown in red and the heat source for the charge $q(I)$ is shown blue. The state of charge is calculated by (1),

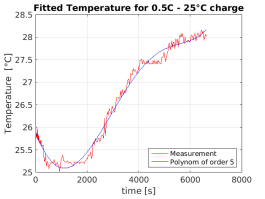

(a) T for charge cylce in Meas. 1: T_s=25°C | I=0.5C

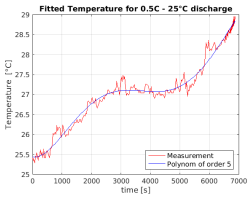

(b) T for discharge cycle in Meas. 1: T_s=25°C | I=0.5C

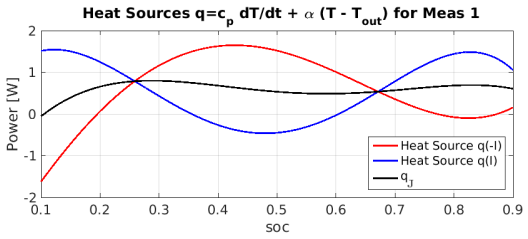

(c) heat source $q = \mathrm{q_R} + \mathrm{q_J}$ over the soc

Fig. 4: *Measured and fitted temperature curves charge and discharge and heat sources* $q = \mathrm{q_R} + \mathrm{q_J} = c_p \frac{dT}{dt} + h_s (T - T_s)$ *for the Meas. 1:* $1C$ *current and external temperature* $25°C$.

since the cell is fully charged at the beginning of Meas 1, i.e $z(0) = 1$.

3) Split the Total Heat Source q: To split the total heat source q up, **we assume that the Joule's heat source $\mathrm{q_J}$ is the same for charge and discharge**. Therefore, the heat sources are

$$\mathrm{q_J}(-I) = \mathrm{q_J}(+I) = 0.5\,(q(-I) + q(I))\,,$$
$$\mathrm{q_R}(-I) = -\,\mathrm{q_R}(+I) = 0.5\,(q(-I) - q(I)) = -ITb(z)$$

4) Calculate entropy $b(z) = \frac{\partial U_{ocv}}{\partial T}$: Then the entropy $b(z)$ is calculated using equation (4)

$$b(z) = \frac{\mathrm{q_R}(I, z(t))}{T(t)I} = \frac{\mathrm{q_R}(-I, z(t))}{T(t)(-I)}.$$

The resulting entropy $b(z)$ is shown in Figure 5 (top). And if we calculate R by $\mathrm{q_J} = RI^2$ we get the results in Figure 5 (bot). From Figure 5 (top) we can make the

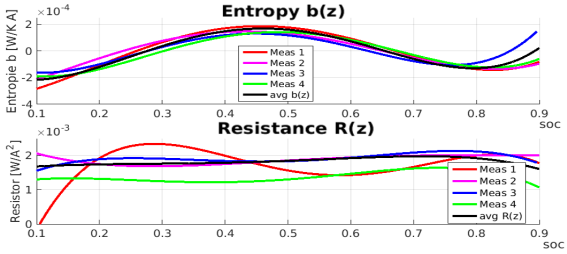

Fig. 5: *Calculated entropy $b(z)$ of the reversible heat source* $\mathrm{q_R} = ITb(z)$ *and calculated resistance R of the Joule's heat source* $\mathrm{q_J} = RI^2$ *by the symmetric approach.*

following deductions for this commercial battery cell:

- U_{ocv} varies so little in T that $b(z) = \frac{\partial U_{ocv}}{\partial T}$ does not depend on T.
- $b(z)$ does not depend on the current I. Neither on the size $|I|$, nor on the direction of I.
- The lithium reaction is on average endothermic for

a charge and exothermic for a discharge, because $\int_0^1 b(z)\,dz < 0$.

- $b(z)$ varies strongly in the state of charge z. And $b(z)$ has a local maximum at $z \approx 0.45$. And two local minima at $z \approx 0.1$ and $z \approx 0.8$. For Meas. 1 the extrema of $\mathrm{q_R}$ are visible in the temperature measurements for the charge in Figures 4a.
- For a charge the lithium reaction is endothermic for $0 < z < 0.3$ or $0.65 < z < 0.9$ and exothermic for $0.3 < z < 0.65$ or $0.9 < z < 1.0$. For a discharge lithium reaction the heat generated and consumed the other way around.

However, the resistor R dependents on the current I and the temperature T, since the curve is significantly different for different current sizes $|I|$ and external temperatures T_s as shown in Figure 5 (bot).

Remark 1. The splitting of q into $\mathrm{q_R}$ and $\mathrm{q_J}$ is not unique. For example another valid approach would be to choose $\mathrm{q_J} = I\,(U - U_{ocv})$. But this does produce very similar $b(z)$ curves.

Remark 2. One of the drawbacks of fitting of $\mathrm{q_R}$ with the method presented in Section III-B is, that we have to make assumptions about $\mathrm{q_J}$ to calculate $\mathrm{q_R}$ and if these assumptions are wrong $\mathrm{q_R}$ is wrong as well.

Remark 3. One of the advantages is that no knowledge about the cathode/anode material is needed. The exact composition of these materials is often kept secret by battery manufacturers and can change over the lifetime of the cell. Additionally, the method presented in Section III-B is non-destructive. Therefore, with this method the change of $\mathrm{q_R}$ over the lifetime of a battery cell can be calculated.

IV. Impact on the Multi-Physics-Model

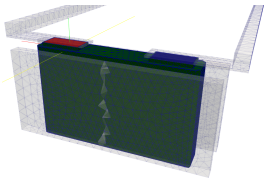

(a) Cell Mesh

Element Type	# Elements	# Nodes
Total	33840	52219
Tetrahedrons	32874	48966
Hexahedrons	540	1818
Pyramids	426	1434

(b) Mesh Overview

Fig. 6: *Overview over the mesh of the commercial battery cell in its test bed.*

A. Simulations Overview

In Section III a method to calculate the entropy $b(z) = \frac{\partial U_{ocv}}{\partial T}$ and the resulting reversible heat source $\mathrm{q_R} = ITb(z)$ is introduced. In this section the resulting reversible heat source $\mathrm{q_R}$ of the commercial battery cell is validated with a different current profile and $T_s = 20°C$, shown in Figure 7a. This cell is simulated using the 3d multi-physics model discussed in Section II-B which is discretized using the finite element method and a mesh with 33840 elements, see Figure 6. Four simulations have been calculated with and without a reversible heat sources and with two different

TABLE II: Overview of 3d Multi-Physics Simulations

Name	$\mathrm{q_R}$	$\mathrm{q_J}$	Calculation Time
Sim. 1	0	$I(U - U_{ocv})$	$3h\ 48min$
Sim. 2	0	RI^2	$3h\ 51min$
Sim. 3	$ITb^p(z)$	$I(U - U_{ocv})$	$3h\ 59min$
Sim. 4	$ITb^p(z)$	RI^2	$4h\ 2min$

Joule's heat sources, see Table II. In the simulations the approximation $b^p(z) = 0.0114z^4 - 0.0213z^3 + 0.0114z^2 - 0.0013z - 0.0001$ of the entropy $b(z)$ is used. For $\mathrm{q_J} \approx RI^2$ a resistor model is used with $R = 0.0018$, R is shown in Figure 5 (bot) in black. The different Joule's heat source $\mathrm{q_J}$ are plotted over the whole time in Figure 7c.

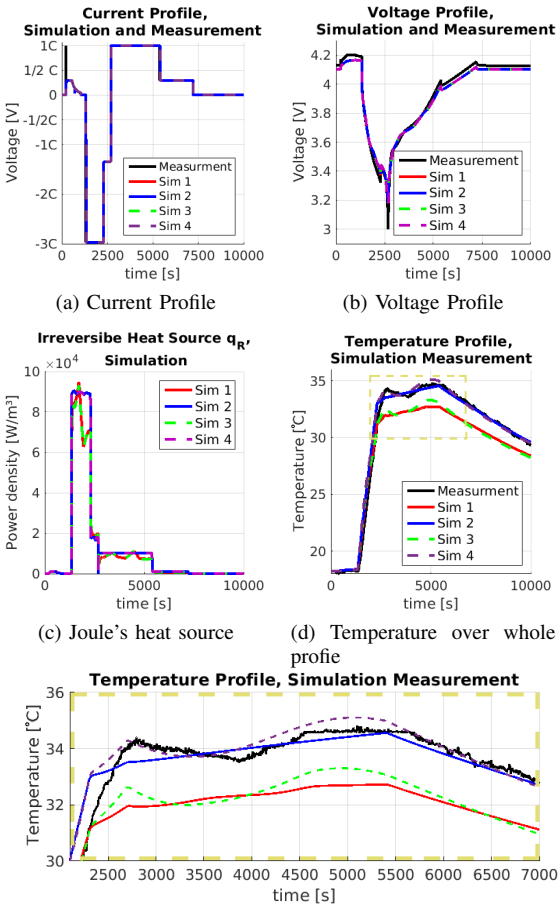

(a) Current Profile

(b) Voltage Profile

(c) Joule's heat source

(d) Temperature over whole profie

(e) Temperature in part "Current $< 1C$"

Fig. 7: *Temperature, current on the cell case. Calculated with the multi-physics finite element solver.*

The results from the simulations are shown in Figure 7. The current profile is:

- Charge with constant voltage to $z = 1$.
- Discharge $1.7C = 110A$ until $t = 2311s$ ($z \approx 0.1$) and discharge $1.35C = 50A$ until $t = 2700s$.
- Charged $1C = 37A$ and $0.30C = 11A$ from .
- When $z \approx 1$ the cell is relaxed for 2.3h.

The output voltage of the simulation does not fit the measured voltage for a small state of charge ($z < 0.1$ which corresponds to $2311s < t < 2700s$), see Figure 7b at time=2700s. In the rest of the simulation the voltage is very close to the measured voltage.

The voltage error results in a systemic temperature error for Sim. 1, 3 after the full discharge at 2700s, because the overpotential $f_U = (U - U_{ocv})$ is too small compared to the measurement, see Figure 7d. On the other hand in Sim. 2, 4 the discharge generates to much temperature for $z > 0.1$ but this is balanced out because it generates to little for $z < 0.1$. The reason for this is that $R = 0.0018$ is an average value and does not change in z. In Sim. 2 and 4 the temperature after the full discharge ($t = at2700s$) is the same as in the measurement, see Figure 7e.

B. Influence of the reversible heat source $\mathrm{q_R}$ on the temperature

If the size of the current $|\,I\,|$ in Figure 7a are compared with the constant model in Figure 3, we see that the currents used in the discharge are already too high for the reversible heat source $\mathrm{q_R}$ to make a large impact, since the constant model shows us that $6.5\,\mathrm{q_R}(1C) < \mathrm{q_J}(1C)$. And we see that for $I = 3C$ the reversible heat source $\mathrm{q_R}$ has nearly no impact. But for the $1.7C$ discharge ($t \in (2300s, 2700s)$) $\mathrm{q_R}$ has an impact, see Figure 7e.

For the charge from $t > 2700s$ onwards we see that the temperature cooling and heating generated by $\mathrm{q_R}$ is the same in the measurement and in the simulation. But for smaller currents ($t > 7000s$) the heat sources make not much difference in this simulation, since the cooling generated from the difference between the temperature $35°C$ on the cell to the external temperature $T_s = 20°C$ is too large. But if the temperature of the cell is closer to the external temperature an impact of $\mathrm{q_R}$ is expected even for lower currents.

The distinct pattern of cooling, heating and cooling between 2700s and 6000s in Figure 7e is matched by the simulation, independent of the chosen irreversible heat source $\mathrm{q_J}$.

Altogether the simulated temperature fits closely the measured temperature and the reversible heat source is a needed addition especially if lower currents than in Figure 7a are considered.

V. Conclusion

For lower temperatures ($T < 0°C$) batteries can only discharge and charge small currents. In this scenario the battery has to heat up to a better working temperature. This can happen for example to car batteries in winter. This scenario is researched in the FFG national funded project eMPROVE *http://www.iesta.at/emprove*. In this application the thermal management is important. If the battery can not heat itself to the working temperature it has to be heated up from the outside.

The reversible heat source $\mathrm{q_R} = TIb(z)$ is necessary for a thermal analysis of battery cells in low current situations as seen in Figure 3. However, the batteries used in automotive industry are designed such that the U_{ocv} varies very little in the temperature T. Hence, this paper explores a method to calculate the entropy $b(z) = \frac{\partial U_{ocv}}{\partial T}$ based on the energy balanced in (3), which is used to find $b(z)$ for a commercial battery cell in Section III. The resulting entropy $b(z)$ over the state of charge z is shown in Figure 5. The energy balanced based method works also for cells, where the open-circuit voltage U_{ocv} varies very little in the temperature T as it is the case for the cell examined in this paper. Additionally, no knowledge about the cell chemistry is needed. However, temperature measurements for charge and discharge are needed to calculate $b(z)$.

In the Section IV the calculated entropy $b(z)$ for a commercial battery cell is used in a multi-physics model. The resulting temperature curve matches the measured temperature of the commercial battery cell better than the simulation without $\mathrm{q_R}$. Even though the current used in the simulation is mostly higher than $1C$, the reversible heat source $\mathrm{q_R}$ still has an impact on the temperature of the cell.

The reversible heat source $\mathrm{q_R}$ and related topics still has to be studied in more detail. For example the method in this paper has to be validated with different cells and compared to other methods which calculate $b(z)$.

Another interesting topic is the difference of $b(z)$ for cells with the same cell chemistry, i.e has only the material an effect on $b(z)$ or have production methods an impact as well.

It is known that the $U_{ocv}(z)$-curve can change when cells are aging. But to our knowledge the impact on $b(z)$ is not known and the method introduced in this paper is a good candidate to study this since it is non-destructive and the measurements are simple to perform.

More detailed measurements and simulations will be performed in the field of the reversible heat source $\mathrm{q_R}$ to evaluate the existing results.

References

[1] C. Pals, J. Newmann. Thermal modeling of the lithium/polymer battery. *Journal of The Electrochemical Society*, 142(10):3274–3281, 1995.

[2] D. Bernardi, E. Pawlikowski, J. Newman. A general energy balance for battery systems. *Journal of The Electrochemical Society*, 132:5–12, 01 1985.

[3] D. Jeon, S. Baek. Thermal modeling of cylindrical lithium ion battery during discharge cycle. *Energy Conversion and Management*, 52(8):2973 – 2981, 2011.

[4] F. Pichler, N. Koester, A. Thaler. Thermo-electric simulation of battery-modules with reduced order modelling of linear electrical components. *COMPEL - The international journal for computation and mathematics in electrical and electronic engineering*, 36(5):1488–1500, 2017.

[5] G. Plett. *Battery Modeling*. Artech House, 2015.

[6] H. Giel, D. Henriques, G. Bourne, T. Markus. Investigation of the heat generation of a commercial 2032 (LiCoO2) coin cell with a novel differential scanning battery calorimeter. *Journal of Power Sources*, 390:116 – 126, 2018.

[7] O. Steinbach. *Numerical Approximation Methods for Elliptic Boundary Value Problems. Finite and Boundary Elements*. Springer Verlag, 2008.

[8] R. Williford, V. Viswanathan, J. Zhang. Effects of entropy changes in anodes and cathodes on the thermal behavior of lithium ion batteries. *Journal of Power Sources*, 189(1):101 – 107, 2009.

[9] Y. Reynier, J. Graetz, T. Swan-Wood, P. Rez, R. Yazami, B. Fultz. Entropy of li intercalation in lixcoo2. 70, 11 2004.

Accelerating parameter estimation in Doyle-Fuller-Newman model for lithium-ion batteries

[12]Sohail R. Reddy, [1]Matthias K. Scharrer, [1]Franz Pichler, [3]Daniel Watzenig, [2]George S. Dulikravich

[1]Department of Electrics/Electronics and Software, VIRTUAL VEHICLE Research Center, Graz, Austria
[2]Department of Mechanical and Materials Engineering, Florida International University, Miami, Florida, USA
[3]Graz University of Technology, Graz, Austria

Purpose:
This paper aims to solve the parameter identification problem to estimate the parameters in electrochemical models of the lithium-ion battery.

Design/methodology/approach:
The parameter estimation framework is applied to the Doyle-Fuller- Newman (DFN) model containing a total of 44 parameters. The DFN model is fit to experimental data obtained through the cycling of Li-ion cells. The parameter estimation is performed by minimizing the least-squares difference between the experimentally measured and numerically computed voltage curves. The minimization is performed using a state-of-the-art hybrid minimization algorithm.

Findings:
The DFN model parameter estimation is performed within 14 h, which is a significant improvement over previous works. The mean absolute error for the converged parameters is less than 7 mV.

Originality/value:
To the best of the authors knowledge, application of a hybrid optimization framework is new in the field of electrical modelling of lithium-ion cells. This approach saves much time in parameterization of models with a high number of parameters while achieving a high-quality fit.

Keywords:
Multiphysics, Differential evolution, Optimal design, Finite element method, Evolution strategies, Material modelling

Published in COMPEL - The international journal for computation and mathematics in electrical and electronic engineering, Vol. 38 No. 5, 2019, ISSN 0332-1649, page 1533 - 1544

Model order reducibility of nonlinear electro-quasistatic problems

Fotios Kasolis, Markus Clemens

Chair of Electromagnetic Theory, Bergische Universitat Wuppertal,Wuppertal, Germany

Purpose:
This paper aims to develop an automated domain decomposition strategy that is based on the presence of nonlinear field grading material, in the context of model order reduction for transient strongly nonlinear electro-quasistatic (EQS) field problems.

Design/methodology/approach:
The paper provides convincing empirical insights to support the proposed domain decomposition algorithm, a numerical investigation of the performance of the algorithm for different snapshots and model order reduction experiments.

Findings:
The proposed method successfully decomposes the computational domain, while the resulting reduced models are highly accurate. Further, the algorithm is computationally efficient and robust, while it can be embedded in black-box model reduction implementations.

Originality/value:
This paper fulfills the demand to effectively perform model order reduction for transient strongly nonlinear EQS field problems.

Keywords:
Electromagnetic fields, Model order reduction, Time-domain modelling, Computational electromagnetics, Domain decomposition method, Electro-quasistatics, Field grading material, Nonlinear model reduction, Rnyi entropy

Published in COMPEL - The international journal for computation and mathematics in electrical and electronic engineering, Vol. 38 No. 5, 2019, ISSN 0332-1649, page 1453 - 1464

Multiphysics field computations for high-end smart sensor design

André Buchau[1] and Jens Anders[1,2]
[1]University of Stuttgart, Institute of Smart Sensors, Pfaffenwaldring 47, 70569 Stuttgart, Germany
[2]Integrated Center of Quantum Science and Technology (IQST), Stuttgart, Germany
E-mail: andre.buchau@iis.uni-stuttgart.de

***Abstract*—Smart sensors bear the potential to revolutionize all aspects of our everyday life, ranging from smart homes that benefit from ambient assisted living, optimized production lines in the frame of Industry 4.0 to high-end sensors that enable entirely new experiments in the scientific world. For an optimum system performance especially of the latter type, multiphysics field problems have to be considered for the physical sensor along with advanced interface circuits to process the measured signals in-situ. Since smart sensors often operate at the limit of what is technical feasible, very precise and reliable models of the relevant multiphysics fields are required in combination with high-level models to describe the complete sensor system. An innovative approach based on software agents enables the solution of these complex multi-layer simulation models in a very flexible and efficient way. A coupling of the finite element method with the boundary element method along with a meshfree post-processing is ideally suited to tackle the challenging task of multiphysics field computations for smart sensors.**

***Index Terms*—boundary element method, finite element method, multiphysics problems, smart sensors, software agents**

I. Introduction

A smart sensor consists of two main components, a physical sensor and a custom-made mixed signal interface circuit (Fig. 1). The physical sensor measures physical quantities such as magnetic, electric or temperature fields. Its output signals, frequently given by electric voltages, are processed in-situ using a dedicated interface circuit, which processes the signal and extracts information about the measurand [1]. Here, especially a co-integration of the physical sensor together with the interface electronics on a single application-specific integrated circuit (ASIC) offers entirely new possibilities in low-noise analogue signal processing combined with digital signal processing. As an example, a mobile electron spin resonance (ESR) spectrometer (Fig. 2) that uses this approach paves the way towards fast and easy-to-handle measurements of free radicals in blood samples [2].

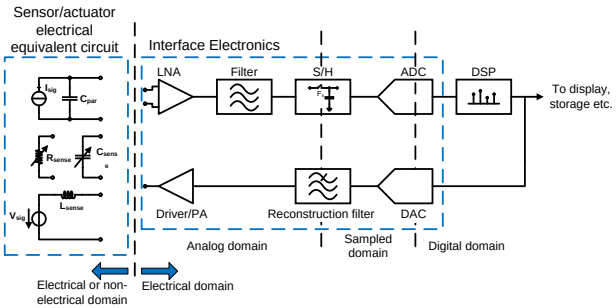

Fig. 1: Block diagram of a smart sensor

For the design of smart sensors, complex multiphysics field problems have to be solved to model the physical sensor performance accurately. They require the simultaneous description of multiple physical effects together with an efficient and robust numerical model. The simulation accuracy has to be frequently very high, since the sensor signals often present a small deviation from a large offset value. Therefore, a combination of the finite element method (FEM), boundary element method (BEM), fast and efficient solvers, and a flexible coupling concept using software agents is a solid basis to tackle this challenging task [3].

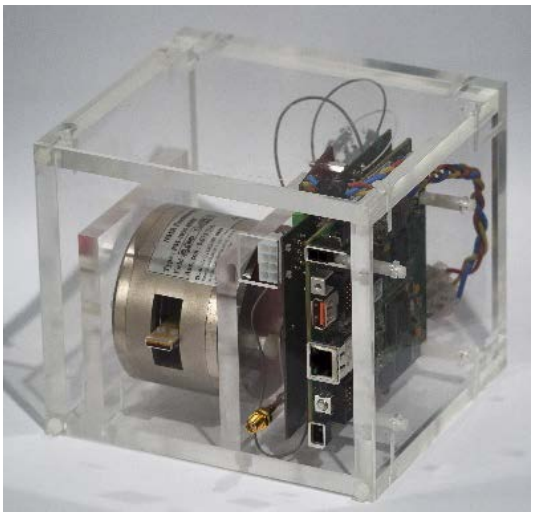

Fig. 2: Portable electron spin resonance spectrometer

Here, the focus is on the efficient solution of the multiphysics field problem of the physical sensor in the context of a multi-layer model of the smart sensor. This elegant approach enables both a comprehensible system model as well as precise finite element methods models for accurate field computations. Furthermore, a combination of the finite element method with a state of the art implementation of the boundary element method including meshfree post-processing is shown along with appropriate visualization techniques.

II. System Model of the Smart Sensor

Due to the high complexity of a smart sensor, a multilayer model is necessary for its efficient and accurate description and design (Fig. 3). Only a precise multiphysics field problem captures all relevant physical effects for an exact model, especially of the physical sensor itself. However, a system model simplifies the analysis of the measured signals significantly and is much more efficient.

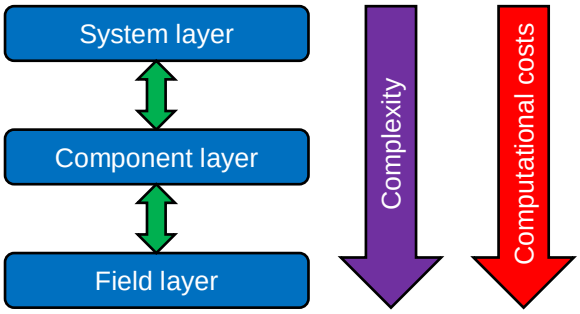

Fig. 3: Multi-layer simulation model for smart sensors

The multi-layer model of the smart sensor consists of three relevant layers. The system layer is the top layer in the model. There, the total sensor system is split into a relatively small number of functional blocks with defined tasks similar to the block diagram of the smart sensor in Fig. 1. Hence, the system layer is clearly structured and relative easy to understand. For this reason, the system layer is indispensable for a top down smart sensor design. The behavior of each block is modeled and described based on the main properties of the block. This approximation of a block results in very fast simulations to characterize and to design the sensor system. However, the determination of these approximation functions is often a challenging task, especially in the case of high accuracy demands.

The middle layer, the component layer, is more complex but also much more accurate. It uses lumped element models, which enable a classical circuit design including tailored analytical and numerical methods [4]. Especially electronic engineers prefer the component layer. Complex equivalent circuit models account for parasitic effects while they are still comprehensible. Very powerful circuit design tools exist to analyze a sensor system at the component layer with high accuracy. However, the increased complexity of this layer results in relative large computational costs. Therefore, a dynamical switch between system layer and component layer is advisable. Using well-defined interfaces, data between both layers is exchanged to determine the precise behavior of system blocks based on circuit models. Overall, an analysis of a smart sensor using a clever combination of system layer and component layer is efficient and in many cases very accurate.

Unfortunately, the component layer is often not accurate enough to analyze the physical sensor along with all relevant fields. Therefore, a detailed field model based on finite element methods as described in the following section is often required. To integrate such a field model into the component model, lumped ports have to be defined. Then, a weak or a strong coupling of the field layer with the component layer can be realized.

In total, different views of the smart sensor are obtained. For a successful design of such a complex sensor system, a combination of all types of models on all three layers is necessary, typically requiring deep expert insights to design such systems.. Thus, we suggest an innovative software agent based approach to tackle this problem and to integrate machine learning methods as a way to include/substitute expert knowledge.

Software agents are a very powerful tool to manage complex systems [5] and are an established approach to control large automation systems. Here, software agents are applied to control the above-described multi-layer model of a smart sensor. A software agent is ideally suited to encapsulate a numerical simulation tool based on general applicable data interfaces. This enables a very flexible mixture of simulation tools on different simulation layers via the software agent approach. Typically, a software agent in a multi-agent system has not only the computing capabilities of the simulation tool but it also has access to dedicated computer resources such as CPU and memory. All n software agents of a system communicate using classical network protocols (Fig. 4).

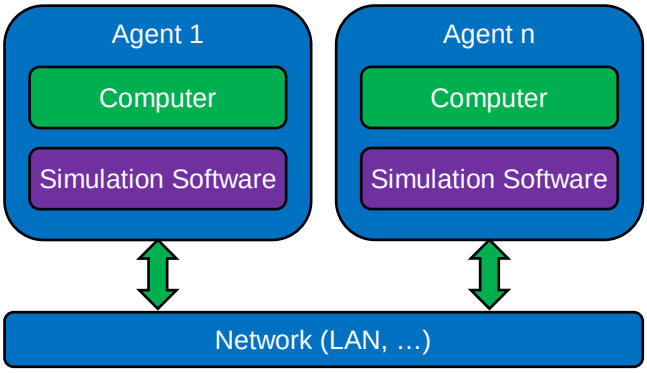

Fig. 4: Software agent system for simulation of smart sensors

In addition to the computing resources, another main property of a software agent is that it has a defined goal and that it interacts with other software agents by observing its environment. In the context of a multi-layer smart sensor model, the goal of a software agent is to find the numerical solution for its assigned sub-problem, for instance the solution of the field problem of the physical sensor. The observation of its environment corresponds to the evaluation of exchanged physical values and can be the input currents and voltages of a coil in a sensor.

Since a software agent acts autonomously to achieve its goal, the software agent decides if a simulation is executed or not. That means, if the retrieved physical values are approximately the same as in the previous computational step, the software agent has the choice to reuse the simulation results of the previous step instead of a newly computed value. In such a way, a weak coupling between system blocks, components, and multiphysics field models is established. Finally, the software agent system computes the solution of the complete smart sensor model. The advantage of the software agent system is that it is much more flexible than a classical algorithm based approach. Additional software agents are created very easily along with a dynamic reconfiguration of the software agent system. This enables fast switching between the model layers and the use of different layers at each computational step.

Furthermore, the use of a software agent system is ideally suited to gain additional information about the smart sensor and about the configuration of the simulation tools. The basis for this is that computing time is very cheap today. Therefore, additional computations are possible that can be then efficiently coordinated by software agents. In

practice this means that software agents can execute redundant computations using different simulation models at multiple model layers or that a simulation model is used with a variation of solution methods and parameters. Of course, these additional computations use only idle resources. After the redundant solution of a sub-problem, the software agents compare their results and the most accurate or most efficient solution is used. In combination with machine learning, the result of the redundant computation is evaluated and stored. Then, this knowledge is applied in a future computation to optimize the solution process of the simulation directly.

Another possibility of the software agent based approach is to vary parameters of the smart sensor. This allows gaining knowledge about the relation between design parameters and, e. g., readout signals. Since these additional computations are automatically generated and evaluated, this knowledge gain is obtained without interaction of the user. A machine learning based evaluation of the solution enables more efficient computations than classical parameter sweeps. In contrast to optimization methods, a cost function is not necessary and a function, which characterizes the smart sensor, is obtained.

The software agent based approach has been tested very successfully for the solution of multiphysics field problems [6]. There, a coupled three-dimensional problem including electromagnetic wave propagation and heat transfer was studied. Each physical problem was assigned to one software agent. Hence, the coupling between electromagnetic field problem and heat transfer problem was realized by the communication between the software agents only. The advantage was that different solvers could be used for both sub-problems.

An extension of the software agents with a neural network demonstrates the strength of software agents in combination with machine learning methods [7]. There, parameters to characterize the studied field problem have been introduced and used to select an appropriate solution method. The advantage of the software agents in that case is that training data is generated also in future computations by some redundant computations. The obtained results show the tremendous potential of the proposed approach, especially in combination with a central database system and a large user group.

The advantage of redundant computations is also very clearly observable in the case of time-dependent field problems [8]. Multiple software agents solve the same time-dependent problem in parallel but with different time-step sizes. Then, the most accurate solution is selected using the error estimate method of the applied solver. The result was that the total number of time-steps could be significantly reduced along with the computation time, which is relevant for a user. Of course, some unnecessary computations were executed, but the advantage of a reduced total simulation time predominates.

In total, the already obtained results of software agents in the context of numerical field computations clearly demonstrate the viability of this approach for the solution of the multi-layer model of smart sensor is very promising. Therefore, the introduction of a coordination agent, which manages the solution process and which interacts with the user is very promising. These software agents can efficiently use the available computers at an institution along with multiple simulation tools. Especially if this approach is applied by a large group of users with a large number of numerical examples, the benefit of a machine learning method with a centralized database can be tremendous.

III. Multiphysics Field Problems

At the field layer, classical multiphysics field problems have to be solved. Here, we present efficient methods, which are adapted to the special situation in smart sensor design. Since our smart sensors are small and often applied in an environment, which is much larger than the sensor itself, special attention is paid to an advanced coupling of the finite element method with the boundary element method. Furthermore, the potential of software agents and of software module based approaches is discussed.

As shown in the previous section, precise field computations are necessary in the context of smart sensor design. Therefore, three aspects are relevant for a successful application of multiphysics models (Fig. 5). First, a sound theoretical description of all physical effects in the smart sensor is indispensable. This includes the partial differential equations of e. g. electromagnetic fields, heat transfer, structural mechanics, or fluid dynamics. Of course, properly chosen boundary conditions are required, too. A challenge is a physically meaningful initial condition in the case of time-dependent problems. Second, a simulation model is derived and an appropriate numerical formulation is chosen. Here, we prefer the finite element method, the boundary element method or a combination of both methods depending on the problem at hand. Simulations enable a deep insight into the studied multiphysics problem, since the relevance of individual physical effects can be computed separately and effects of design changes are determinable for the real three-dimensional physical sensor by an evaluation of very accurate numerical field values. Finally, the third pillar of our design concept is the evaluation and characterization of the smart sensor by measurements. There, the accuracy of the analytical and the numerical model is eventually verified. Furthermore, measurements enable an improvement of these models mainly with respect to material models. In total, only a combination of a sound theory, appropriate numerical simulations, and measurements with realized manufactured sensor hardware lead to a successful smart sensor design.

As demonstrated in the previous section, the concept of software agents is very well applicable for the solution of time-depend multiphysics problems. Mainly the difficult task of coupling multiple physics, which are often solved using specialized software implementations for each physics, is tackled very elegantly by software agents. On the layer of computational domains of a single physics problem, several approaches exist.

A single field problem, which is split into multiple subproblems, is solvable by a software agent approach, too. There, the geometrical sensor model is divided based on domain boundaries. Instead of classical domain decomposition approaches, the coupling between the computational

domains is realized by a software agent system. The main advantage of such a coupling approach is that the domains can be solved using not only different numerical methods but also different software implementations.

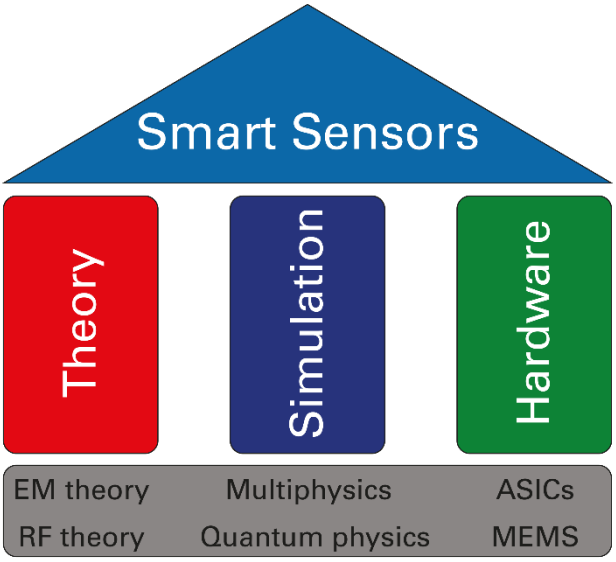

Fig. 5: Three pillars of knowledge gain in smart sensor design

Another very interesting approach is a direct integration of two software tools into one framework. Therefore, we developed our software MuPhyN (multiphysics numerics). The main component is our BEM solver for the solution of electrostatic and magnetostatic field problems [(Fig. 6). Another component is a general interface to the finite element method, which has recently been adapted to the commercial FEM software COMSOL Multiphysics. Besides classical coupling methods of BEM and FEM, a focus is on the common post-processing of both methods.

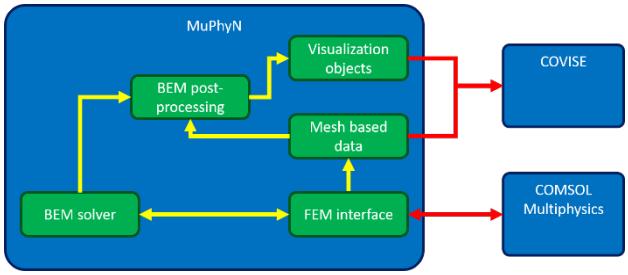

Fig. 6: Block structure of multiphysics software MuPhyN

A numerical field computation process consists of two important steps. First, the solution is computed on the finite elements. There, specifics of the underlying numerical methods are considered, for instance that the solution is computed on domain boundaries only in the case of the BEM. Second, the computed results are evaluated during the post-processing step. This means that the results are processed for an analysis by the user, e. g. by an appropriate visualization of field values.

The visualization of field values should be independent of the applied solution methods. This seems to be obvious but this requirement demands highly developed post-processing techniques, especially for the BEM [10]. The problem is that for a deep insight into a field problem, field values have to be visualized inside domains. Therefore, domain data are required. One possibility is to compute field values even in the case of a BEM in the nodes of a grid or mesh and to apply standard visualization tools like the open source software COVISE [11]. The significant drawback of such an approach is that field values are computed with high computational costs on a huge number of points while most of these values are not used for visualization, since rendered figures should be clear. Therefore, an efficient meshfree post-processing for the BEM was introduced [10].

The basis of a meshfree post-processing is an automatic domain detection method. In contrast to FEM, where domain data are available, a BEM model consists only of a description of domain boundaries. Especially in the case of complexly shaped domain boundaries, a robust and efficient method is necessary to detect the domain of an evaluation point reliable. Domain data are needed in many cases to determine material data, which is also involved in the field value computation. Furthermore, field line computations should be restarted at domain boundaries to obtain sharp bends of field lines at domain boundaries [12].

Octree schemes are a common technique in visualization to sort data and to compute for instance isosurfaces [13]. Furthermore, octrees are the basis of the fast multipole method, which is one of the established methods for matrix compression in boundary element methods. We developed a much more flexible version of the fast multipole method. There, the compression techniques are also applied to increase the efficiency of post-processing integral computations. An integration of BEM into visualization methods enables computations of field values only at points, which are necessary for visualization. Hence, the number of field computations is drastically reduced in comparison to classical approaches. The efficiency of this proposed method was demonstrated for field line computations using a reversed fast multipole method [12] and for isosurface computations based on a common octree scheme [14].

In the case of a coupling of BEM and FEM, our innovative BEM post-processing approach has to be integrated and combined with classical FEM post-processing. To this end, we developed a powerful data interface between our software MuPhyN and the visualization software COVISE. Depending on the applied numerical method in a domain, field values on a volume mesh are prepared or visualization objects such as field lines are computed directly (Fig. 6). Then, both types of data are transferred to the visualization tool (Fig. 7). For the highest possible flexibility, the open data protocol (OData) is used [15]. It encapsulates data in extensible markup language (XML) format and establishes the connection between the processes of MuPhyN and COVISE based on hypertext transfer protocol (http). This allows running the field computation and the visualization on the same computer or on different machines. In COVISE an application specific module was added to use the powerful visualization methods of COVISE for the FEM data and to combine them with already computed visualization objects from BEM. Finally, the merged result is rendered in virtual or augmented reality.

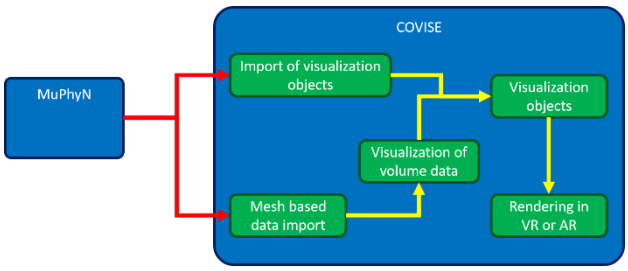

Fig. 7: Block structure of visualization of mixed data obtained from a coupling of BEM with FEM

As an example for computation of fields in a smart sensor, the magnetic field of the physical sensor of our portable ESR spectrometer [2] was computed. The core of the sensor is a coil, which interacts with the electron spins of the sample under investigation. The coil is integrated on the ASIC to increase the quality of the measured signal and to shorten the distance to the mixed-signal processing. In Fig. 8 the coil is shown along with a symbolic representation of the electron spins of the sample in the magnetic field of the coil.

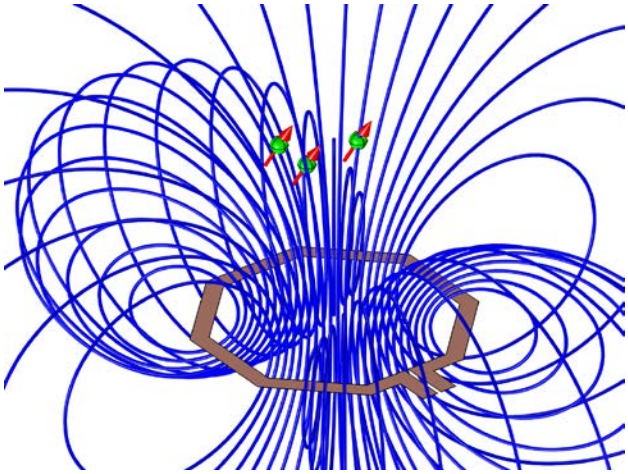

Fig. 8: Magnetic field of the coil of a mobile ESR spectrometer

IV. Conclusions

A very powerful and flexible approach based on software agents has been presented that allows simulating smart sensors using a multi-layer simulation model. There, multiple specialized simulation tools are combinable and redundant computations with a parameter variation along with machine learning methods enable a deep insight into the studied smart sensor. At the field layer, a clever coupling of the finite element method with an advanced boundary element method is recommended for the solution of multiphysics fields in the context of smart sensors. Especially our proposed post-processing, which combines classical FEM evaluations with innovative meshfree BEM methods, improves the smart sensor design significantly.

References

[1] G. Meijer et al. Smart Sensor Systems: Emerging Technologies and Applications, Wiley

[2] B. Schlecker et al., "VCO-based ESR-on-a-chip as a tool for low-cost, high-sensitivity point-of-care diagnostics," 2017 IEEE SENSORS, Glasgow, 2017, pp. 1-3.

[3] A. Buchau and M. Jüttner, „A concept of separated numerical formulations for the solution and evaluation of complex field problems“, International Journal of Computational Methods and Experimental Measurements, vol. 6, no. 6, pp. 1008-1018, 2018

[4] F. N. Najm, “Circuit Simulation”, Wiley-IEEE Press, ISBN: 978-0-470-56120-1, 2010

[5] N. R. Jennings, “Agent-Oriented Software Engineering”, I. Imam, Y. Kodratoff, A. El-Dessouki, M. Ali (eds.) Multiple Approaches to Intelligent Systems, IEA/AIE 1999, Lecture Notes in Computer Science, Vol. 1611, Springer, Berlin, Heidelberg, 1999

[6] M. Jüttner, A. Buchau, D. Vögeli, W. M. Rucker, P. Göhner, “Iterative Software Agent Based Solution of Multiphysics Problems”, A. Bartel, M. Clemens, M. Günther, E. ter Maten (eds.) Scientific Computing in Electrical Engineering: Mathematics in Industry, Vol. 23, Springer, pp. 123-131, 2016

[7] M. Jüttner, J. Falk and W. M. Rucker, "A Neural Network Based Recommendation System for Solvers and Preconditioners for Systems of Linear Equations," IEEE Transactions on Magnetics, Vol. 53, No. 6, pp. 1-4, June 2017, Art no. 7202904

[8] M. Jüttner, S. Grabmaier, J. Rohloff, D. Vögeli, W. M. Rucker, P. Göhner, and M. Weyrich, “A distributed method for transient simulations that dynamically considers supplementary results from autonomous software agents,” Informatyka, Automatyka, Pomiary w Gospodarce i Ochronie Środowiska, Vol. 8, No. 2, pp. 35–38, 2018

[9] A. Buchau, W. Hafla, F. Groh, and W. M. Rucker, “Fast multipole method based solution of electrostatic and magnetostatic field problems,” Computing and Visualisation in Science, Vol. 8, No. 3–4, pp. 137–144, 2005

[10] A. Buchau, W. M. Rucker, “Feasibility of a meshfree post-processing for boundary element methods”, Boundary Elements and Other Mesh Reduction Methods XXXVIII, WIT Press, pp. 327–338, 2015

[11] W. Hafla, A. Weinläder, A. Bardakcioglu, A. Buchau, and W. M. Rucker, “Efficient Post-Processing with the Integral Equation Method,” COMPEL, Vol. 26, No. 3, pp. 873–887, 2007

[12] A. Buchau and W. M. Rucker, “Meshfree computation of field lines across multiple domains using fast boundary element methods,” IEEE Transactions on Magnetics, 2015

[13] J. Wilhelms and A. van Gelder, “Octrees for Faster Isosurface Generation”, ACM Transactions on Graphics, Vol. 11, No. 3, pp. 201-227, 1992

[14] A. Buchau, W. M. Rucker, “A meshfree isosurface computation method for boundary element methods”, International Journal of Computational Methods and Experimental Measurements Vol. 5 No. 5, pp. 647 – 658, 2017

[15] Open Data Protocol (OData), OASIS, Advancing open standards for the information society, www.oasis-open.org

A novel variant of the H - Φ field formulation for magnetostatic and eddy current problems

Jasmin Smajic

Institute for Energy Technology, University of Applied Sciences of Eastern Switzerland (HSR), Rapperswil, St. Gallen, Switzerland

Purpose:
The paper presents a new variant of the H-U field formulation for solving 3-D magnetostatic and frequency domain eddy current problems. The suggested formulation uses the vector and scalar tetrahedral elements within conducting and non-conducting domains, respectively. The presented numerical method is capable of solving multiply connected regions and eliminates the need for computing the source current density and the source magnetic field before the actual magnetostatic and eddy current simulations. The obtained magnetostatic results are verified by comparison against the corresponding results of the standard stationary current distribution analysis combined with the Biot-Savart integration. The accuracy of the eddy current results is demonstrated by comparison against the classical A-A-f approach in frequency domain.

Design/methodology/approach:
The theory and implementation of the new H-U magnetostatic and eddy current solver is presented in detail. The method delivers reliable results without the need to compute the source current density and source magnetic field before the actual simulation.

Findings:
The proposed H-U produce radically smaller and considerably better conditioned equation systems than the alternative A-A approach, which usually requires the unphysical regularization in terms of a low electric conductivity value within the nonconductive domain.

Originality/value:
The presented numerical method is capable of solving multiply connected regions and eliminates the need for computing the source current density and the source magnetic field before the actual magnetostatic and eddy current simulations.

Keywords:
Magnetostatic analysis, Eddy current analysis, H-U field formulation, Multiply connected regions

Published in COMPEL - The international journal for computation and mathematics in electrical and electronic engineering, Vol. 38 No. 5, 2019, ISSN 0332-1649, page 1545 - 1561

Simulating induction heating processes using harmonic balance FEM

Klaus Roppert, Florian Toth, Manfred Kaltenbacher

Institute of Mechanics and Mechatronics, TU Wien, Vienna, Austria

Purpose:
The purpose of this paper is to examine a solution strategy for coupled nonlinear magnetic–thermal problems and apply it to the heating process of a thin moving steel sheet. Performing efficient numerical simulations of induction heating processes becomes ever more important because of faster production development cycles, where the quasi steady-state solution of the problem plays a pivotal role.

Design/methodology/approach:
To avoid time-consuming transient simulations, the eddy current problem is transformed into frequency domain and a harmonic balancing scheme is used to take into account the nonlinear BH-curve. The thermal problem is solved in steady-state domain, which is carried out by including a convective term to model the stationary heat transport due to the sheet velocity.

Findings:
The presented solution strategy is compared to a classical nonlinear transient reference solution of the eddy current problem and shows good convergence, even for a small number of considered harmonics.

Originality/value:
Numerical simulations of induction heating processes are necessary to fully understand certain phenomena, e.g. local overheating of areas in thin structures. With the presented approach it is possible to perform large 3D simulations without excessive computational resources by exploiting certain properties of the multiharmonic solution of the eddy current problem. Together with the use of nonconforming interfaces, the overall computational complexity of the problem can be decreased significantly.

Keywords:
Keywords Induction heating, Multiphysics, Finite element method, Coupled systems, Computational electromagnetics, Magnetic nonlinearity

Published in COMPEL - The international journal for computation and mathematics in electrical and electronic engineering, Vol. 38 No. 5, 2019, ISSN 0332-1649, page 1562 - 1574

Magnetic coupling of mechanical modes in MRI systems

[1]Christopher Stroehlein, [2]Hermann Landes, [3]Andreas Krug, [3]Peter Dietz

[1]Department of Physics, University of Regensburg, Regensburg, Germany
[2]SIMetris GmbH, Erlangen, Germany
[3]Siemens Healthcare GmbH, Erlangen, Germany

Purpose:
The purpose of this paper is to investigate magneto-mechanical coupling occurring in magnetic resonance imaging (MRI) systems. The authors study influence of the strength of the background field on the coupling of mechanically isolated, conductive cylindrical structures and the so-called shields. This coupling has a strong impact on frequency-dependent thermal losses occurring in the shield structures which are of high importance in MRI systems.

Design/methodology/approach:
In the investigations, numerical methods are applied. First, finite element methods taking into account the full magneto-mechanical coupling are used to investigate the coupled physical phenomena. As these calculations may be time-consuming, several approximate predictive methods are derived. Modal expansion factors and participation factors are based on combinations of structural eigenmode calculations and eddy current calculations using BiotSavart representations of the dynamic gradient field. In addition, a parallelism factor expressed in terms of the shield vibrations is defined to measure the coupling between the distinct cylinders.

Findings:
It is found that the strength of the background field strongly influences the coupling of the distinct shields, which strongly increases the parallelism of the shield vibrations. Furthermore, modal expansion and participation factors are significantly influenced, caused by frequency shifts due to magnetic stiffening and increased magnetic coupling.

Originality/value:
The defined factors estimating parallelism and modal participation in magnetomechanical coupling are original work and studied for the first time.

Keywords:
Numerical analysis, Eddy currents, Finite element analysis

Published in COMPEL - The international journal for computation and mathematics in electrical and electronic engineering, Vol. 38 No. 5, 2019, ISSN 0332-1649, page 1575 - 1583

A non-smooth Newton method for the solution of magnetostatic field problems with hysteresis

Stephan Willerich, Hans-Georg Herzog

Institute of Energy Conversion Technology, Technical University of Munich (TUM), Munich, Germany

Purpose:
The use of gradient-based methods in finite element schemes can be prevented by undefined derivatives, which are encountered when modeling hysteresis in constitutive material laws. This paper aims to present a method to deal with this problem.

Design/methodology/approach:
Non-smooth Newton methods provide a generalized framework for the treatment of minimization problems with undefined derivatives. Within this paper, a magnetostatic finite element formulation that includes hysteresis is presented. The non-linear equations are solved using a nonsmooth Newtonmethod.

Findings:
The non-smooth Newton method shows promising convergence behavior when applied to a model problem. The numbers of iterations for magnetization curves with and without hysteresis are within the same range.

Originality/value:
Mathematical tools like Clarkes generalized Jacobian are applied to magnetostatic field problems with hysteresis. The relation between the non-smooth Newton method and other methods for solving non-linear systems with hysteresis like the M(B)-iteration is established.

Keywords:
Electromagnetic fields, Finite element method, Magnetic hysteresis

Published in COMPEL - The international journal for computation and mathematics in electrical and electronic engineering, Vol. 38 No. 5, 2019, ISSN 0332-1649, page 1584 - 1594

Behavioral Modeling of PM Motors Based on Current- and Position-dependent Inductance Matrix Utilizing Frozen Permeability Method

Yusaku Shutta, Yasuhito Takahashi, and Koji Fujiwara
Doshisha University, Kyoto, Japan
E-mail: ytakahashi@mail.doshisha.ac.jp

***Abstract*— This paper proposes a new behavioral modeling for permanent magnet synchronous motors based on a current- and position-dependent inductance matrix. The model is obtained by separating the fluxes due to permanent magnets and armature current by means of the frozen permeability method. The proposed model has the same accuracy as the behavioral motor model based on flux linkage and can calculate the d- and q-axis inductances and flux linkages due to permanent magnets explicitly.**

***Index Terms*— behavioral model, frozen permeability method, permanent magnet synchronous motor, finite element method**

I. Introduction

To design control system for an interior permanent magnet synchronous motor (IPMSM), it is necessary to accurately grasp the characteristics of the motor such as d- and q-axis inductances and flux linkages due to permanent magnets by considering magnetic saturation and spatial harmonics. Because the simple motor model using the flux linkage and inductance as constants cannot consider their current- and position-dependence, simulation with sufficient accuracy cannot be obtained. Although highly accurate simulation results are obtained from the directly coupled analysis with a finite element method (FEM) and a control system [1], there is a problem that enormous calculation time is required.

To overcome this difficulty, several nonlinear motor models (behavioral models), in which flux linkage and inductance are expressed as a function of armature current and rotor position, have been proposed [2]. In the self-inductance model, since some linearity is assumed when the fluxes generated by permanent magnets are separated from total fluxes, there is a possibility that the accuracy becomes insufficient in the case where the nonlinearity is strong. On the other hand, the flux linkage model is capable of considering magnetic saturation and cross-coupling between d- and q-axes appropriately because this model does not need to separate the fluxes generated by permanent magnets and armature current. Therefore, its accuracy is generally better than the self-inductance model although the d- and q-axis inductances are not explicitly obtained in the flux linkage model.

With this background, this paper proposes a new motor model which can represent self- and mutual inductances directly. The proposed model is derived by separating the fluxes due to permanent magnets and armature current by means of the frozen permeability method (FPM) [3]. Numerical results are presented to demonstrate the validity of the proposed model. In addition, a circuit simulation including a control system with a proposed behavioral model considering current- and position-dependence of d- and q-axis inductances and flux linkage due to permanent magnets is performed. The simulated results by the proposed model are compared with those by the simple motor model using constant flux linkage and inductance.

II. Behavioral Model Considering Current- and Position-dependent

Behavioral models utilize table data as nonlinear circuit elements in circuit simulation, which are calculated by the FEM regarding d- and q-axis currents as parameters. This paper compares the inductance matrix model (proposed model) based on the FPM with the self-inductance model and the flux linkage model widely used among the behavioral models.

A. Self-inductance Model

The circuit equation of the self-inductance model is given by

$$\begin{bmatrix} \upsilon_{\mathrm{d}} \\ \upsilon_{\mathrm{q}} \end{bmatrix} = R_{\mathrm{a}} \begin{bmatrix} i_{\mathrm{d}} \\ i_{\mathrm{q}} \end{bmatrix} + \begin{bmatrix} pL_{\mathrm{d}} & -\omega L_{\mathrm{q}} \\ \omega L_{\mathrm{d}} & pL_{\mathrm{q}} \end{bmatrix} \begin{bmatrix} i_{\mathrm{d}} \\ i_{\mathrm{q}} \end{bmatrix} + \begin{bmatrix} 0 \\ \omega \Psi_{\mathrm{m}} \end{bmatrix}, \quad (1)$$

where υ_{d}, υ_{q}, i_{d}, i_{q}, L_{d}, L_{q} are the d- and q-axis voltages, currents, self-inductances, R_{a} is the coil resistance, p is the differential operator with respect to time (d/dt), and ω is the angular frequency. Ψ_{m} is flux linkage due to permanent magnets. By utilizing the d- and q-axis flux linkages Ψ_{d}, Ψ_{q}, each inductance is expressed as

$$L_{\mathrm{d}} = \frac{\Psi_{\mathrm{d}} - \Psi_{\mathrm{m}}}{i_{\mathrm{d}}}, \quad L_{\mathrm{q}} = \frac{\Psi_{\mathrm{q}}}{i_{\mathrm{q}}}. \quad (2)$$

The torque τ is expressed as

$$\tau = P_{\mathrm{n}} \left\{ \Psi_{\mathrm{m}} i_{\mathrm{q}} + \left(L_{\mathrm{d}} - L_{\mathrm{q}} \right) i_{\mathrm{d}} i_{\mathrm{q}} \right\}, \quad (3)$$

where P_{n} is the number of pole pairs.

In the case of the self-inductance model based on (1), it is not easy to separate the d- and q-axis fluxes into the fluxes due to armature currents ($L_{\mathrm{d}}i_{\mathrm{d}}$, $L_{\mathrm{q}}i_{\mathrm{q}}$) and the flux due to permanent magnets (Ψ_{m}). Therefore, there is a limit on improving the accuracy of the self-inductance model even if current- and position-dependence of self-inductances and flux linkages is considered.

B. Flux Linkage Model

The flux linkage model can properly consider magnetic

saturation and cross-magnetization between d- and q-axes because it expresses the flux linkages due to armature current and permanent magnets without separating them. The circuit equation of the flux linkage model is written as

$$\begin{bmatrix} \upsilon_{\mathrm{d}} \\ \upsilon_{\mathrm{q}} \end{bmatrix} = R_{\mathrm{a}} \begin{bmatrix} i_{\mathrm{d}} \\ i_{\mathrm{q}} \end{bmatrix} + \begin{bmatrix} p & -\omega \\ \omega & p \end{bmatrix} \begin{bmatrix} \Psi_{\mathrm{d}} \\ \Psi_{\mathrm{q}} \end{bmatrix}. \tag{4}$$

The torque τ is expressed as

$$\tau = P_{\mathrm{n}} \left(\Psi_{\mathrm{d}} i_{\mathrm{q}} - \Psi_{\mathrm{q}} i_{\mathrm{d}} \right). \tag{5}$$

Although the accuracy of this model is generally better than the self-inductance model, it suffers from the disadvantage that the d- and q-axis inductances cannot be obtained explicitly.

C. Inductance Matrix Model

We propose the motor model based on current- and position-dependent inductance matrix derived by separating the fluxes due to armature current and permanent magnets by utilizing the FPM [4,5]. The FPM can separate flux linkages for each magnetomotive force. Figure 1 shows the principle of the FPM. First, ordinary nonlinear magnetic field analysis is performed using armature current and permanent magnets as magnetomotive force sources. Then, the permeability in each element at each time step is calculated. Finally, under the condition that the permeability is fixed as a constant in each element at each time step, the influence of each magnetomotive force is calculated by performing linear magnetic field analysis.

By utilizing the FPM, the d- and q-axis flux is obtained as

$$\begin{bmatrix} \Psi_{\mathrm{d}} \\ \Psi_{\mathrm{q}} \end{bmatrix} = \begin{bmatrix} L_{\mathrm{d}} & L_{\mathrm{dq}} \\ L_{\mathrm{dq}} & L_{\mathrm{q}} \end{bmatrix} \begin{bmatrix} i_{\mathrm{d}} \\ i_{\mathrm{q}} \end{bmatrix} + \begin{bmatrix} \Psi_{\mathrm{md}} \\ \Psi_{\mathrm{mq}} \end{bmatrix}, \tag{6}$$

where L_{dq} is the mutual inductance and Ψ_{md}, Ψ_{mq} are the d- and q-axis flux linkages due to permanent magnets. Each inductance can be calculated as

$$L_{\mathrm{d}} = \frac{\Psi_{\mathrm{d}}\left(i_{\mathrm{d}}, i_{\mathrm{q}} = 0\right) - \Psi_{\mathrm{md}}}{i_{\mathrm{d}}}, \quad L_{\mathrm{q}} = \frac{\Psi_{\mathrm{q}}\left(i_{\mathrm{d}} = 0, i_{\mathrm{q}}\right) - \Psi_{\mathrm{mq}}}{i_{\mathrm{q}}},$$
$$L_{\mathrm{dq}} = \frac{\Psi_{\mathrm{q}}\left(i_{\mathrm{d}}, i_{\mathrm{q}} = 0\right) - \Psi_{\mathrm{mq}}}{i_{\mathrm{d}}} = \frac{\Psi_{\mathrm{d}}\left(i_{\mathrm{d}} = 0, i_{\mathrm{q}}\right) - \Psi_{\mathrm{md}}}{i_{\mathrm{q}}}. \tag{7}$$

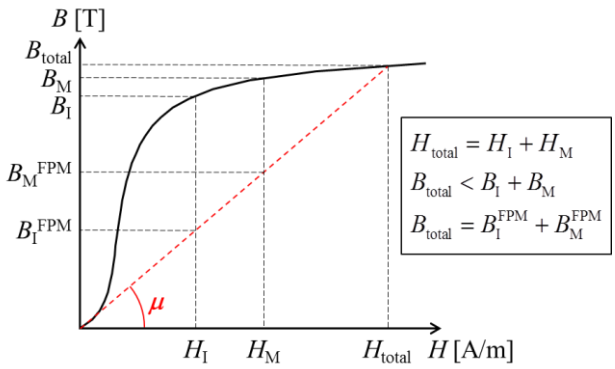

Figure 1 : Principle of the frozen permeability method.

With the help of the FPM, Ψ_{md} and Ψ_{mq} are calculated under the condition of $i_{\mathrm{d}} = i_{\mathrm{q}} = 0$, L_{d} is calculated under the condition of $i_{\mathrm{q}} = 0$, L_{q} is calculated under the condition of $i_{\mathrm{d}} = 0$, and L_{dq} is calculated under the condition of $i_{\mathrm{d}} = 0$ or $i_{\mathrm{q}} = 0$. Therefore, it is necessary to carry out the linear magnetic field analysis three more times compared with the flux linkage model.

By substituting (6) into (4) and (5), the inductance matrix model is obtained as

$$\begin{bmatrix} \upsilon_{\mathrm{d}} \\ \upsilon_{\mathrm{q}} \end{bmatrix} = R_{\mathrm{a}} \begin{bmatrix} i_{\mathrm{d}} \\ i_{\mathrm{q}} \end{bmatrix} + \begin{bmatrix} p & -\omega \\ \omega & p \end{bmatrix} \begin{bmatrix} L_{\mathrm{d}} & L_{\mathrm{dq}} \\ L_{\mathrm{dq}} & L_{\mathrm{d}} \end{bmatrix} \begin{bmatrix} i_{\mathrm{d}} \\ i_{\mathrm{q}} \end{bmatrix} + \begin{bmatrix} p & -\omega \\ \omega & p \end{bmatrix} \begin{bmatrix} \Psi_{\mathrm{md}} \\ \Psi_{\mathrm{mq}} \end{bmatrix}, \tag{8}$$

$$\tau = P_{\mathrm{n}} \left\{ \Psi_{\mathrm{md}} i_{\mathrm{q}} + \left(L_{\mathrm{d}} - L_{\mathrm{q}} \right) i_{\mathrm{d}} i_{\mathrm{q}} - \Psi_{\mathrm{mq}} i_{\mathrm{d}} + L_{\mathrm{dq}} \left(i_{\mathrm{q}}^2 - i_{\mathrm{d}}^2 \right) \right\}. \tag{9}$$

Although the flux linkages due to armature current and permanent magnets are separated by utilizing the FPM, the total flux linkages can be reproduced perfectly. Therefore, this method has the same calculation accuracy as the flux linkage model.

III. Accuracy Verification of Each Behavioral Model

In order to verify the accuracy of each behavioral model, we compare the voltage waveform and the torque obtained when a sinusoidal current is imposed to the IPMSM with concentrated winding, which is the benchmark motor proposed by IEEJ called D1 model [6]. TABLE I and Figure 2 show the analysis conditions and mesh of D1 model. The frequency is 50 Hz, and one period is divided into 180 time steps.

Figures 3 shows the d- and q-axis voltage waveforms

TABLE I
Analysis conditions.

Number of elements	7,644
Number of nodes	3,872
Number of poles	4
Number of stator slots	6
Number of coil turns (per teeth)	125
Rated current [A_{rms}]	4.4
Rated torque [Nm]	1.8
Coil resistance [Ω/phase]	0.38
Magnetization of magnet [T]	1.225
Grade of electrical steel sheet	M300-35A5

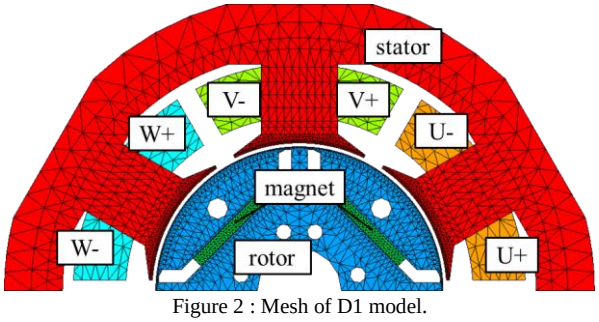

Figure 2 : Mesh of D1 model.

when three-phase sinusoidal currents corresponding to the effective current I_{rms} = 4.4 A and current phase angle β = 20 deg is applied to the D1 model under the condition of rotation speed N = 1,500 min^{-1}. In the self-inductance model, the position dependence of Ψ_m is obtained from the finite-element analysis at no load, and the current- and position- dependence of L_d and L_q are calculated from (2). From Figure 3, d- and q-axis voltages obtained from the self-inductance model are different from the results obtained by the FEM. Because the d- and q-axis flux linkages have strong nonlinearity in this motor, it is difficult to reproduce the numerical results of the FEM by the self-inductance model. By contrast, the d- and q-axis voltages obtained from the flux linkage model and the inductance matrix model are in fairly good agreement with those obtained by the FEM. Therefore, the inductance matrix model can consider the current- and position-dependence of a motor with the same accuracy as the flux linkage model.

Figure 4 shows torque waveform at I_{rms} = 4.4 A, β = 20 deg and N = 1,500 min^{-1}. The average torque of all the behavioral models is in good agreement with that obtained from the FEM. However, torque ripple obtained from the FEM cannot be reproduced in all the behavioral models. This is because fluctuation of magnetic energy is not taken into account in them. Using the output power p_{out}, the instantaneous torque τ is expressed as

$$\tau = \frac{p_{out}}{\omega_{mech}} = \frac{p_{in} - p_{copper} - p_{mag}}{\omega_{mech}}, \quad (10)$$

where ω_{mech} is the mechanical angular frequency, p_{in} is input power, p_{copper} is copper loss, and p_{mag} is magnetic energy. In the case of the flux linkage model, p_{in} is expressed as (11).

$$p_{in} = i_d \upsilon_d + i_q \upsilon_q = p_{copper} + \left(i_d p\Psi_d + i_q p\Psi_q\right) + \omega\left(\Psi_d i_q - \Psi_q i_d\right) \quad (11)$$

By substituting (11) into (10), the following equation is obtained:

$$\tau = P_n \left\{ \left(\Psi_d i_q - \Psi_q i_d\right) + \frac{\left(i_d p\Psi_d + i_q p\Psi_q\right) - p_{mag}}{\omega} \right\} \quad (12)$$

Compared with (5), (12) takes fluctuation of magnetic energy into account. Therefore, by considering the fluctuation of magnetic energy directly in the behavioral models, it is expected that the numerical results by the FEM including torque ripple can be reproduced.

Figure 5 shows the effect of the fluctuation of magnetic energy calculated from the FEM on the torque waveform. It can be confirmed that torque ripple is expressed by considering magnetic energy. The phase difference of the torque waveform obtained from the FEM and the flux linkage model in (12) is caused by the time step size for the backward Euler method when solving (12). Because the energy based flux linkage model in (12) includes time-derivative term, which results in the numerical error, it is more practical to represent torque as a function of

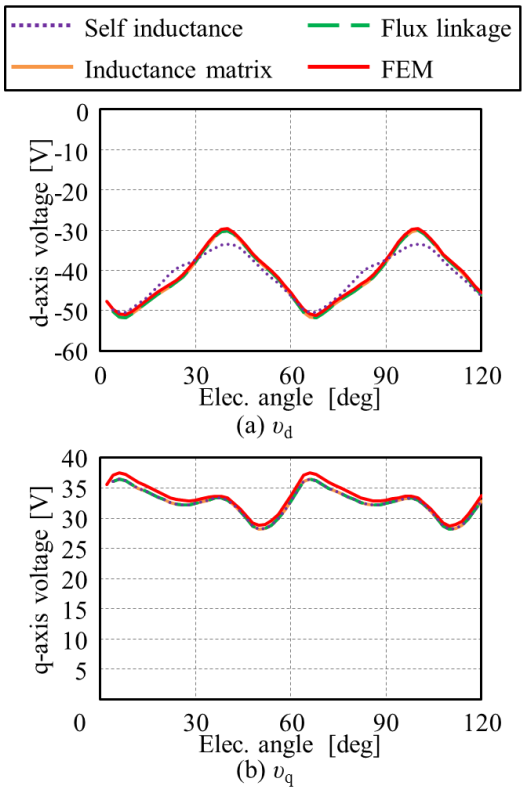

Figure 3 : Comparison of d- and q-axis voltages.

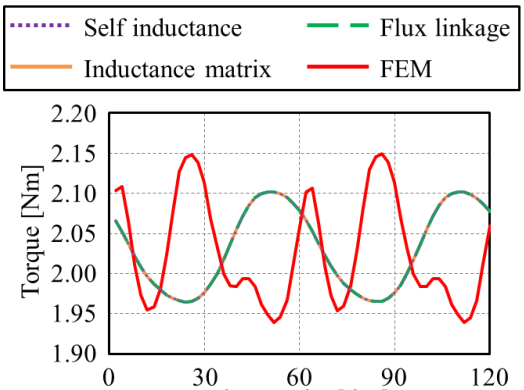

	Self inductance	Flux linkage	Inductance matrix	FEM
average torque [Nm]	2.0316	2.0316	2.0316	2.0270

Figure 4 : Comparison of torques.

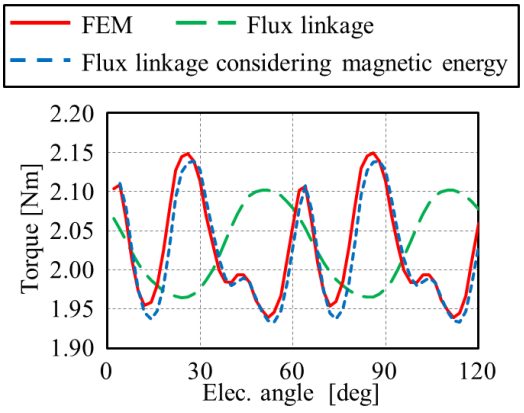

Figure 5 : Torque waveform considering magnetic energy.

current and position with the table data obtained from the FEM.

IV. Circuit Simulation Using Behavioral Model

When inputting voltage into a behavioral model, it is necessary to solve the nonlinear equation in which d- and q-axis currents are unknown variables. Here, a nonlinear analysis of behavioral models is carried out under sinusoidal voltage excitation. The table data of the inductance matrix model is calculated by using the results of 121 cases with 1 A pitch ($-10 \le i_d \le 0$, $0 \le i_q \le 10$) and 180 steps per period (electrical angle $\theta = 2$ deg per step). A linear interpolation is used for the table data. The calculation time required for performing 121 analyses is about 8 h 10 min in the inductance matrix model. Because of the periodicity of the analyzed motor shown in Figure 2, the magnetic field analysis for 1 / 3 period is required to reproduce numerical results for one period in the D1 model. The calculation time required for making the table data for 1 / 3 period is about 1 h 30 min in the flux linkage model and about 2 h 50 min in the inductance matrix model.

Figure 6 shows the time variation of d- and q-axis currents and torque when three-phase sinusoidal voltages corresponding to I_{rms} = 4.4 A and β = 20 deg are applied to the flux linkage model and the inductance matrix model of D1 model at N = 1,500 min^{-1}. In each model, three dimensional table data of inductances and flux linkages, which are functions of (i_d, i_q, θ), are used to consider their current- and position-dependence. Furthermore, the table data of torque considering current- and position-dependence is used to express torque ripple. From Figure 6, the results obtained from the inductance matrix model agree well with those obtained from the flux linkage model. Furthermore, the torque ripple by the FEM can be expressed accurately in each model.

Next, the influence of the pitch size of currents on the accuracy of the table data for inductances and flux linkages is investigated to reduce the computational cost required for creating table data. Figure 7 shows the analysis results when the pitch size of currents is set to 1A, 2A and 5A. As the pitch size of the d- and q-axis currents increases, the calculation accuracy simply reduces. However, the numerical results at the pitch size of 1 A and 2 A are not significantly different. Figure 8

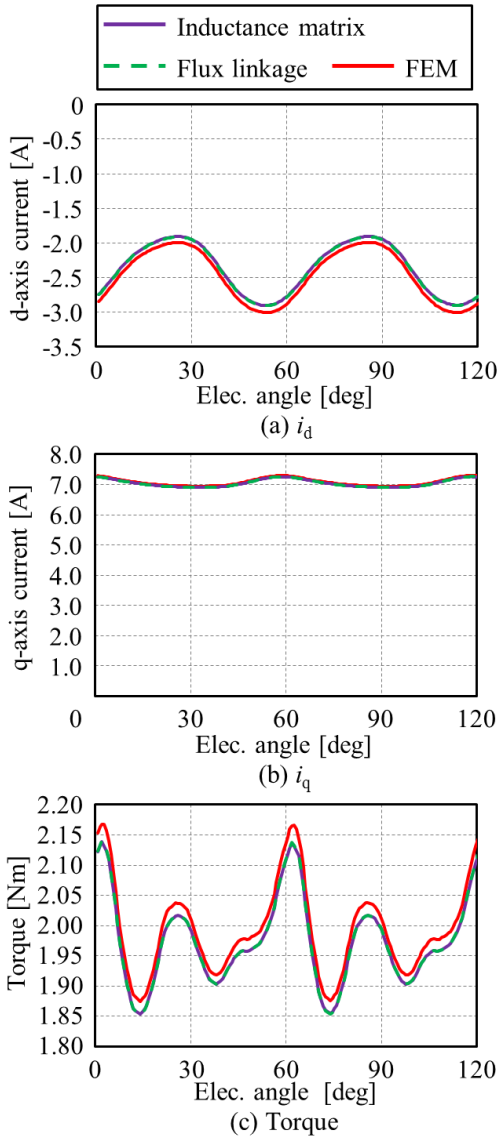

Figure 6 : Analysis results (voltage source).

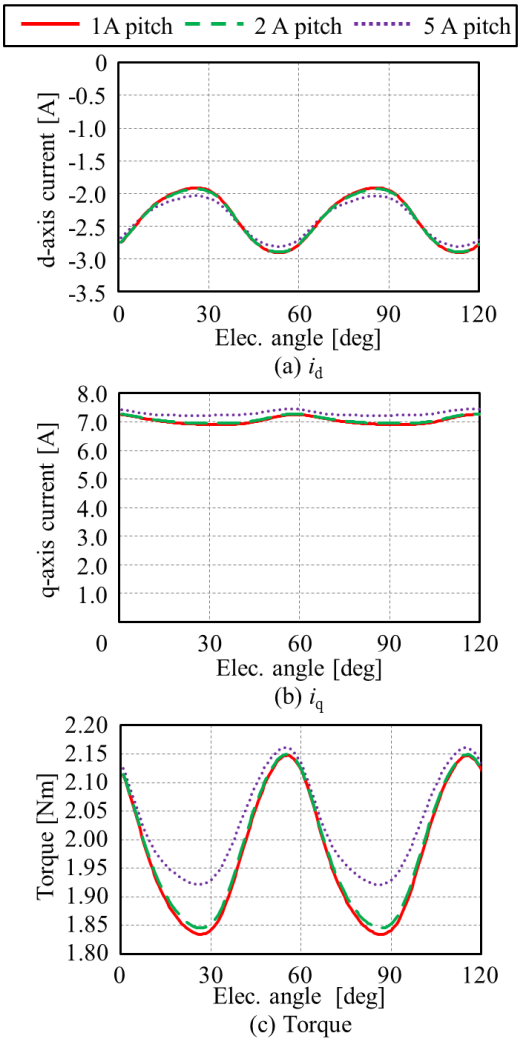

Figure 7 : Effect of pitch size of d- and q- axis currents.

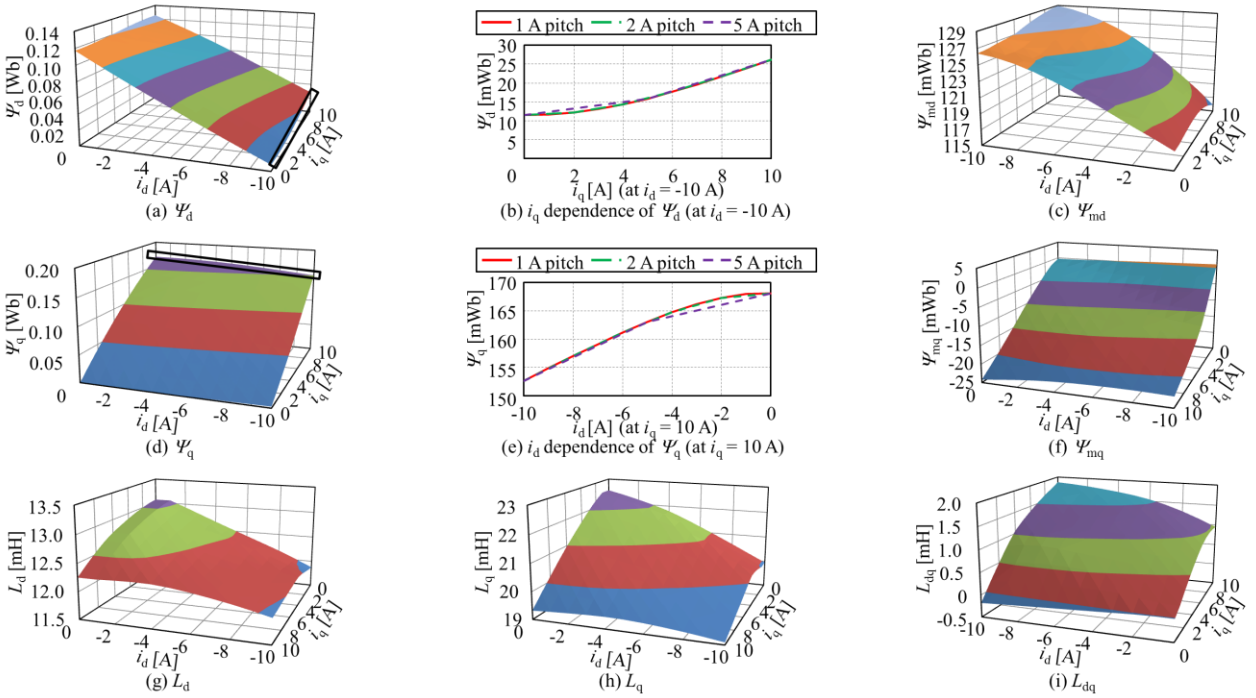

Figure 8 : Current-dependence of each table data.

shows Ψ_d, Ψ_q, Ψ_{md}, Ψ_{md}, L_d, L_q, and L_{dq} for i_d and i_q at θ = 2 deg. As an example, Figure 8 (b) and (e) show the q-axis current characteristics of Ψ_d at i_d = -10 A and the d-axis current characteristics of Ψ_q at i_q = 10 A. Because the shape of each data does not exhibit complicated variation, there is a possibility that the calculation time for creating table data can be shortened by reducing the number of analysis cases. By improving an interpolation method of the table data, the calculation time can be further reduced.

V. Coupled Circuit Simulation with Control System

Circuit simulation combined with control system is carried out by using Simulink. Figures 9 and 10 show the simulation circuit and the block diagram of the motor model described in Chapter IV, respectively. In the motor model, each table data is input to the S-function block and the nonlinear equation in (6) is solved. Furthermore, the torque is interpolated using i_d and i_q output by the S-function block. i_d = 0 control is used as the current vector control method. The rotation speed N is given as the reference and i_d, i_q and ω_m are fed back to perform current control and speed control. L_d, L_q and Ψ_m used for current control are obtained by averaging the values calculated by the FEM for one period under the condition of I_{rms} = 4.4 A and β = 20 deg. DC voltage V_{dc} for the inverter is 200 V, carrier frequency f_c is 5 kHz and dead time T_D is 3 μs. Dead time compensation is carried out to correct the dead time error occurring between the voltage reference and the actual output voltage.

Figure 11 shows simulation results of the simple motor model in which L_d, L_q and Ψ_m are used as constants and the behavioral model in which the inductance matrix model described in Chapter IV when the reference of N = 1,500 min^{-1} are given. It can be confirmed that the results

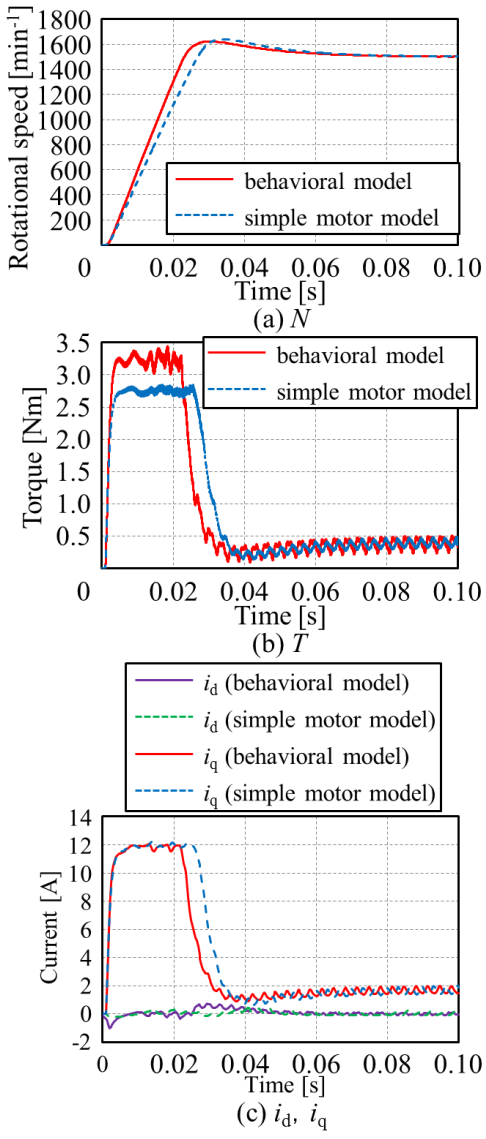

Figure 11 : Results of circuit simulation.

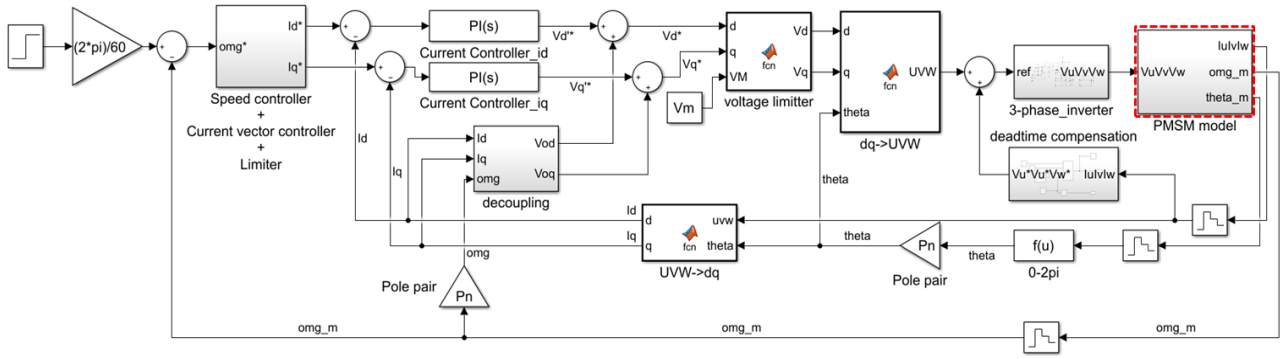

Figure 9 : Simulation circuit.

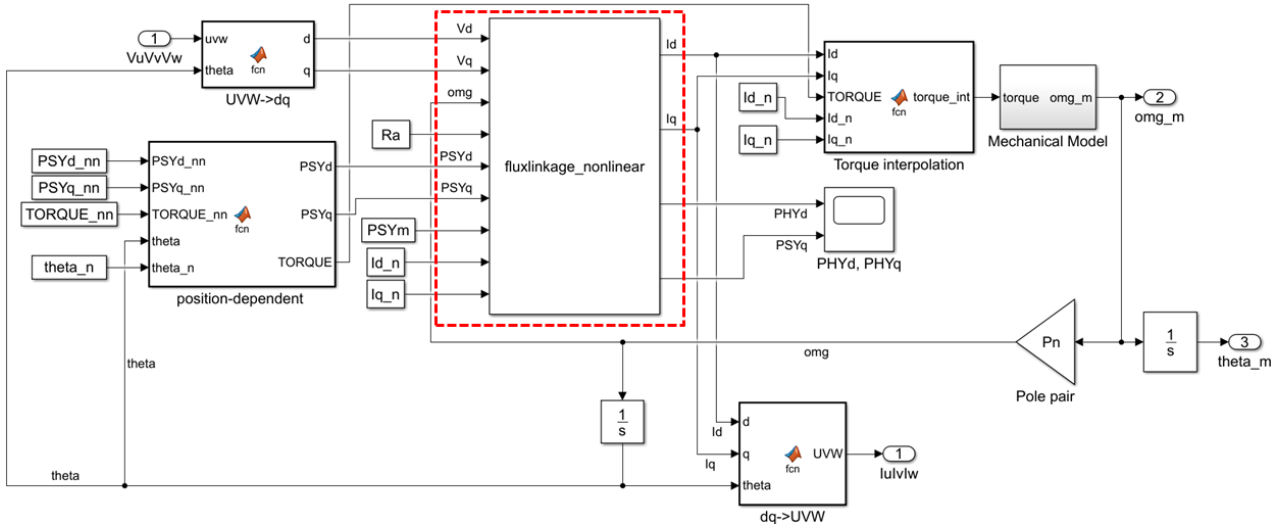

Figure 10 : Block diagram of motor model

of the behavioral model are significantly different from the results of the simple motor model. The convergence time of the behavioral model is shorter than that of the simple motor model and can express the torque ripple accurately, which indicates the effectiveness of the developed motor model.

VI. Conclusion

This paper investigated the new motor model "inductance matrix model" which utilizes the separation of flux linkage due to armature current and permanent magnets by the FPM. The inductance matrix model can consider the current- and position-dependence of parameters in the d-q equivalent circuit of an IPMSM with the same accuracy as the flux linkage model and calculate inductances explicitly. It is possible to carry out circuit simulation considering the effects of magnetic saturation and spatial harmonics by using the proposed motor model. In future work, we will compare simulated and measured results of the IPMSM and investigate a behavioral model which can take frequency-dependence of iron loss into account.

Acknowledgments

We would like to thank Mr. Takuya Yoshioka, DENSO Corporation, and Mr. Hiroyuki Kaimori, Science Solutions International Laboratory, Inc. for their valuable advice for this research.

References

[1] K. Akatsu and R. D. Lorenz, "Comparing Coupled Analysis with Experimental Results for an Interior PM Machine", *IEEE Trans. Ind. Applicat.*, Vol.45, no. 1, pp. 178-185 (2009)

[2] H. Kaimori and K. Akatsu, "Behavior Modeling of Permanent Magnet Synchronous Motors Using Flux Linkages for Coupling with Circuit Simulation," *IEEJ Journal of Industry Applications*, vol. 7, no. 1, pp. 56-63 (2018).

[3] J. A. Walker, D. G. Dorrell, and C. Cossar, "Flux-linkage Calculation in Permanent-magnet Motors Using the Frozen Permeabilities Method," *IEEE Trans. Magn.*, vol. 41, no. 10, pp. 3946-3948 (2005).

[4] W. Q. Chu and Z. Q. Zhu, "Average Torque Separation in Permanent Magnet Synchronous Machines Using Frozen Permeability," *IEEE Trans. Magn.*, vol. 49, no. 3, pp. 1202-1210 (2013).

[5] K. Yamazaki and M. Kumagai, "Torque Analysis of Interior Permanent-Magnet Synchronous Motors by Considering Cross-Magnetization: Variation in Torque Components With Permanent-Magnet Configurations," *IEEE Trans. Ind. Electron.*, vol. 61, no. 7, pp. 3192-3201 (2014).

[6] Investigating R&D Committee on Practical Analysis Techniques of 3-D Electromagnetic Field for Rotating Machines, "Practical Analysis Techniques of 3-D Electromagnetic Field for Rotating Machines", *IEEJ Tech. Rep.*, no.1296 (2013).

Comparison of Different Soil Models for the Dimensioning of Grounding Systems

Marko Jesenik, Miloš Beković, Anton Hamler and Mladen Trlep
Faculty of Electrical Engineering and Computer Science, Koroška cesta 46, 2000 Maribor, Slovenia

***Abstract*— Grounding systems are an important part of protection systems which protect people and devices. The Finite Element Method (FEM) is often used for proper dimensioning of the grounding systems. Soil parameters can be determined using analytic soil models. The determination of the soil models' parameters is an optimization problem. First of all, an appropriate soil model should be used, and different methods for the parameters` determination are variously successive and effective. A suggestion which model should be used and which method is appropriate for parameters` determination could be useful for grounding system designers.**

***Index Terms*—Grounding systems, Finite Element Method**

I. INTRODUCTION

Grounding systems are an important part of protection systems which protect people and devices. Modelling of a grounding system with the use of the Finite Element Method (FEM) [1, 2] model is a common approach which offers accurate grounding system design. A FEM model can be made only if the structure of the soil is known. Often soil characteristics are determined using measurements such as the Wenner method [3, 4], and analytical horizontal soil models. In the case of horizontal soil models, a real soil structure is replaced with one or more soil layers defined with resistivity and layer thickness. More or less matching of the used model with a real soil structure depends on the chosen number of soil layers and determination of the soil model's layers` parameters, which is an optimization problem. In our work, we tested a two layered integral and simplified model and three layered integral model using Genetic Algorithm [5], Differential Evolution [6], Artificial Bee Colony [7] and Teaching Learning Based Optimization [8] for three test examples, with the aim to determine the most appropriate model and method among those tested.

In the literature different works can be found which present soil parameters' determination. In [9] the Steepest descent method, Levenberg-Marquardt method, Newton method, Generalized Inverse method and Quasi-Newton method are mentioned. A Second order gradient technique, the usage of Electrostatic Images, and the Complex Image Method are presented in [10 - 12]. Genetic algorithm is used in [13, 14] and Differential Evolution is used in [6].

The remainder of this paper is organised as follows. In the second Section measurements and selected test examples are presented, and compared soil models are presented in the third Section. The Soil parameters` searching procedure and objective function are presented in the fourth Section, and used metaheuristics and parameters are presented in the fifth Section. The longest is the sixth Section, presenting results. The seventh Section presents our conclusions.

II. MEASUREMENTS AND TEST EXAMPLES

Determination of a soil model's parameters can be carried out using different measuring methods, but the Wenner method [3, 4] with four electrodes is the one used most commonly. It is determined with Standards IEEE 81-1983 and IEEE 81-2012 [15, 16]. Four electrodes are grounded into the depth *b* and placed at distance *d*, as presented in Fig. 1. A forced current between the outer electrodes causes electric voltage between the inner electrodes.

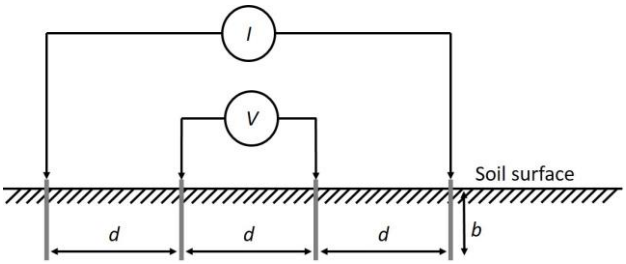

Figure 1: Wenner four electrode method

Apparent resistance can be calculated using (1).

$$\rho = \frac{4 \cdot \pi \cdot d \cdot R}{1 + \frac{2 \cdot d}{\sqrt{d^2 + 4 \cdot b^2}} - \frac{d}{\sqrt{d^2 + b^2}}}; R = \frac{U}{I} \tag{1}$$

Measurements are made for different distances *d*, and apparent resistance is obtained. dependent on *d*.

Three different test examples are used to test models and methods. The first one, marked as TEA, is a measurement in which apparent resistivity increased with *d*, the second one, marked as TEB, is taken from the literature [17], and also the third one, marked as TEC, is taken from the literature [18]. Test examples are presented in Fig. 2.

Data of the test examples presented in Fig. 2 are written in Tables I to III.

TABLE I
TEST EXAMPLE TEA

d (m)	4	5	6	7	8
ρ (Ωm)	75.24	79.55	85.91	94.45	105.64
d (m)	9	10	11	12	13
ρ (Ωm)	115.68	123.82	136.42	145.43	154.30
d (m)	14	15			
ρ (Ωm)	161.05	167.20			

TABLE II
TEST EXAMPLE TEB

d (m)	1	3	5	10	15
ρ (Ωm)	214	256	273	307	284
d (m)	20	30	50	80	
ρ (Ωm)	250	225	210	186	

TABLE III
TEST EXAMPLE TEC

d (m)	1.5	2	2.5	3	3.5
ρ (Ωm)	30.2	29.7	30.0	29.0	28.9
d (m)	4	4.5	5	5.5	6
ρ (Ωm)	28.8	28.8	27.6	27.4	28.2
d (m)	8	10	13	16	20
ρ (Ωm)	27.0	24.0	18.9	17.5	13.0
d (m)	25	32	40		
ρ (Ωm)	10.0	7.8	7.1		

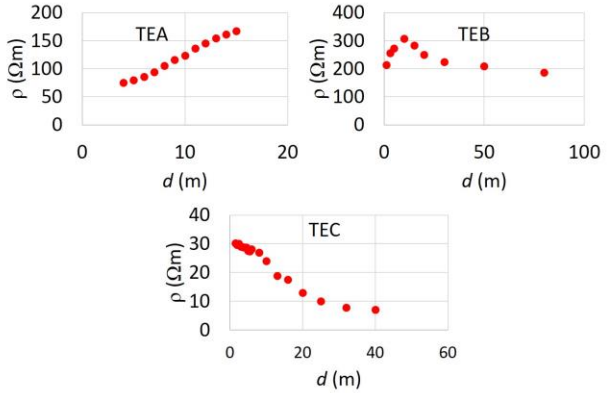

Figure 2: Test examples

III. COMPARED SOIL MODELS

Our choice was limited to three models, which are a two layers integral model (I2) [12], a simplified two layers model (S2) [19] and a three layers integral model (I3) [12]. The parameters of the two and three layers models are presented in Fig. 3.

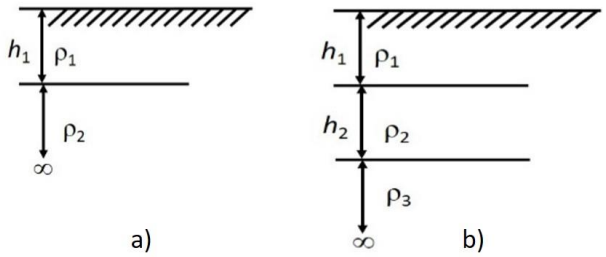

Figure 3: a) Parameters of two layers model, b) Parameters of three layers model

A. Two layers integral model

The two layers integral soil model has three parameters, which are, specific resistivity of the first layer ρ_1, width of the first layer h_1, and specific resistivity of the second layer ρ_2. Calculation of apparent resistivity is defined with (2) [12].

$$K_1(\lambda)=\frac{\rho_2-\rho_1}{\rho_2+\rho_1};\ \alpha_1(\lambda)=1+\frac{2K_1e^{-2\lambda h_1}}{1-K_1e^{-2\lambda h_1}};\ f(\lambda)=\alpha_1(\lambda)-1; \quad (2)$$
$$\rho=\rho_1\left(1+2d\int_0^\infty f(\lambda)\left[\mathrm{J}_0(\lambda d)-\mathrm{J}_0(2\lambda d)\right]d\lambda\right)$$

B. Three layers integral model

The three layers integral soil model has five parameters, which are, specific resistivity of the first layer ρ_1, width of the first layer h_1, specific resistivity of the second layer ρ_2, width of the second layer h_2 and specific resistivity of the third layer ρ_3. Calculation of apparent resistivity is defined with (3) [12].

$$K_2(\lambda)=\frac{\rho_3-\rho_2}{\rho_3+\rho_2};\ \alpha_2(\lambda)=1+\frac{2K_2e^{-2\lambda h_2}}{1-K_2e^{-2\lambda h_2}};$$
$$K_1(\lambda)=\frac{\rho_2\alpha_2(\lambda)-\rho_1}{\rho_2\alpha_2(\lambda)+\rho_1};\ \alpha_1(\lambda)=1+\frac{2K_1e^{-2\lambda h_1}}{1-K_1e^{-2\lambda h_1}}; \quad (3)$$
$$f(\lambda)=\alpha_1(\lambda)-1;$$
$$\rho=\rho_1\left(1+2d\int_0^\infty f(\lambda)\left[\mathrm{J}_0(\lambda d)-\mathrm{J}_0(2\lambda d)\right]d\lambda\right)$$

C. Two layers simplified model

The two layers simplified model is the simplification of the I2 model and it has the same parameters ρ_1, h_1 and ρ_2. Apparent resistivity is calculated using (4) [19].

$$k=\frac{\rho_2-\rho_1}{\rho_2+\rho_1};\ A=1+\left(\frac{2mh_1}{d}\right);\ B=A+3; \quad (4)$$
$$\rho=\rho_1\left(1+4\sum_{m=1}^{\infty}k^m\left(\frac{1}{\sqrt{A}}-\frac{1}{\sqrt{B}}\right)\right)$$

IV. SOIL PARAMETERS` SEARCHING PROCEDURE AND OBJECTIVE FUNCTION

Different optimization methods could be used for the calculation. We decided to use metaheuristic methods, and a basic flowchart is shown in Fig. 4, where objective function is marked with OF.

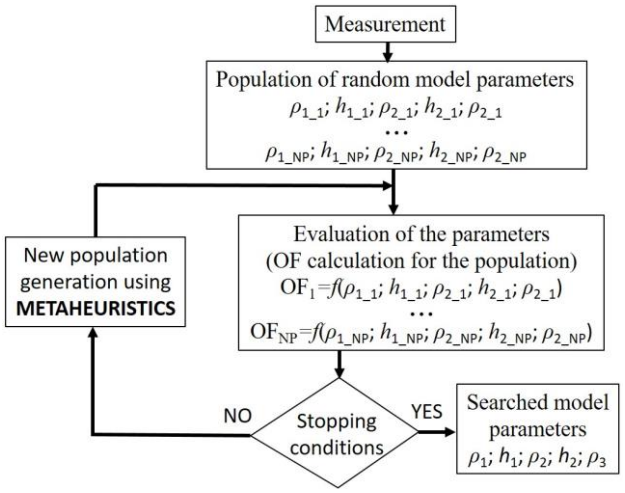

Figure 4: Flowchart of the calculation procedure

Objective function is defined the same as is used in literature [13, 17, 19] and it is written in (5).

$$\mathrm{OF} = \frac{1}{n}\sum_{i=1}^{n}\left|\frac{\rho_{\mathrm{calculated\_i}} - \rho_{\mathrm{measured\_i}}}{\rho_{\mathrm{measured\_i}}}\right| \cdot 100 \ (\%) \qquad (5)$$

n is the number of measured points. The difference between calculated and measured apparent resistivity for each point should be as small as possible.

V. USED METAHEURISTICS AND PARAMETERS

We decided to test four different metaheuristics to solve the presented problem. The older Genetic Algorithm (GA) [5] was the first choice. The second choice was Differential Evolution (DE) [6] with strategy DE/rand/1/exp. The third and fourth choices were newer Artificial Bee Colony (ABC) [7] and Teaching Learning Based Optimization (TLBO) [8].

A. Parameters` limits

Parameters` limits are set considering the physical background of the problem. The soil specific resistivity was set between 5 Ωm, which is the specific resistivity of wet sand, and 3500 Ωm, which is the specific resistivity of rocky ground. The thickness of the soil layers is set between 0.4 m and 40 m. It doesn't make sense to set more than 40 m, because the field made by grounding system penetrates only to a limited depth of the soil.

B. Parameters used for the calculation

The internal parameters of GA are set on the following values: fraction of the population kept equals 0.5 and mutation rate equals 0.1. The internal parameters of DE were set on following values: Crossover probability rate equalled 0.8 and amplification of differential variation equalled 0.6. The used DE strategy was rand/1/bin. Limit value of ABC was set on 100.

Population was set to six times the number of parameters. Stopping criteria was the number of Fitness Evaluations (FEs), which was set to 20,790. Based on the experimental test, it was found out that 20,790 FEs is enough to get results. In the case of TLBO, implementation is used, with no duplicate elimination phase. Two phases were considered for Fes` counting, teaching and learning phases. For ABC, dynamic counting was used, due to the consideration of the scout bee. In Tables IV and V calculation parameters are presented for I2, S2 and I3 models separately.

TABLE IV
PARAMETERS USED FOR THE CALCULATION IN THE CASE OF I2 AND S2 MODELS

	GA, DE	ABC	TLBO
Parameters (P)	3	3	3
Population (NP)	6 x P=18	6 x P=18	6 x P=18
Iterations (IT)	1155	≤ 1155	577
Used FEs	NP x IT 20790	NP x IT ≤ 20790	NP x 2 x IT 20772

TABLE V
PARAMETERS USED FOR THE CALCULATION IN THE CASE OF THE I3 MODEL

	GA, DE	ABC	TLBO
Parameters (P)	5	5	5
Population (NP)	6 x P=30	6 x P=30	6 x P=30
Iterations (IT)	693	≤ 693	346
Used FEs	NP x IT 20790	NP x IT ≤ 20790	NP x 2 x IT 20772

In the case of TLBO, 20,772 FEs are used, because 20,790 can't be divided with 2x18=36 and with 2x30=60.

VI. RESULTS

Because of the stochastic nature of the metaheuristics, 100 independent runs were made for each combination of model (I2, S2 and I3), test example (TEA, TEB and TEC) and solving method (GA, DE, ABC and TLBO). Results are presented separately for different models. In each Table, the presented results are the best value (B), the worst value (W), mean value (M) and Standard Deviation (SD).

A. Results considering the I2 model

Tables VI, VII and VIII show results for the I2 model for TEA, TEB and TEC test examples.

TABLE VI
RESULTS FOR THE I2 MODEL AND TEA TEST EXAMPLE

	GA	DE	ABC	TLBO
B	1.226508	1.209603	1.237953	1.209603
W	7.931337	3.242333	1.621673	1.209603
M	3.649783	1.411282	1.478415	**1.209603**
SD	2.021628	$5.922\cdot10^{-1}$	$1.218\cdot10^{-1}$	$3.308\cdot10^{-8}$

TABLE VII
RESULTS FOR THE I2 MODEL AND TEB TEST EXAMPLE

	GA	DE	ABC	TLBO
B	6.568881	6.567178	6.567178	6.567178
W	6.824377	12.26323	6.795761	6.567178
M	6.638972	6.681099	6.579248	**6.567178**
SD	$6.018\cdot10^{-2}$	$7.974\cdot10^{-1}$	$2.801\cdot10^{-2}$	$1.78\cdot10^{-15}$

TABLE VIII
RESULTS FOR THE I2 MODEL AND TEC TEST EXAMPLE

	GA	DE	ABC	TLBO
B	2.235074	2.217447	2.217535	2.217447
W	10.74522	68.37207	2.310524	2.217447
M	4.249090	21.66717	2.231368	**2.217447**
SD	2.159253	25.72826	$1.806\cdot10^{-2}$	$2.22\cdot10^{-15}$

B. Results considering the S2 model

Tables IX, X and XI show results for the S2 model for TEA, TEB and TEC test examples.

TABLE IX
RESULTS FOR THE S2 MODEL AND TEA TEST EXAMPLE

	GA	DE	ABC	TLBO
B	1.218375	1.209748	1.251499	1.209748
W	7.438757	3.242375	1.627220	1.209749
M	3.059937	1.672754	1.552497	**1.209748**
SD	1.840819	$8.410 \cdot 10^{-1}$	$1.096 \cdot 10^{-1}$	$1.154 \cdot 10^{-7}$

TABLE X
RESULTS FOR THE S2 MODEL AND TEB TEST EXAMPLE

	GA	DE	ABC	TLBO
B	6.571514	6.565999	6.565999	6.565999
W	6.821671	12.26359	6.710149	12.26360
M	6.635395	6.868355	6.576374	**6.679952**
SD	$5.764 \cdot 10^{-2}$	$8.144 \cdot 10^{-1}$	$2.182 \cdot 10^{-2}$	$7.977 \cdot 10^{-1}$

TABLE XI
RESULTS FOR THE S2 MODEL AND TEC TEST EXAMPLE

	GA	DE	ABC	TLBO
B	2.235861	2.218367	2.218463	2.218367
W	10.74256	69.18751	2.293418	2.218367
M	4.262519	23.67661	2.225346	**2.218367**
SD	2.062856	25.63474	$1.082 \cdot 10^{-2}$	$5.78 \cdot 10^{-15}$

C. *Results considering the I3 model*

Tables XII, XIII and XIV show results for the I3 model for TEA, TEB and TEC test examples.

TABLE XII
RESULTS FOR THE I3 MODEL AND TEA TEST EXAMPLE

	GA	DE	ABC	TLBO
B	1.127531	1.096902	0.900667	1.096902
W	7.634448	3.221506	2.243543	1.152148
M	2.698900	1.239976	1.355032	**1.102003**
SD	1.761500	$5.147 \cdot 10^{-1}$	$2.5085 \cdot 10^{-1}$	$6.749 \cdot 10^{-3}$

TABLE XIII
RESULTS FOR THE I3 MODEL AND TEB TEST EXAMPLE

	GA	DE	ABC	TLBO
B	2.304934	1.931828	2.002967	1.924942
W	7.039856	8.428094	4.252339	6.614352
M	5.619087	5.094612	**2.602374**	5.575045
SD	1.461553	2.005376	$4.459 \cdot 10^{-1}$	1.816522

TABLE XIV
RESULTS FOR THE I3 MODEL AND TEC TEST EXAMPLE

	GA	DE	ABC	TLBO
B	2.147235	1.996786	1.997091	1.996786
W	16.48269	46.83763	2.168586	2.251057
M	5.151856	6.965966	**2.003597**	2.014430
SD	3.046025	11.58809	$1.865 \cdot 10^{-2}$	$6.023 \cdot 10^{-2}$

D. *Comparison of the models*

Comparing results from Tables VI and IX, presenting results for the I2 and S2 models for the TEA test example, it can be seen that the results are almost identical. The same can be seen from comparing Tables VII and X, presenting results for the I2 and S2 models for the TEB test example, and also from comparing Tables VIII and XI, presenting results for the I2 and S2 models for the TEC test example. Because of this, only results using the I2 model will be presented in the continuation of the paper.

Figure 5 shows measured and calculated apparent resistivity for TEA.

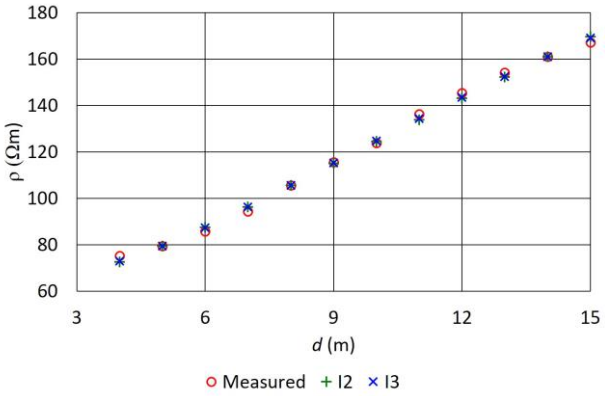

Figure 5: Measured and calculated apparent resistivity for TEA

From Fig. 5 it can be seen that calculated values for both models, I2 and I3, coincide well with the measured values. The difference between results obtained using the I2 model is small compared to the I3 model. The best mean objective function for the I2 model is 1.209603, and for I3 is 1.102003, which is only a bit better.

Figure 6 shows measured and calculated apparent resistivity for TEB.

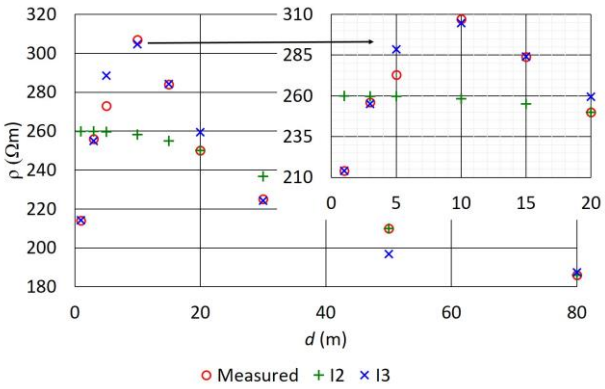

Figure 6: Measured and calculated apparent resistivity for TEB

From Figure 6 it can be seen that calculated values using the I2 model don't coincide well with measured values, which can be seen in the part where the measured values increase and, after that, decrease. Also, the best mean value of the objective function using the I2 model is 6.567178, which is a rather large value. Results are much better using the I3 model, for which the best mean value is 2.602374, which can also be seen from Fig. 6, where calculated values for the I3 model coincide well with measured values. The I2 model didn't give satisfactory

results.

Figure 7 shows measured and calculated apparent resistivity for TEC.

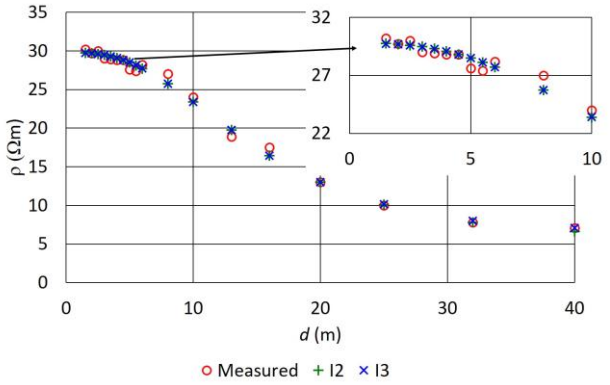

Figure 7: Measured and calculated apparent resistivity for TEC

From Fig. 7 it can be seen that, also for this case, such as for TEA, calculated values for the I2 and for I3 models coincide well with measured values. The best mean objective function for the I2 model is 2.217447, and the best mean objective function for the I3 model is 2.003597, which is only a bit better value.

E. Calculation times

Calculation times of the Objective Function depend on the parameters. Calculation of the apparent resistivity using (3), in the case of integral models, is made using numerical integration. Integration is finished when the value inside the integral is small enough and no longer affects the result. Calculation of apparent resistivity using (4), in the case of the simplified two layers model, is finished when the value inside the sum is small enough and no longer affects the result.

Because of this, the calculation times for separate runs can be very different. Calculation times are also different for different solving methods, because they depend on the searching area of the individual method.

Comparison of the calculation times is made on a computer with a 2.67 GHz processor. For each combination of model, method and test example, 30 independent runs were made. Figures 8, 9 and 10 show the calculation times used for the S2, I2 and I3 models separately.

From Figs. 8, 9 and 10 it can be seen that the number of measured points of the data influence calculation time. The longest is for the TEC example with 18 points, and the shortest is for the TEB example with 9 points.

The S2 model is very fast, almost all calculations were made in less than minute, and mean calculation times were from 5 to 30 seconds.

The time used for the I2 model is much longer. Mean calculation times were from 150 to 2500 seconds.

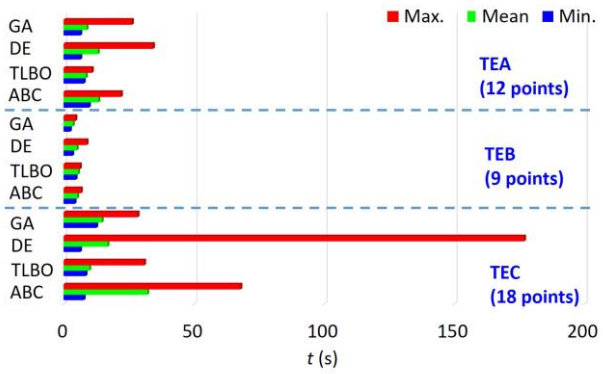

Figure 8: Calculation times of the S2 model

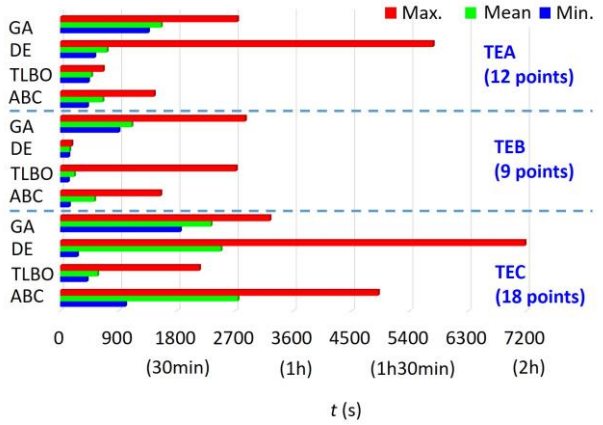

Figure 9: Calculation times of the I2 model

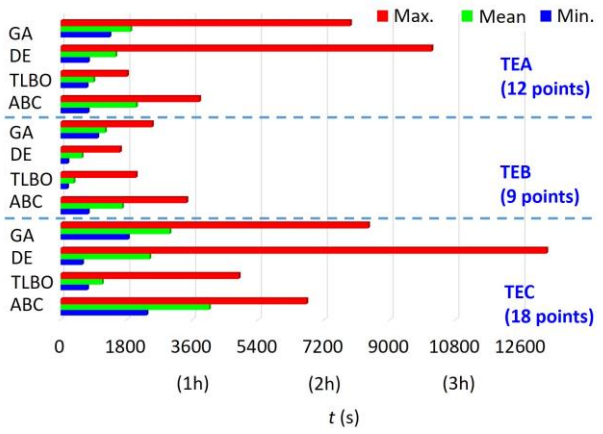

Figure 10: Calculation times of the I3 model

The times used for the I3 model are even longer. Mean calculation times were from 350 to 4000 seconds.

It can be seen that different models and different examples cause that, in some cases, some methods are faster, and in different cases other methods are faster. It can generally be seen that the mean calculation time of TLBO was the shortest in many cases.

VII. CONCLUSIONS

Comparing results obtained with the S2 and I2 models, it can be concluded that results are very similar. The S2 model is a very good simplification of the I2 model, and the calculation times of the S2 model are much shorter

than the calculation times of the I2 model. If the selection is made only between the S2 and I2 models, the S2 model would be a better choice.

However, results for TEB using the two layers model are not appropriate, which can be seen from Fig. 6. Based on that, the two layers model can't be suggested as a universal model. Much better are the results obtained using the three layered model, which means that the three layered model can be suggested as a universal model.

However, all solving methods are not appropriate for solving the presented problem. In the case of TEB, only ABC was able to solve the problem. Although TLBO is faster and in more cases the mean value of the Objective Function is lower than in the case of ABC, ABC is suggested as a universal method for the presented problem, because of the TLBO's problems with TEB and the I3 model.

ACKNOWLEDGMENT

This work was supported by the Slovenian Research Agency under Grant P2-0114.

REFERENCES

[1] Z. Zeng, L. Udpa, S.S. Udpa, Finite-element model for simulation of ferrite-core eddy-current probe, IEEE Transactions on Magnetics, 46 (3), (2010), 905-909

[2] M. Trlep, A. Hamler, M. Jesenik, B. Štumberger, The FEM-BEM analysis of Complex Grounding systems, IEEE Transactions on Magnetics, 39 (3) (2003), 1155-1158

[3] Z. Chik, T. Islam, Near Surface Soil Characterizations Through Soil Apparent Resistivity: a Case Study, The 7th International Conference on Intelligent Data Acquisition and Advanced Computing System: Technology and Applications, Berlin, Germany (2013) 57-60

[4] R.D. Southey, M. Siahrang, S. Fortin, F.P. Dawalibi, Using Fall-of-Potential Measurements to Improve Deep Soil Resistivity Estimates, IEEE Transactions on Industry Applications, 51 (6) (2015), 5023-5029

[5] R. L. Haupt, S. E. Haupt, Practical genetic algorithms, John Wiley and Sons, New Jersey, USA, 2004

[6] W.R. Pereira, M.G. Soares, L.M. Nato, Horizontal Multilayer Soil Parameter Estimation Through Differential Evolution, IEEE Transactions on Power Delivery, 31 (2) (2016), 622-629

[7] D. Karaboga, B. Basturk, A powerful and efficient algorithm for numerical function optimization: artificial bee colony (ABC) algorithm, Journal of Global Optimization, 39 (3) (2007), 459 – 471

[8] R.V. Rao, V.J. Savsani, D.P. Vakharia, Teaching-learning-based optimization: A novel method for constrained mechanical design optimization problems, Computer-Aided Design, 43 (2011), 303 – 315

[9] J.L. del Alamo, A Comparion among Eight Different Techniques to Achieve an Optimum Estimation of Electrical Grounding Parameters in Two-Layer Earth, IEEE Transactions on Power Delivery, 8 (4) (1993) 1890-1899

[10] J.L. del Alamo, A second Order Gradient Technique for an Improved Estimation of Soil Parameters in a Two-Layer Earth, IEEE Transactions on Power Delivery, 6 (3) (1991) 1166-1170

[11] P.J. Lagace, J. Fortin, E.D. Crainic, Interpretation of Resistivity Sounding Measurements in N-Layer Soil using Electrostatic Images, IEEE Transactions on Power Delivery, 11 (3) (1996) 1349-1354

[12] B. Zhang, X. Cui, L. Li, J. He, Parameter Estimation of Horizontal Multilayer Earth by Complex Image Method, IEEE Transactions on Power Delivery, 20 (2) (2005), 1394-1401

[13] W.P. Calixto, L.M. Neto, M. Wu, K. Yamanaka, E. Moreira, Parameters Estimation of Horizontal Multilayer Soil Using Genetic Algorithm, IEEE Trancactions on Power Delivery, 25 (3) (2010) 1250-1257

[14] N. Mohamed Nor, R. Rajab, K. Ramar, Validation of the Calculation and Measurement Techniques of Earth Resistance Values, American Journal of Applied Sciences 5 (10) (2008) 1313-1317

[15] IEEE Power and Energy Society, IEEE Guide for Measuring Earth Resistivity, Ground Impedance, and Earth Surface Potentials of Grounding Systems, The Institute of Electrical and Electronics Engineers, Inc., New York (2012)

[16] T. Barič, D. Šljivac, M. Stojkov, Validity limits of the expression for measuring soil resistivity by the Wenner method according to IEEE Standard 81-1983, Energija, 56 (3) (2007) 730-753

[17] H. Zhiqiang, Z. Bin, Soil Model's Inversion Calculation Base on Genetic Algorithm, 7th Asia-Pacific International Conference on Lightning, Chengdu, China (2011) 225-230

[18] P.J. Lagace, M.H. Vuong, Graphical User Interface for Interpreting and Validating Soil Resistivity Measurements, IEEE ISIE (International Symposium on Industrial Electronics, Montreal, Quebec, Canada (2006) 1841-1845

[19] I.F. Gonos, I.A. Stathopulos, Estimation of Multilayer Soil Parameters Using Genetic Algorithms, IEEE Transactions on Power Delivery, 20 (1) (2005) 100-106

Design Optimization of Conductor Plate in Magnetic Sensor for Enhancing Performance on Detection of Rail Wheel

[1]Hiroyuki Kuwahara, [1]Atsushi Ando, [1]Yuya Maruyama, [1]Shinji Wakao,
[2]Masahide Takahashi, [2]Makoto Yagi, [3]Tamio Okutani, and [4]Yoshifumi Okamoto
[1]Department of Electrical Engineering and Bioscience, Waseda University, Tokyo 1698555, Japan.
[2]The Nippon Signal Co., Saitama 3468524, Japan
[3]Railway Signalling Technical Research Institute Co., Tokyo 1530033, Japan
[4]Department of Electrical and Electronic Engineering, Hosei University, Tokyo 1848584, Japan
wakao@waseda.jp

***Abstract*—The axle counter is an important device which detects the wheel existence on a railway. In this paper, we propose the novel introduction of a conductor plate to an axle counter and optimize its configuration using level-set method for improving detection performance. Finally, we derive an easily feasible optimum shape of the conductor plate by the level-set method imposing an area limitation set by referencing the size of the design area.**

***Index Terms*—induced voltage, level-set method, magnetic sensor, multi-objective design optimization.**

I. INTRODUCTION

Recently, the trend of speedup of train intensifies on a worldwide scale. Therefore, the development of sensors for high-speed train is an important issue. In particular, the operating range of sensor, i.e., the range which the axle counter can detect a wheel, should be wider as the speed of train increases. With this background, this paper mainly focuses on the design optimization of magnetic sensor from the viewpoint of the operating range.

It is revealed that introducing a conductor plate can extend the operating range effectively [1]. In this paper, we propose new optimized conductor configurations using the 2-D level-set method. Finally, we derive an easily feasible 3-D shape of the conductor plate by modifying the optimization result. Some numerical examples, which demonstrate the validity and effectiveness of the proposed approach, are also presented.

II. IMPROVEMENT OF THE OPERATING RANGE OF THE SENSOR

Fig. 1 shows the model investigated in this paper. This model is composed of a wheel, a rail and an axle counter, which is a device including a transmission coil, a receiving coil and a newly introduced conductor plate. The Two coils have a ferrite core wound with copper wire. In the case without a wheel, the magnetic flux from the transmission coil passes over the rail and flows into a receiving coil from the top to the bottom. On the other hand, in the case where a wheel is next to an axle counter, the magnetic flux shielded off by the wheel passes between the wheel and the rail. Therefore, the flux flows into the receiving coil from the bottom to the top. The axle counter detects the wheel existence by the phase inversion of the induced voltage in the receiving coil changing with a passing train.

The conductor plate helps the flux flow into the receiving coil from the bottom to the top when the wheel is close to but not directly next to an axle counter. In other word, a conductor plate adequately varies the magnetic flux distribution for detection. Table I shows the specifications of the model. In addition, the current value of the transmission coil is 400 (mA) × 58(turns) and the frequency is 21 (kHz).

We succeed in extending the range which the axle counter can detect the wheel, i.e., the operating range, by using a conductor plate. Additionally, we optimize the shape of a conductor plate and the position of the receiving coil to further improve the operating range.

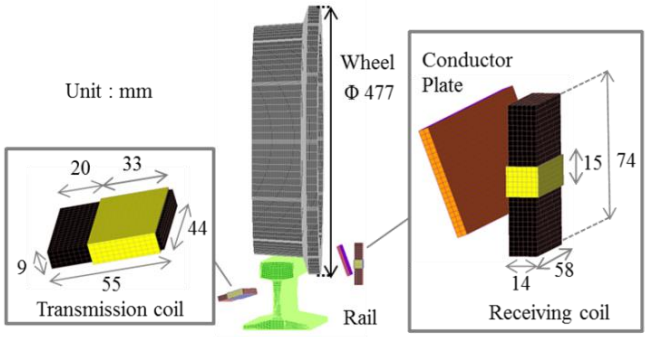

Fig. 1: Axle counter investigated in this paper

TABLE I
SPECIFICATIONS OF THE MODEL

	Relative permeability	Conductivity	Number of turns
Transmission coil with ferrite core	5000	0	58 turns
Receiving coil with ferrite core	5000	0	60 turns
Rail	70	4.56×10^6 S/m	-
Wheel	70	4.56×10^6 S/m	-

III. SHAPE OPTIMIZATION METHOD FOR THE CONDUCTOR PLATE

In conventional shape optimization the pre-set of the design variables makes the search domain of the solution narrow. Therefore, we use the level-set method to extend

the solution search domains and optimize the shape more dynamically. This is achieved by using the entire material boundary as a design variable which is calculated using the level-set function. It is the signed distance function which is given by (1), where Ω is the material area and $\partial\Omega$ is the material boundary. $d(x,\partial\boldsymbol{\Omega})$ shows the shortest distance from the material boundary.

We describe the material distribution in the range from 0 to 1 using Heaviside function (2). The parameter h defines the gray scale, which is neither the material nor the air. It is the transition width of gray scale, expressing the material constant as the continuous value. Fig. 2 shows concept of level-set function.

In this method, optimization is carried out by advection, which is determined by the gradient of sensitivity of the level-set function. Therefore, we can derive a practical and effective shape.

$$\phi(x) = \begin{cases} d(x,\partial\Omega) & (x \in \Omega) \\ 0 & (x \in \partial\Omega) \\ -d(x,\partial\Omega) & (x \notin \Omega) \end{cases} \quad (1)$$

$$H(\phi) = \begin{cases} 0 & (\phi < -h) \\ \frac{1}{2} + \frac{15}{16}\left(\frac{\phi}{h}\right) - \frac{5}{8}\left(\frac{\phi}{h}\right)^3 + \frac{3}{16}\left(\frac{\phi}{h}\right)^5 & (-h \le \phi < h) \\ 1 & (h \le \phi) \end{cases} \quad (2)$$

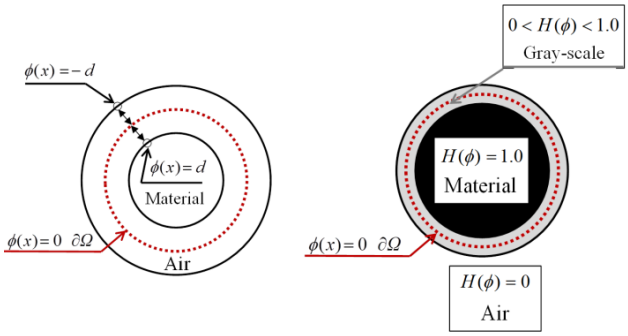

Fig. 2: Concept of level-set function

As it is also important to reduce the computational burden, we use 2-D FEM combined with level-set method to optimize the shape of the conductor plate and the position of the receiving coil. Subsequently, we define the 3-D optimum shape by referring to the 2-D optimum shape and the results of the 3-D FEM analysis.

IV. Design Variables And Objective Functions For Sensor Optimization

In this paper, we consider the position of the receiving coil and shape of the conductor plate as the design variables and consider two objective functions. One is the operating range, which is important to detect a high-speed train safely. The other is the amount of the induced voltage in the receiving coil when the axle counter detects the wheel in order to protect against noises from many devices around the rail.

Fig. 3 shows the model of the 2-D optimization problem. Design area shown in Fig. 3 means the area where we can set the conductor plate. According to the railway building regulations, we cannot set the conductor plate and receiving coil more than 25 mm above the rail and it must be within 76 mm from the rail. Therefore, we define the available area to set a plate and the receiving coil as shown in the area surrounded with dotted lines in Fig. 3.

We have two reasons why there is an air gap between the train and the wheel in our simulation. First in the 3-D model, the wheel contacts with the rail at only one point, therefore flux is able to pass over the rail. Thus, in the model of the 2-D optimization problem an airgap must be created to allow flux to pass over the rail. Second, since we consider the operating range as an objective function, the model should consider cases where the wheel is near but not next to the axle counter. In these cases the shielding effectiveness of a wheel is not effective enough to block the flow of flux over the rail, therefore the need for an airgap space between the rail and the wheel in the simulation.

This 2-D optimization problem considers the total amount of flux from the bottom to the top as an evaluation function, which enables us to optimize the two objective functions with only this evaluation function.

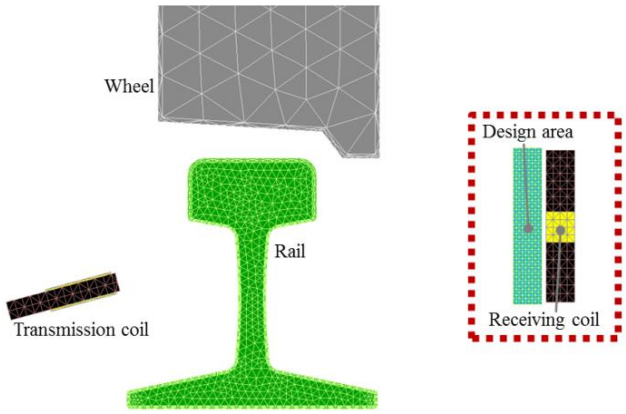

Fig. 3: Model of 2-D optimization problem

V. 2-D Optimization Results For The Conductor Plate

From the optimization we conclude the optimum shape as disconnected conductor plates. However, this type of conductor plate is not a feasible design. Therefore, we propose a method which imposes an area limitation to prevent the conductor plate from becoming smaller than a lower limit. This limit is appropriately set by referencing the size of the design area. This makes it possible to get a non-disconnected and easily manufactured feasible optimum shape. It also helps us to resolve the problem of the final shape of the optimization changing depending on the initial shape.

We optimize 2-D models with different sized design areas and where the design area and receiving coil location

are in different parts of the region surrounded by the dotted lines in Fig. 3. In this section, we show and compare the typical results. First, we show the optimum shape of the models changed based on the height of the receiving coil which is lowered by 40mm and 20mm from the building limit in Fig. 4 (a) and (b) respectively. Each optimum shape has the similar characteristic of the conductor plate length extending to the bottom of the receiving coil. TABLE II shows the final values of the evaluation function for the three models, and the values from high to low are: Fig. 4(c), Fig. 4(b), and Fig. 4(a). As a result, the case of Fig. 4(c) shows the highest value. Fig. 5 and Fig. 6 shows its initial shape of optimization and its increasing value of the evaluation function respectively. These results mean that the height of the receiving coil should be set as high as the railway building regulations allow.

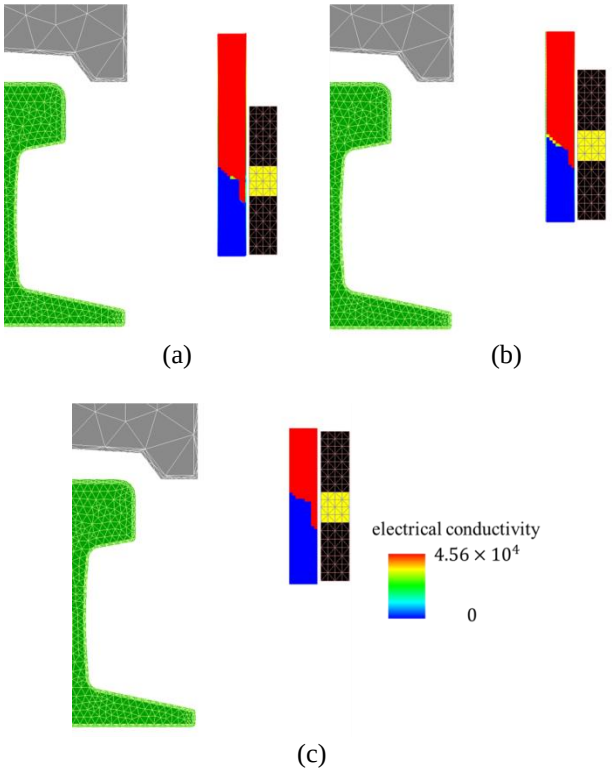

Fig. 4: Optimum shape of the conductor plate (a) lower than the limit by 40mm, (b)lower than the limit by 20mm, and (c)the model as high and close to rail as possible

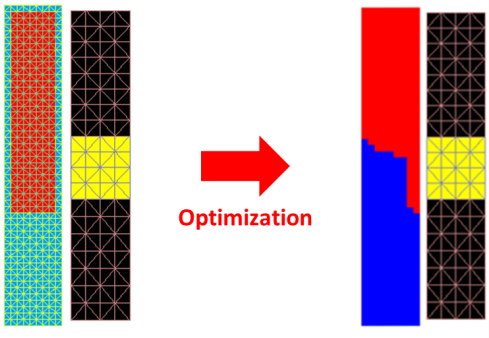

Fig. 5: The initial shape of optimization of Fig.4(c)

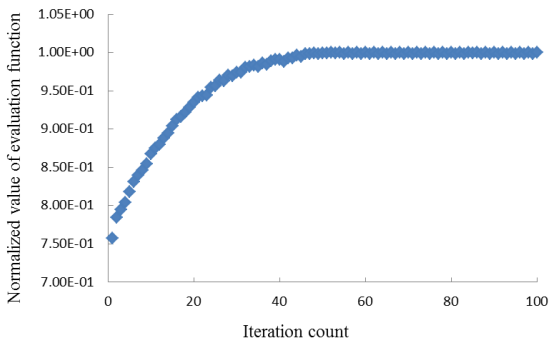

Fig. 6: The increasing value of the evaluation function of Fig. 4(c)

TABLE II
FINAL VALUE OF THE EVALUATION FUNCTION OF MODELS SHOWN IN FIG. 4

	Fig. 4(a)	Fig. 4(b)	Fig. 4(c)
Final value of the evaluation function	7.32×10^{-5}	7.73×10^{-5}	8.39×10^{-5}

Fig. 7 shows the optimum shape of the models changed based on the distance between the rail and the design area increased by 20mm and 40mm in Fig. 7(b) and (c) respectively. These optimum shapes also have the same similar characteristic seen in Fig. 4. TABLE III shows the final values of the evaluation function for the three models, and the values from high to low are: Fig. 7(c), Fig. 7(b), and Fig. 7(a). Therefore, we conclude that the optimum position of the conductor and the receiving coil is as high and close to the wheel as possible, and optimum conductor shape is shown in Fig. 4(c) (Fig. 7(a)).

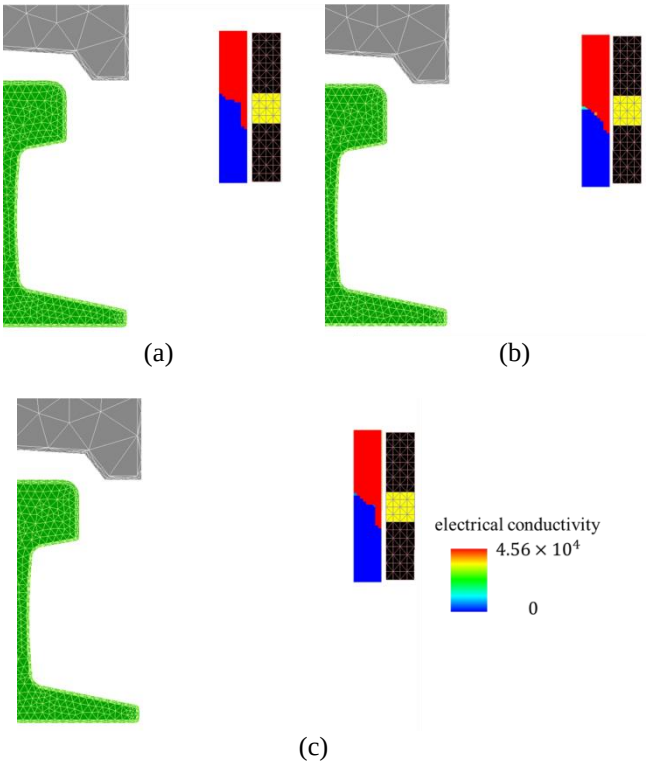

Fig. 7: Optimum shape of the conductor plate (a) the model as high and close to rail as possible (b)farther from the rail limit by 20mm and (c) farther from the rail limit by 40mm.

TABLE III

FINAL VALUE OF THE EVALUATION FUNCTION OF MODELS SHOWN IN FIG. 7

	Fig. 7(a)	Fig. 7(b)	Fig. 7(c)
Final value of the evaluation function	8.39×10^{-5}	5.98×10^{-5}	3.78×10^{-5}

VI. CONSIDERATION FOR 3-D OPTIMUM SHAPE

We analyze different 3-D models, based on the 2-D optimum shape, by 3-D FEM and compare their performances in this section. Since the analysis value of 3-D FEM is compared and checked against the actual measured value its validity is guaranteed in [3].

Considering the skin effect, 2-D optimum shape is able to be simplified from the viewpoint of weight reduction as shown in Fig. 8(b). This simplification aims to further improve the manufacturability of the feasible optimum shape and lower the cost of the conductor plate. The skin depth is calculated to be 0.2mm, however, in order to provide structural strength the conductor plate thickness is set to 3mm. We analyzed three 3-D analysis models with conductor plate lengths in the rail track direction of 120mm, 160mm, and 200mm, all of which are longer than that of the receiving coil. Fig. 9 shows 3-D models with the various conductor plate lengths in the rail track direction.

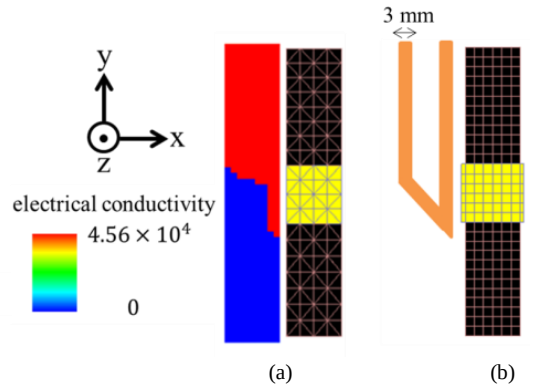

Fig. 8: Conductor plate (a)2-D optimum shape (b)Simplified shape

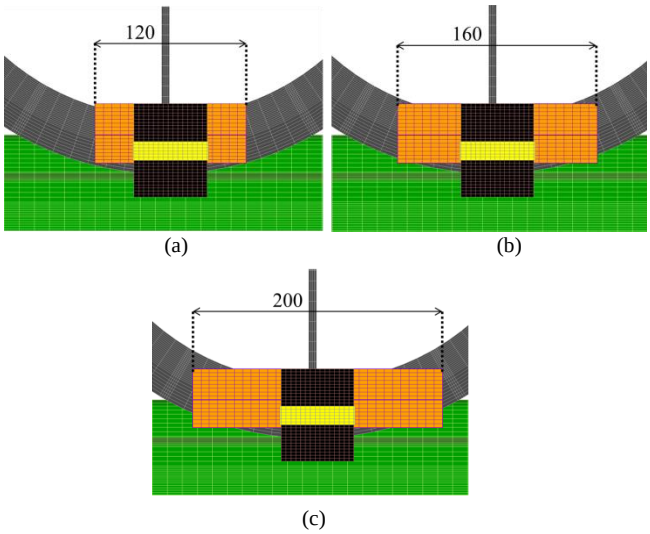

Fig. 9: Comparison of the models with conductor plate length in the rail track direction of (a) 120 mm, (b) 160mm, and (c) 200mm

We define the phase difference as 180 degrees in the case without a wheel, and if it is less than 90 degrees the axle counter detects the wheel. The relationship between the relative position of the wheel and phase difference is shown in Fig. 10(a). Here the relative position is defined as 0 in the case where a wheel is next to the axle counter. We can observe two characteristics of the detection. First, the conductor plate enables the axle counter to extend operating range from 215mm to 340mm and leads to more phase inversion compared to the case without a conductor plate. Second, the improving of the operating range is saturated in the case of the conductor plate length in the rail track direction of 160mm.

Fig. 10(b) shows the relationship between the relative position of the wheel and the amount of the induced voltage. It shows that setting a conductor plate increases the amount of induced voltage in the case where the axle counter detects the wheel. We also found that the increase of the amount of induced voltage is saturated in the case of the conductor plate length in the rail track direction of 160mm. Based on these results and in consideration of cost saving, we conclude that the 3-D optimum shape is the model with a conductor plate length in the rail track direction of 160mm as shown in Fig. 11.

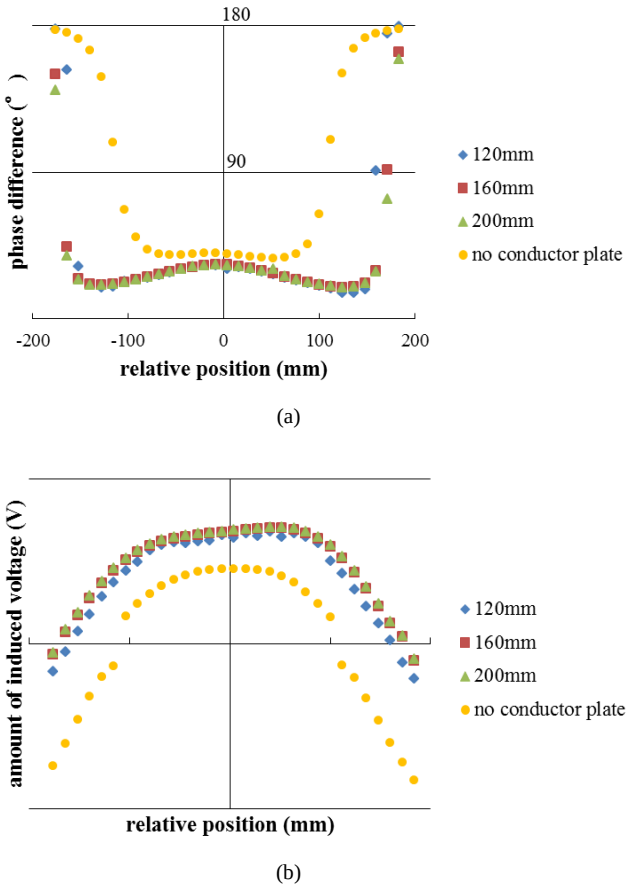

Fig. 10: Comparison of the results of the 3-D models.
(a) Operating range (b) amount of the induced voltage

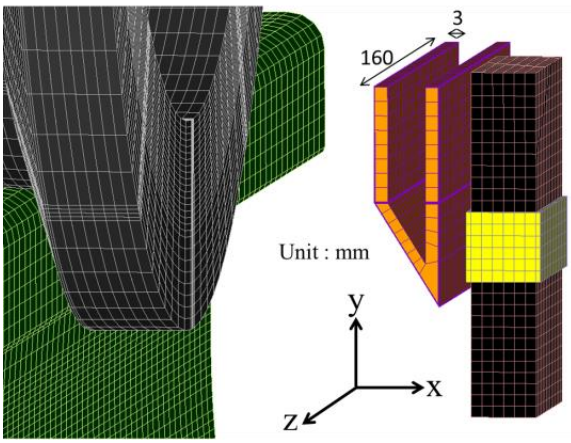

Fig. 11: Optimum shape and position of a conductor plate

VII. Consideration For The Stability Of The Detection Performance

When a train runs, various changes of the operating condition occur. As a typical example, a wheel slips from the center of a rail by train meandering as shown in Fig. 12. In this paper, we investigate the stability against the slippage of a wheel. In addition, we also investigate how the stability changes by introducing a conductor plate.

We assume that the maximum slippage of a wheel is 30mm. Therefore, we analyze three 3-D analysis models as shown in Fig. 12. A wheel in Fig. 12(b) and (c) is 15mm and 30mm away from the original position respectively.

Fig. 13 shows the relationship between the relative position of the wheel and the phase difference with and without a conductor plate in Fig. 13(a) and (b) respectively. Fig. 13 proves a conductor plate reduces the changes in the detection performance and the increase the stability.

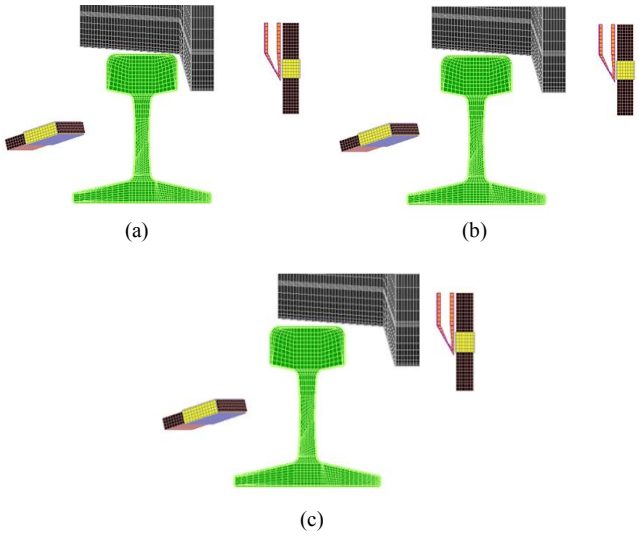

(a) (b)

(c)

Fig. 12: Comparison of the models which a wheel is at the (a) original position, (b) 15mm and (c) 30mm away from there

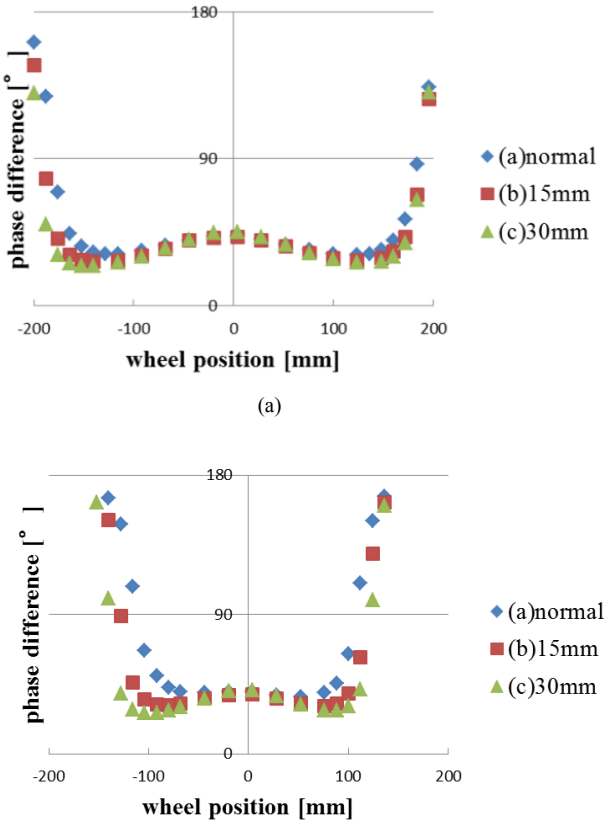

Fig. 13: Comparison of the changes of the phase difference (a) with and (b) without a conductor plate

The approach of a wheel to the receiving coil makes it easier that the magnetic flux flows into the receiving coil from the bottom to the top. With a conductor plate, the performance is the same as the case where a wheel approaches the receiving coil though these two are away each other.

For the reasons stated above, we can confirm the stability against the slippage of a wheel increases by introducing a conductor plate.

VIII. Conclusion

In this paper, we propose the novel introduction of a conductor plate to an axle counter, and optimize its 2-D shape and the position of the receiving coil using level-set method. We impose an appropriate area limitation set by referencing the size of the design area to get a block and easily manufactured feasible optimum shape. It also helps us to resolve the problem where the final shape of evaluation function changes depending on the initial shape.

After optimizing the 2-D model, we analyze different 3-D models, based on the 2-D optimum shape, by 3-D FEM and compare their performances. The improvement of the objective functions is saturated in the case of the conductor plate length in the rail track direction of 160mm. Based on this and cost saving considerations we conclude the 3-D optimum shape and position, which expands the operating range about 1.6 times from the range without a conductor

plate, to be the shape and position as depicted in Fig.11.

Finally, as changes of operating condition, we investigate the stability against train meandering. From the analysis results, we can verify the axle counter with the conductor plate proposed in this paper improves its performance further than the case without a conductor plate.

REFERENCE

[1] H. Kuwahara, et al., "Multi-objective Optimization of Magnetic Sensor with Conductor Plate for Rail Wheel Detection," *IEEE CEFC*, Miami, USA, Nov. 2016

[2] Asuka Otake, Kenta Takayasu, Shinji Wakao, Tamio Okutani, Yasuhito Takahashi, Masahiko Saito, and Akihisa Toyoda, "Design of railway wheel detector insusceptible to electromagnetic noise," *IEEE Trans. Magn.*, vol.46, No.8, pp. 2731-2734, Aug. 2010

[3] Shogo Yasukawa, Naoko Takagi, Gege Dong, Shinji Wakao, Masahide Takahashi, Makoto Yagi and Tamio Okutani, "Design optimization of magnetic sensor for train detection," *IEEE Trans. Magn*., vol.51, No.3, Mar. 2015

[4] Yoshifumi Okamoto, Shinji Wakao, and Shuji Sato, "Topology optimization based on regularized level-set function for solving 3-D nonlinear magnetic field System with spatial symmetric condition," *IEEE Trans. Magn.*, vol.52, NO. 3, March 2016

[5] H.K. Jung, G.S. Lee, and S.Y. Hahn: "3-D Magnetic field computation using Finite-Element approach with localized functional," *IEEE Trans. Magn.*, vol. 21, no. 6, pp. 2196-2198, 1985

[6] M. P. Bendsøe, "Optimal shape design as a material distribution problem," *Struct. Optim.*, vol. 1, no. 4, pp. 193–202, 1989.

[7] D. N. Dyck and D. A. Lowther, "Automated design of magnetic devices by optimizing material distribution," *IEEE Trans. Magn.*, vol. 32, no. 3, pp. 1188–1193, May 1996.

[8] J.-K. Byun, I.-H. Park, and S.-Y. Hahn, "Topology optimization of electrostatic actuator using design sensitivity," *IEEE Trans. Magn*., vol. 38, no. 2, pp. 1053–1056, Mar. 2002.

[9] A. Kameari, "Magnetic field analysis using hybrid meshes of linear hexahedral and tetrahedral edge elements," *IEEE Trans. Magn.*, vol. 44, no. 6, pp. 1182-1185, 2008.

Temperature-dependent hysteresis model for soft magnetic materials

[1]Maria Roberta Longhitano, [2]Fabien Sixdenier, [2]Riccardo Scorretti, [2]Laurent Krähenbühl, [3]Christophe Geuzaine

[1]Laboratoire Ampere, Ecole Centrale de Lyon, Lyon, France
[2]Laboratoire Ampere, Ecole Centrale de Lyon, Lyon, France and CNRS, Universite Claude Bernard Lyon 1, Lyon, France
[3]Department of Electrical Engineering and Computer Science, Universite de Liege, Liege, Belgium

Purpose:
To understand the behavior of the magnetization processes in ferromagnetic materials in function of temperature, a temperature-dependent hysteresis model is necessary. This study aims to investigate how temperature can be accounted for in the energy-based hysteresis model, via an appropriate parameter identification and interpolation procedure.

Design/methodology/approach:
The hysteresis model used for simulating the material response is energy-consistent and relies on thermodynamic principles. The material parameters have been identified by unidirectional alternating measurements, and the model has been tested for both simple and complex excitation waveforms. Measurements and simulations have been performed on a soft ferrite toroidal sample characterized in a wide temperature range.

Findings:
The analysis shows that the model is able to represent accurately arbitrary excitation waveforms in function of temperature. The identification method used to determine the model parameters has proven its robustness: starting from simple excitation waveforms, the complex ones can be simulated precisely.

Originality/value:
The results suggest that it is possible to predict magnetization curves within the measured range, starting from a reduced set of measured data.

Keywords:
Magnetic hysteresis, Thermal analysis, Soft magnetic materials, Material modeling

Published in COMPEL - The international journal for computation and mathematics in electrical and electronic engineering, Vol. 38 No. 5, 2019, ISSN 0332-1649, page 1595 - 1613

Finite-element analysis of turbine generator using homogenization method taking account of magnetic anisotropy

[1]Ryoko Minehisa, [1]Yasuhito Takahashi, [1]Koji Fujiwara, [2]Norio Takahashi, [2]Masafumi Fujita, [2]Kazuma Tsujikawa, [2]Ken Nagakura

[1]Department of Electrical Engineering, Doshisha University, Kyotanabe, Japan
[2]Toshiba Energy Systems and Solutions Corporation, Kawasaki, Japan

Purpose:
This paper aims to propose a homogenization method considering magnetic anisotropy for a magnetic field analysis of a turbine generator. To verify the validity of the proposed method, the effects of magnetic anisotropy and a space factor on a no-load saturation curve and no-load iron loss of the turbine generator are discussed.

Design/methodology/approach:
The proposed method was derived from the combination of the homogenization of microscopic fields in a laminated iron core with the modelling of two-dimensional magnetic properties based on free energy. To verify the validity, the proposed method was applied to a finite element analysis of a simple ring core model. Finally, a no-load saturation curve and iron loss of the turbine generator was investigated by using the proposed method.

Findings:
The computational accuracy of the homogenization method considering magnetic anisotropy is almost the same as that of the detailed modelling of the laminated structure in the magnetic field analysis of the laminated iron core. Furthermore, it is clarified that magnetic anisotropy does not have a large influence on the no-load saturation curve of the turbine generator because of the large air gap. On the other hand, the space factor affects the shape of the no-load saturation curve.

Originality/value:
This paper verifies the validity of the homogenization method considering magnetic anisotropy method and elucidates the effects of magnetic anisotropy and a space factor on no-load characteristics of the turbine generator.

Keywords:
Finite element analysis, Homogenization method, Lamination modelling, Magnetic anisotropy

Published in COMPEL - The international journal for computation and mathematics in electrical and electronic engineering, Vol. 38 No. 5, 2019, ISSN 0332-1649, page 1614 - 1626

Enhancement of cconvergence characteristic of Newton-Raphson method with line search for nonlinear eddy current analysis based on time-periodic FEM

Shimpei Kakita, Yoshifumi Okamoto

Department of Electrical and Electronic Engineering, Hosei University, Tokyo, Japan

Purpose:
The paper aims to improve convergence characteristics of the NewtonRaphson (NR) method applied to time-periodic finite element method using various line searches, as time-periodic finite element method causes deterioration of convergence characteristic of nonlinear analysis based on NR method. The study also aims to accelerate and improve accuracy of electromagnetic field analysis for improvement of the performance of electrical machine.

Design/methodology/approach:
The paper proposes new type line searches that set approximate step size for NR method. The line search evaluated step size using higher-order interpolation of functional derivative. In addition, two criteria for applying these line search were proposed. First method set one scalar value for every NR iteration that is named constant step size. Second method define different step size in each time step of time-periodic finite element method to update solution vector that is named different step size.

Findings:
The paper provides efficient line searches to improve convergence characteristics for NR method. Nonlinear magnetic field analysis of two transformer models is demonstrated. The proposed methods achieve the following results: higher-order functional NR is efficient in improving convergence characteristics, and the proposed methods succeeded about twice faster in both models.

Originality/value:
The paper fulfills improvement of convergence characteristics of the NR method applied to time-periodic finite element method using proposed line searches and accelerate electromagnetic field analysis.

Keywords:
NewtonRaphson method, Line-search, Time-periodic finite element method,Steady plate analysis

Published in COMPEL - The international journal for computation and mathematics in electrical and electronic engineering, Vol. 38 No. 5, 2019, ISSN 0332-1649, page 1627 - 1640

Optimization Procedure for Approximation of Square-shaped Wire Electrode by a Ring Electrode

*Nenad Cvetkovic, †Marinko Barukcic, *Dejan Jovanovic, *Miodrag Stojanovic and †Zeljko Hederic
*University of Nis, Faculty of Electronic Engineering, A. Medvedeva 14, 18000 Nis, Serbia
†J.J. Strossmayer University of Osijek, FERIT, Kneza Trpimira 2B, 31000 Osijek, Croatia
E-mail: nenad.cvetkovic@elfak.ni.ac.rs

***Abstract*—The grounding systems realized in practice very often include a square-shaped electrode. Since circularly shaped grounding electrode is simpler for analyzing, there is an interest to find some appropriate relation between square side and radius of equivalent circular wire electrode that would approximately model the square electrode. In this paper, the optimization procedure for the approximation of square electrode by a ring of the equivalent radius is proposed. That approach includes using the heuristic global optimization technique based on the Ant Colony Optimization (ACO). The obtained results are compared with those obtained using other approaches.**

***Index Terms*—Evolutionary computation, grounding, quasi-stationary regime, wire electrode.**

I. INTRODUCTION

Very often, grounding systems include basic star, rectangular or circularly shaped electrode [1]-[2] connected to an iron armature of the pillar foundation, which can be treated as a second part of the grounding system. As it is well known, the grounding system which includes a ring electrode is simpler for numerical analysis comparing to the system including the rectangular shaped electrode. Because of that, it could be of interest to find some appropriate relation between dimensions of the rectangular electrode and radius of equivalent circular wire electrode that would approximately model the square electrode. In this paper square-shaped electrode, as most often used rectangular ground electrode, is observed. The relation between dimension and depth of square-shaped electrode and equivalent depth and radius of ring electrode is derived, based on electric potential distribution at the ground surface and ground electrode resistance value. The results are compared with those from [3]-[4]. In these papers, the square electrode is approximated by a ring electrode of the same length and same surface as a square electrode, as well as by the ring electrode which equivalent radius is determined by estimation method [5]. The analysis is carried out in the quasi-stationary regime.

In this paper, the problem will be solved using optimization method based on an Evolutionary Algorithm (EA). That approach includes using heuristic global optimization techniques. The EAs belong to a class of the global optimizers, population-based and near to global optimum methods. The main feature of the EAs is that searching the solution space in the parallel process provides avoiding the stuck into the local optimums. There are a lot of different EAs methods, very well covered in the literature, dealing with soft computing techniques. Among different evolutionary optimization tools, the MIDACO (Mixed Integer Distributed Ant Colony Optimization) solver [6] is chosen to be used here. It is based on ACO technique and can be applied for solving general single/multi-objective optimization problems [7]. It is a powerful and easy EA optimization tool, very suitable for co–simulation, since it is available for different programming.

II. THEORETICAL BACKGROUND

A. The square-shaped ground electrode

The square-shaped ground electrode of side *a*, placed at depth *h* is observed, Fig. 1. The surrounding ground is assumed as the homogeneous domain of specific conductivity σ_1. The electrode is made of a strip conductor (usually FeZn strip) assumed to be a wire conductor having an equivalent circular cross-section of a radius r_0, $r_0 << a, h$, [5]. The reflection coefficient ground-air R_{10} is practically equal to one, i.e.

$$R_{10} = (\sigma_1 - \sigma_0)/(\sigma_1 + \sigma_0) \approx 1, \quad (1)$$

where σ_0 is air specific conductivity, $\sigma_0 \approx 0$.

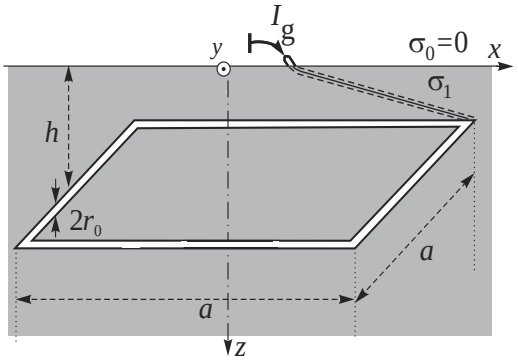

Figure 1: Single square-shaped ground electrode.

The feeding current is modeled by an ideal very low-frequency current generator I_g, while leakage current $I_{leak}(s')$ distribution along the wire axis (s') is assumed as constant, which is justified for the quasi-stationary regime. ($r_0, a, h << \lambda$, where λ is a wavelength corresponding to the current generator frequency in the surrounding ground),

$$I_{leak}(s') = -\partial I(s')/\partial s' = -I'(s') = I_{gk}/(4a), \quad (2)$$

where $I(s')$ is unknown longitudinal current distribution

along the square-shaped conductor. The electrode surface is assumed to be equipotential of potential value *U*.

The electric scalar potential at the point in the vicinity of the grounding system shown in Fig. 1, defined by the field vector $\vec{r}_{\mathrm{p}}$, can be determined using the expression:

$$\varphi(\vec{r}_{\mathrm{p}}) = \frac{I_{\mathrm{g}}}{4\pi\sigma_1 4a} \int_{l_{\mathrm{square}}} \left(\frac{1}{r_k} + \frac{1}{r_{k\mathrm{i}}} \right) \mathrm{d}s' , \qquad (3)$$

where r_k and $r_{k\mathrm{i}}$ denote distances between the current element, i.e., its image, and the field point, respectively. Applying the Method of Moments [8] and matching potential value on the conductors' surface defined by the field vector $\vec{r}_{\mathrm{p}} = 0.5a\,\hat{x}$ the integral equations are formed:

$$\varphi(\vec{r}_{\mathrm{p}} = 0.5a\,\hat{x}) \cong U \ , \ n = 1,2 . \qquad (4)$$

After solving equation (4), the resistance of the electrode from Fig. 1 is

$$R_{\mathrm{g}} = U / I_{\mathrm{g}} . \qquad (5)$$

B. The ring ground electrode

The ring ground electrode of radius a_{e}, placed at depth h_{e} and fed by low-frequency current generator I_{g} is observed, Fig. 2. Again, the surrounding ground is assumed as the homogeneous domain of specific conductivity σ_1 and the radius of an equivalent circular cross-section is r_0, $r_0 << a_{\mathrm{e}}, h_{\mathrm{e}}$, and $R_{10} \approx 1$.

Assuming leakage current distribution as constant, electric scalar potential at the point defined by field vector $\vec{r}_{\mathrm{p}}$ can be determined as [9],

$$\varphi = \frac{I_{\mathrm{g}}}{2\pi^2\sigma_1} \left[\frac{K(\frac{\pi}{2}, k_1)}{\sqrt{(a_{\mathrm{e}} + r)^2 + (z - h_{\mathrm{e}})^2}} + \frac{K(\frac{\pi}{2}, k_2)}{\sqrt{(a_{\mathrm{e}} + r)^2 + (z + h_{\mathrm{e}})^2}} \right], r = \sqrt{x^2 + y^2} \qquad (6)$$

where

$$K(\frac{\pi}{2}, k) = \int_0^{\pi/2} \frac{\mathrm{d}x}{\sqrt{1 + k^2 (\sin x)^2}} \qquad (7)$$

is the complete elliptic integral of the first kind, while corresponding modulus are,

$$k_1^2 = \frac{4 r\, a_{\mathrm{e}}}{(r + a_{\mathrm{e}})^2 + (z - h_{\mathrm{e}})^2} \text{ and } k_2^2 = \frac{4 r\, a_{\mathrm{e}}}{(r + a_{\mathrm{e}})^2 + (z + h_{\mathrm{e}})^2} .$$

The resistance of the ring electrode is [9],

$$R_g = \frac{1}{2\pi^2\sigma_1} \left[\frac{1}{\sqrt{4a_{\mathrm{e}}^2 + r_0^2}} K(\pi/2, k_1) + \frac{1}{\sqrt{4a_{\mathrm{e}}^2 + (2h_{\mathrm{e}} + r_0)^2}} K(\pi/2, k_2) \right]. \qquad (8)$$

In (8) are

where $k_1^2 = \frac{4 r_K^2}{4a_{\mathrm{e}}^2 + r_0^2}$ and $k_2^2 = \frac{4a_{\mathrm{e}}^2}{4a_{\mathrm{e}}^2 + (2h_{\mathrm{e}} + r_0)^2}$.

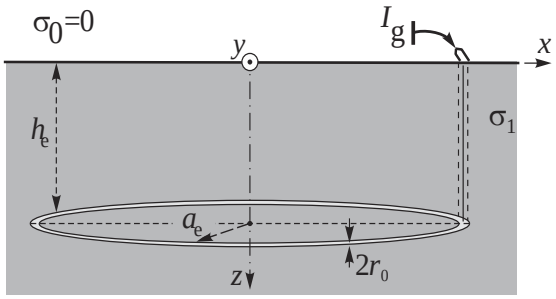

Figure 2: Equivalent ring ground electrode.

C. Approximation of wire square electrode with an equivalent ring electrode

Based on expressions (1)-(5) (for the square-shaped ground electrode) and expressions (6)-(8) for ring ground electrode, the optimization procedure for determining parameters of ring electrode (depth h_{e} and radius a_{e}) which approximate square electrode (side *a* and depth *h*) is formed. The procedure is based on optimization of the objective function

$$f_{\mathrm{obj}}(h_{\mathrm{e}}, a_{\mathrm{e}}) = \left(R_{\mathrm{sq}} - R_{\mathrm{e}}\right)^2 + \sum_{i=1}^{N} \left(\varphi_{\mathrm{sq},i} - \varphi_{\mathrm{e},i}\right)^2 \qquad (9)$$

subject to constraints

where R_{sq} is grounding resistance of the original square grounding electrode, R_{e} is grounding resistance of the equivalent ring grounding electrode, $\varphi_{\mathrm{sq},i}$ is potential of *i*-th point on the surface in case of the original square grounding electrode and $\varphi_{\mathrm{e},i}$ is potential of *i*-th point on the surface in case of the ring electrode. The optimization problem has been solved by using metaheuristic optimization method based on the Ant Colony Optimization (ACO) technique. The obtained results are also compared with those obtained using methods presented in [3]-[4], where the equivalent radius is obtained using relations

$$a_{\mathrm{e}} = 0.25a\left(1 + \sqrt{2}\right) \text{ (estimation method),} \qquad (10a)$$

$$2a_e\pi = 4a \Rightarrow a_{\mathrm{e}} = \frac{2a}{\pi} \text{ (same length) and} \qquad (10b)$$

$$a_{\mathrm{e}}^2\pi = a^2 \Rightarrow a_{\mathrm{e}} = \frac{a}{\sqrt{\pi}} \text{ (same surface).} \qquad (10c)$$

It is important to emphasize that expressions (10a-c) considers only equivalent radius, while depths of square-shaped electrode and ring electrodes are equal.

III. Numerical results

The described procedure is applied for optimization of the square-shaped electrode having side $a = 1\,\mathrm{m}$, cross-section radius $r_0 = 9.7\,\mathrm{mm}$ [3], while its position depth values were $h = 0.5\,\mathrm{m}$, $1\,\mathrm{m}$, $1.5\,\mathrm{m}$, $2\,\mathrm{m}$ and $3\,\mathrm{m}$. The specific conductivity of the ground is $\sigma_1 = 0.01\,\mathrm{S/m}$ and

low frequency fed current value is $I_g = 1\text{A}$. The used ranges of the problem decision variables are $0.5\text{m} \le a_e \le 2.5\text{m}$ and $0.2\text{m} \le h_e \le 10\text{m}$. The potential value at the ground surface was determined at six points, which are determined based on the symmetrical characteristics of the square, Fig. 3.

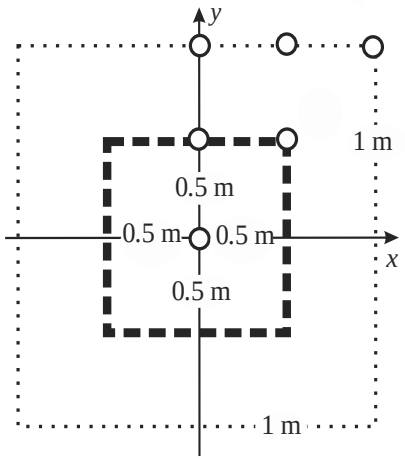

Figure 3: Ground surface points.

The equivalent parameters of the ring electrode (depth h_e and radius a_e) for various values of square-shaped electrode of depth h are given in Table I. In Table II equivalent radius a_e values determined from expressions (10a-c) are given.

The potential distributions at the ground surface of square-shaped and equivalent ring electrode, at the ground surface points from Fig. 3 for different values of h are shown in Fig. 4.

The relative error of potential value determining and relative error of resistance determining are shown in Figs 5 and 6 respectively. In Fig. 7 the resistances of square-shaped and ring electrode versus square electrode depth are given, while the radius and depth of ring electrode versus square electrode depth can be seen in Fig. 8.

TABLE I
EQUIVALENT PARAMETERS OF THE RING ELECTRODE AND OBJECTIVE FUNCTION VALUES

h [m]	h_e [m]	a_e [m]	f_{obj}
0.5	0.501	0.601	12.637
1	1.06	0.624	1.466
1.5	1.634	0.596	0.145
2.0	2.213	0.597	0.072
3.0	3.430	0.598	0.021

TABLE II
EQUIVALENT RADIUS OF THE RING ELECTRODE

Expression	(10a)	(10b)	(10c)
a_e [m]	0.604	0.637	0.564

From Figs 4-8 one can conclude that equivalent radius of ring electrode do not significantly depend on square electrode depth. Also, there is good coinciding of the resistance value, including the values obtained using expressions (10a-c).

Also, from Fig. 8 can be seen that ring electrode depth h_e is larger than square-shaped electrode h and difference between these two values is increasing with depth increasing.

Finally, the coinciding of potential values is good, except for h=0,5 m.

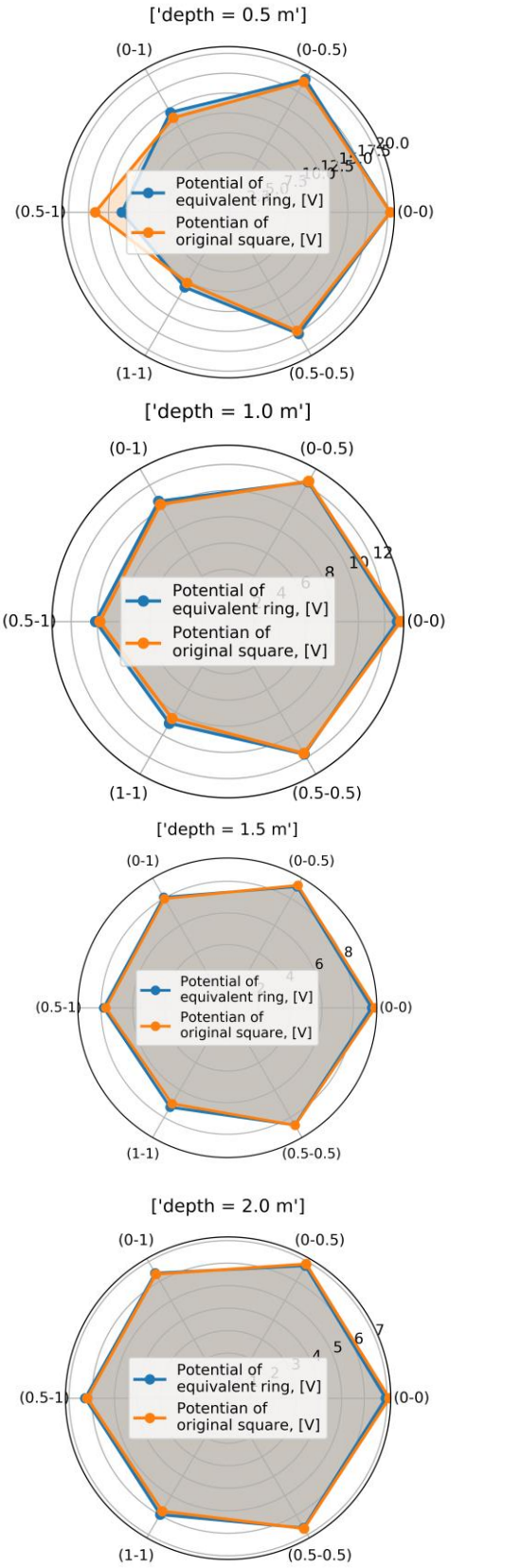

Figure 4: Potential distribution at the ground surface in [V] for h=0.5, 1, 1.5 and 2 m.

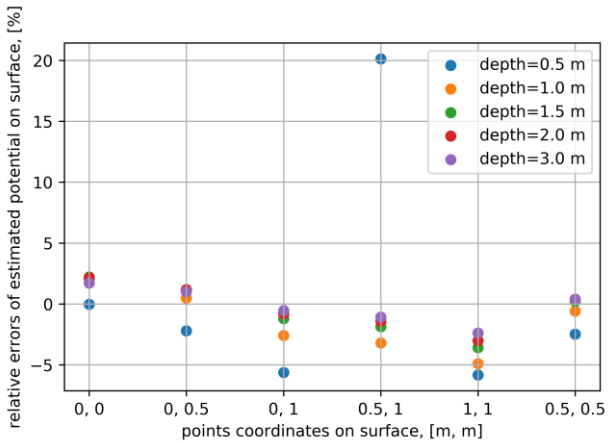

Figure 5: Relative error of potential value determining.

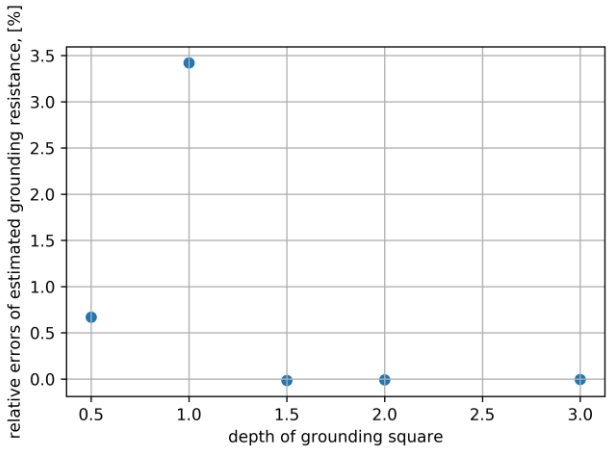

Figure 6: Relative error of resistance determining.

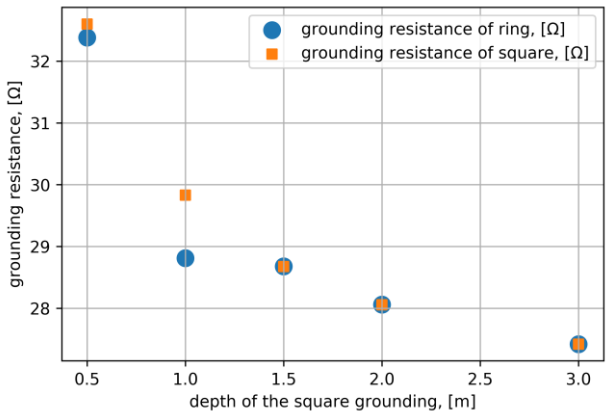

Figure 7: Resistance of square-shaped and ring electrode.

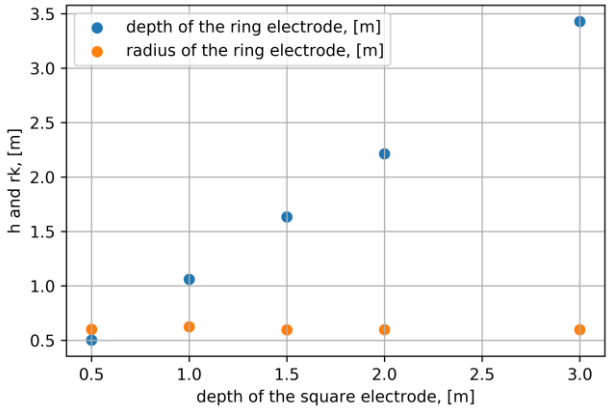

Figure 8. Equivalent radius a_e and depth h_e of ring electrode versus square electrode depth h.

IV. Conclusions

One procedure for determining equivalent parameters of ring electrode (depth and radius) which approximates square-shaped electrode is presented in the paper. The reason for that is the fact that the ring electrode is simpler for numerical analysis comparing to rectangular shaped electrode.

The optimization procedure is based on minimizing the objective function which includes potential distribution at the ground surface and electrode resistance as main ground electrode characteristic.

Obtained results lead to the conclusion that it is possible to approximate square-shaped electrode with ring electrode with satisfactory accuracy. The procedure presented in the paper can be used as base for deriving empirical expression which could be used in practical engineering calculation procedures.

Also, from Fig. 8 can be seen that ring electrode depth h_e is larger than square-shaped electrode h and difference between these two values is increasing with depth increasing.

Finally, the coinciding of potential values is good, except for h=0,5 m.

Acknowledgement

This paper is supported in part by project grants TR33035 and III44004 financed by Ministry of Education, Science and Technological Development of Republic of Serbia.

References

[1] *Technical Recommendation 9 of Electric Power Industry of Serbia: Grounding of the Power Network Pillars*, 3rd ed., Belgrade 2010. (in Serbian). Available at: https://goo.gl/YGPpiY.

[2] J. Nahman, *Neutral Grounding of Distribution Networks*, Naučna knjiga, Belgrade, Serbia, 1980, pp. 281-288. (in Serbian)

[3] P. D. Rancic and N. N. Cvetkovic, "Square shaped eelctrode as pillar grounding system," *9th International Conference on Telecomunications in Modern Satellite, Cable and Broadcasting Services-TELSIKS 2009*, October 07-09, 2009, Niš, Serbia, Proceeding of papers, vol. 2, pp. 351-354. DOI: 10.1109/TELSKS.2009.5339524

[4] N. N. Cvetkovic, "System of square-shaped electrodes as a pillar grounding system," *XLVI International Scientific Conference on Information, Communication and Energy Systems and Technologies - ICEST 2011*, June 29 - July 1, 2011, Niš, Serbia, Proc. of papers, vol. I, pp. 195-198, ISBN: 978-86-6125-031-6. Avaliable at: https://goo.gl/c5fkEA

[5] N. N. Cvetković and P. D. Rančić, "Influence of foundation on pillar grounding system's characteristics," *COMPEL: The International Journal for Computation and Mathematics in Electrical and Electronic Engineering*, Emerald Group Publishing Limited, vol. 28, 2009, pp. 471-492 .DOI: 10.1108/03321640910929335

[6] M. Schlüter, M. Gerdts and J-J Rückmann, "A numerical study of MIDACO on 100 MINLP benchmarks," *Journal of Mathematical Programming and Operations Research*, vol. 61, 2012, pp. 873–900.
DOI: 10.1080/02331934.2012.668545

[7] M. Schlüter, J.A. Egea and J.R. Banga, "Extended ant colony optimization for non-convex mixed integer nonlinear programming," *Computers & Operations Research*, vol. 36, 2008, pp. 2217–2229. DOI: 10.1016/j.cor.2008.08.015

[8] R. R. Harrington, *Field computation by Moment Methods*, The Macmillan Company, New York, USA, 1969.

[9] P. D. Rančić and N. N. Cvetković, "Current Distribution and Impedance of Ring Electrode Pillar Grounding System: Quasistationary Antenna Model," *8th International Conference on Telecomunications in Modern Satellite, Cable and Broadcasting Services-TELSIKS 2007*, September 26-28, 2007, Niš, Serbia, Proceeding of papers, vol. 2, pp. 569-572. DOI: 10.1109/TELSKS.2007.4376076

Performance of Krylov subspace method with SOR preconditioner supported by Eisenstats technique for linear system derived from time-periodic FEM

Makoto Kumagai, Shimpei Kakita, Yoshifumi Okamoto

Department of Electrical and Electronic Engineering, Hosei University, Tokyo, Japan

Purpose:
This paper aims to present the affinity of BiCGStab and BiCGStab2 with successive over-relaxation (SOR) preconditioner supported by Eisenstats technique for a linear system derived from the time-periodic finite element method (TP-FEM). To solve the time domain electromagnetic field problem with long transient state, TP-FEM is very useful from the perspective of rapidly achieving a steady state. Because TP-FEM solves all of the state variables at once, the linear system derived from TP-FEM becomes the large scale and nonsymmetric, whereas the detailed performance of some preconditioned Krylov subspacemethod is not reported.

Design/methodology/approach:
In this paper, BiCGStab and BiCGStab2 are used as the linear solver for a large-sparse nonsymmetric linear system derived from TP-FEM. In addition, incomplete LU (ILU)factorization is applied as a preconditioner to compare SOR supported by Eisenstats technique. As examples, the pot-type reactor and three-phase transformer is analyzed.

Findings:
In the problem of the pot-type reactor, when SOR preconditioner supported by Eisenstats technique is applied to BiCGStab and BiCGStab2, the elapsed time can be reduced dramatically. However, in the problem of the three-phase transformer, the iterative process of the linear solvers with SOR preconditioner is not terminated, whereas the iterative process of linear solvers with ILU preconditioner is terminated. The preconditioner that can be supported by Eisenstats technique is not necessarily appropriate for the problem to derive from TP-FEM.

Originality/value:
In this paper, the affinity of preconditioned linear solver supported by Eisenstats technique for the nonsymmetric linear system derived from TP-FEM is demonstrated.

Keywords:
Time-periodic finite element method, Nonsymmetric linear system, BiCGStab2,Eisenstats technique

Published in COMPEL - The international journal for computation and mathematics in electrical and electronic engineering, Vol. 38 No. 5, 2019, ISSN 0332-1649, page 1641 - 1654

Worst-case analysis of electronic circuits based on an analytic forward solver approach

[1]Mario Schenk, [1]Annette Muetze, [1]Klaus Krischan, [2]Christian Magele

[1]Electric Drives and Machines Institute (EAM), Graz University of Technology, Graz, Austria
[2]Institute of Fundamentals and Theory in Electrical Engineering (IGTE), Graz University of Technology, Graz

Purpose:
The purpose of this paper is to evaluate the worst-case behavior of a given electronic circuit by varying the values of the components in a meaningful way in order not to exceed pre-defined currents or voltages limits during a transient operation.

Design/methodology/approach:
An analytic formulation is used to identify the time-dependent solution of voltages or currents using proper state equations in closed form. Circuits with linear elements can be described by a system of differential equations, while circuits composing nonlinear elements are described by piecewise-linear models. A sequential quadratic program (SQP) is used to find the worst-case scenario.

Findings:
It is found that the worst-case scenario can be obtained with as few solutions to the forward problem as possible by applying an SQP method.

Originality/value:
The SQP method in combination with the analytic forward solver approach shows that the worst-case limit converges in a few steps even if the worst-case limit is not on the boundary of the parameters

Keywords:
Computer-aided design, Transient analysis, Circuit analysis, Power electronic simulation, Circuit simulation, SQP, Time-domain analysis

Published in COMPEL - The international journal for computation and mathematics in electrical and electronic engineering, Vol. 38 No. 5, 2019, ISSN 0332-1649, page 1655 - 1666

A MSFEM to simulate the eddy current problem in laminated iron cores in 3D

Karl Hollaus

Department of Analysis and Scientific Computing, Visual Computing and Human-Centered Technology, Wien, Austria

Purpose:
The simulation of eddy currents in laminated iron cores by the finite element method (FEM) is of great interest in the design of electrical devices. Modeling each laminate by finite elements leads to extremely large nonlinear systems of equations impossible to solve with present computer resources reasonably. The purpose of this study is to show that the multiscale finite elementmethod (MSFEM) overcomes this difficulty.

Design/methodology/approach:
A new MSFEM approach for eddy currents of laminated nonlinear iron cores in three dimensions based on the magnetic vector potential is presented. How to construct the MSFEM approach in principal is shown. The MSFEM with the BiotSavart field in the frequency domain, a higher-order approach, the time stepping method and with the harmonic balancemethod are introduced and studied.

Findings:
Various simulations demonstrate the feasibility, efficiency and versatility of the new MSFEM.

Originality/value:
The novel MSFEM solves true three-dimensional eddy current problems in laminated iron cores taking into account of the edge effect.

Keywords:
Eddy currents, Finite element method, BiotSavart field, Harmonic balance method, Higher-order MSFEM, Multiscale finite element method, Time stepping method

Published in COMPEL - The international journal for computation and mathematics in electrical and electronic engineering, Vol. 38 No. 5, 2019, ISSN 0332-1649, page 1667 - 1682

Simulating metallic contamination in permanent magnets used in magnetic sensors

Safire Torres Santos da Silva, Nikola Jerance, Harijaona Lalao Rakotoarison

Electricfil Automotive, Miribel, France

Purpose:
The purpose of this paper is to provide a model for simulating contamination by ferromagnetic particles in sensors that use permanent magnets. This topic is especially important for automotive applications, where magnetic sensors are extensively used and where metallic particles are present, particularly because of friction between mechanical parts. The aim of the model is to predict the particle accumulation and its effect on the sensor performance.

Design/methodology/approach:
Magnetostatic moment method is used to calculate particles magnetization and magnetic field. Magnetic saturation is included and NewtonRaphson method is used to solve the non-linear system. Magnetic force on particles is calculated as a gradient of energy. Dynamic simulation provides the positions of agglomerated particles.

Findings:
A simulation of magnetic park lock sensor shows a significant impact of ferromagnetic particles on sensors accuracy. Moreover, gains on computational time because of model optimizations are reported.

Originality/value:
The paper presents a novel simulation tool developed to answer the growing need for reliable and fast prediction of magnetic position sensors degradation in the presence of metallic particles.

Keywords:
Electromagnetism, Sensors magnetic sensors, Metallic contamination, Magnetostatic moment method

Published in COMPEL - The international journal for computation and mathematics in electrical and electronic engineering, Vol. 38 No. 5, 2019, ISSN 0332-1649, page 1683 - 1695

Comparison of different vector Preisach models for the simulation of ferromagnetic materials

[1]Michael Nierla, [1]Michael Loeffler, [2]Manfred Kaltenbacher, [1]Stefan Johann Rupitsch

[1]Department of Electrical, Electronic and Communication Engineering, Friedrich-Alexander-University Erlangen-Nuremberg, Erlangen, Germany
[2]Institute of Mechanics and Mechatronics, Vienna University of Technology, Vienna, Austria

Purpose:
The numerical computation of magnetization processes in moving and rotating assemblies requires the usage of vector hysteresis models. A commonly used model is the so-called Mayergoyz vector Preisach model, which applies the scalar Preisach model into multiple angles of the halfspace. The usage of several scalar models, which are optionally weighted differently, enables the description of isotropic as well as anisotropic materials. The flexibility is achieved, however, at the cost of multiple scalar model evaluations. For solely isotropic materials, two vector Preisach models, based on an extra rotational operator, might offer a lightweight alternative in terms of evaluation cost. The study aims at comparing the three mentioned models with respect to computational efficiency and practical applicability.

Design/methodology/approach:
The three mentioned vector Preisach models are compared with respect to their computational costs and their representation of magnetic polarization curves measured by a vector vibrating sample magnetometer.

Findings:
The results prove the applicability of all three models to practical scenarios and show the higher efficiency of the vector models based on rotational operators in terms of computational time.

Originality/value:
Although the two vector Preisach models, based on an extra rotational operator, have been proposed in 2012 and 2015, their practical application and inversion has not been tested yet. This paper not only shows the usability of these particular vector Preisach models but also proves the efficiency of a special stageless evaluation approach that was proposed in a former contribution.

Keywords:
Magnetic hysteresis, Everett function, Vector Preisach model, Material modelling, Computational electromagnetics, Vector vibrating sample magnetometer, Vector hysteresis

Published in COMPEL - The international journal for computation and mathematics in electrical and electronic engineering, Vol. 38 No. 5, 2019, ISSN 0332-1649, page 1696 - 1710

Experimental technique for high-frequency conductivity measurement

[1]Karoly Marak, [2]Sandor Bilicz, [1]Jozsef Pavo

[1]Department of Broadband Infocommunications and Electromagnetic Theory, Budapest University of Technology and Economics, Budapest, Hungary
[2]Budapest University of Technology and Economics, Budapest, Hungary

Purpose:
The purpose of this study is to introduce a novel method for the measurement of electromagnetic material parameters.

Design/methodology/approach:
The main idea behind the approach is the fact that for slabs with elongated shapes, the intensity of the backscattered field and the electromagnetic resonance frequency corresponding to the length of the sample are dependent on the conductivity of the samples material.

Findings:
It is shown that for a known scattered field and resonance frequency, it is possible to formulate an inverse problem as to the calculation of the conductivity of the samples material at the considered frequencies. To investigate the applicability of the method, demonstrative experiments are performed during which the micro-Doppler effect is used to increase the measurement accuracy. The idea is extended to the case of anisotropic samples, with slight modifications proposed to the experimental setup in the case of significant anisotropy in the investigated material.

Originality/value:
To the best of the authors knowledge, this is the first time the use of the micro- Doppler effect is proposed for the purpose of the measurement of material parameters.

Keywords:
Carbon fiber composites, Composite material, Conductivity measurement, Material parameters, Micro-Doppler effect

Published in COMPEL - The international journal for computation and mathematics in electrical and electronic engineering, Vol. 38 No. 5, 2019, ISSN 0332-1649, page 1711 - 1722

Index of Authors

Alotto, Piergiorgio, 43
Anders, Jens, 63
Ando, Atsushi, 89

Bajda, Yevgen, 31
Balabozov, Iosko, 19
Barukcic, Marinko, 101
Beković, Miloš, 83
Bilicz, Sándor, 117
Bretterklieber, Thomas, 47
Buchau, André, 63
Burger, Loïc, 27

Clemens, Markus, 61
Cvetkovic, Nenad N., 29, 101

Delkov, Dimitri, 49
Dulikravich, George S., 59

Essl, Christiane, 53

Fabian, Jürgen, 53
Filippini, Mattia, 43
Fujita, Masafumi, 97
Fujiwara, Koji, 25, 45, 77, 97

Geuzaine, Christophe, 27, 95
Ghorbanian, Vahid, 1
Gietler, Harald, 5
Giust, Alessandro, 43

Hamler, Anton, 83
Hayatsu, Masato, 11
Hederic, Zeljko, 101
Henrotte, François, 27
Herzog, Hans-Georg, 17, 75
Hollaus, Karl, 111

Iwashita, Takeshi, 45

Jerance, Nikola, 113
Jesenik, Marko, 83
Jovanovic, Dejan, 29, 101

Kakita, Shimpei, 99, 107
Kaltenbacher, Manfred, 71, 115
Kasolis, Fotios, 61
Klymenko, Borys, 31
Koczka, Gergely, 39
Koester, Niels, 53
Korol, Olena, 31
Krischan, Klaus, 109
Krstic, Dejan, 29
Krähenbühl, Laurent, 95
Kumagai, Makoto, 107
Kuwahara, Hiroyuki, 89

Labinsky, Robert, 39
Longhitano, Maria Roberta, 95

Lowther, David, 1
Löffler, Michael, 115

Magele, Christian, 109
Maruyama, Yuya, 89
Marák, Károly, 117
Minehisa, Ryoko, 97
Mohammadi, Mohammad Hossain, 1
Muetze, Anette, 109

Nagakura, Ken, 97
Nakamura, Sousuke, 11
Nakamura, Yuta, 11
Nakashima, Hiroshi, 45
Neumayer, Markus, 47
Nierla, Michael, 115

Okamoto, Yoshifumi, 11, 99, 107

Padilha Leitzke, Juliana, 37
Palka, Ryszard, 3
Pantelyat, Michael G., 31
Parz, Peter, 53
Pichler, Franz, 53, 59
Piotuch, Rafal, 3
Preis, Kurt, 39
Prosznigg, Florian, 53
Pávó, József, 117

Rakotoarison, Harijaona Lalao, 113
Reddy, Sohail R., 59
Renhart, Werner, 23
Roppert, Klaus, 71
Rupitsch, Stefan J., 115

Santos Da Silva, Safire Torres, 113
Scharrer, Matthias K., 59
Schenk, Mario, 109
Scorretti, Riccardo, 95
Shutta, Yusaku, 77
Sixdenier, Fabien, 95
Smajic, Jasmin, 69
Stankovic, Vladimir, 29
Stetco, Christian, 5
Stojanovic, Miodrag, 101
Straßer, Sebastian, 17
Ströhlein, Christopher Andreas, 73
Suppan, Thomas, 47

Takahashi, Masahide, 89
Takahashi, Norio, 97
Takahashi, Yasuhito, 25, 45, 77, 97
Thaler, Alexander, 53
Toth, Florian, 71
Trlep, Mladen, 83
Tsujikawa, Kazuma, 97
Töpfer, Hannes, 49

Ulm, Jürgen, 49

Vanderheyden, Benoît, 27
Vuckovic, Dragan, 29

Wakao, Shinji, 89
Watanabe, Naoya, 25
Watzenig, Daniel, 59
Wilhelm, Johann, 23
Willerich, Stephan, 75

Yagi, Makoto, 89
Yatchev, Ivan, 19
Yelanskyi, Yurii, 31

Zangl, Hubert, 5, 37